

Theoretical Analysis, Simulation and Development of Antenna Arrays for mm-Wave Systems

Submitted to

Department of Microwave Electronics

Faculty of Electrical Engineering and Computer Science

University of Kassel, Germany

in partial fulfillment of the requirement for the degree

Master of Science in Electrical Communication Engineering

Thesis was work carried out at

Barkhausen Institut

Dresden, Saxony

Author: Merve Tascioglu

Matriculation No: 35215477

First Examiner: Prof. Dr.-Ing. Axel Bangert

Second Examiner: Prof. Dr. Bernd Witzigmann

Supervisor: Dr. Padmanava Sen (Barkhausen Institut)

Kassel, May 2021

To the best of my knowledge, I do hereby declare that this master thesis work report is my own work. It has not been submitted in any form to any other university or other institution of education. Information derived from the published or unpublished work of others has been acknowledged in the text and a list of references is given.

Kassel, May 2021

A handwritten signature in black ink, consisting of a large, stylized 'M' followed by a vertical line and some smaller, less distinct characters.

Student's signature

Merve Tascioglu

Acknowledgements

First and foremost, I would like to express my sincere gratitude to Prof. Dr.-Ing Axel Bangert and Prof. Dr. Bernd Witzigmann for agreeing to be my supervisors and encouraging me to complete this thesis project. The completion of this undertaking would have not been possible without meaningful support of them. I am eternally grateful to Dr. Padmanava Sen for giving me an opportunity to undertake this attractive project at Barkhausen Institut and his continuous support from the beginning with his team of RF Design Enablement. My sincere thanks go to Mehrab Ramzan for his technical support about antenna array fabrication and measurements, to Dr. Marco Zoli for his contribution for Ray Tracing simulations, to Dr. André Barreto for his insightful comments and suggestions. Finally, I would like to extend my thanks to my husband, Alp Yalcinkaya for providing me with unfailing and continuous support.

CONTENTS

Abstract	i
List of Figures.....	ii
List of Tables	v
Abbreviations	vi
List of Symbols	viii
1. INTRODUCTION	10
1.1 Thesis Goal.....	11
1.2 Thesis Organization	12
2. THEORY OF ANTENNA AND PROPAGATION.....	13
2.1 Antenna Regions.....	14
2.2 Antenna Key Parameters.....	16
2.3 Antenna Propagation Aspect	25
2.4 Microstrip Patch Antennas	26
2.4.1 Feed Techniques of Microstrip Antennas	27
2.4.2 Method of Analysis	30
2.4.3 Guide to Design a Microstrip Patch Antenna	31
2.5 Antenna Array Theory	35
2.5.1. Geometrical Configuration	36
2.5.2 Array Layout	45
2.5.3 Phased Array Antennas	51
2.5.4 Antenna Array Feed Structure	56
2.5.5 Mutual Coupling	58
3. SIMULATIONS & MEASUREMENTS	59
3.1. Development of Python Simulator	59
3.2 Effects of Essential Parameters	60
3.2.1 Inter-Element Spacing	60
3.2.2 Effects of the Number of Elements in the Array	61
3.2.3 Steering angle.....	62
3.2.4 Comparison of Phase Shifter and TTD	63
3.3 Proposed Antenna Arrays	70
3.3.1 Uniformly Spaced Arrays	70
3.3.2 Non-Uniformly Spaced Arrays	74

3.4 3D Simulations by HFSS	83
3.4.1 Proposal of Single Rectangular Patch antenna at 10 GHz.....	84
3.4.2 Uniformly Spaced Linear Rectangular Array Antenna Designs at 10 GHz.....	88
3.4.3 Non-uniformly Spaced Linear Rectangular Array Antenna Designs at 10 GHz....	92
3.4.4 Uniformly Spaced Planar Rectangular Array Antenna Designs at 10 GHz	95
3.4.5 Non-Uniformly Spaced Planar Rectangular Array Antenna Designs at 10 GHz .	100
3.5 Comparison of Theory and Simulation.....	102
3.6 Fabrication and Measurement	108
4. APPLICATION USE CASES AND RELEVANT ALGORITHM.....	115
5. CONCLUSION.....	122
BIBLIOGRAPHY	124

Abstract

The immense growth of wireless data traffic in recent years has made the millimeter-wave frequencies good candidates for fulfilling the requirements of high data rates, lower latency as well as increased coverage. Moreover, higher operating frequencies allow reduction in the size of the antennas which may be particularly beneficial for area consumption in device integration. However, there are various design challenges of the array such as the design of feed lines and inter-element spacing that are heavily correlated with grating lobes, side lobes and mutual coupling. Besides, the large-scale antenna arrays are necessary to enhance the gain and combat the severe propagation losses. This thesis concentrates on the investigation, development, fabrication and measurement of mm-wave arrays consisting of microstrip patch antennas with different geometrical configurations and layouts. The scope of the dissertation also covers the implementation of beam steering techniques on the phased array systems which are highly attractive for mm-wave frequency applications where high path loss, attenuation from obstacles and high losses due to atmospheric gases are prevalent. Furthermore, ray tracing technique is used with an isotropic antenna as the transmitter and developed arrays in the receiver to predict radio propagation in indoor environments.

Keywords: mm-wave communication, phased array, microstrip patch antenna, antenna array design, beam steering, ray tracing

List of Figures

Figure 1.1 Summary of the Project’s Step	12
Figure 2.1 Field Region of antenna [1]	15
Figure 2.2 Schematic diagram of antenna fundamental parameters [2].....	16
Figure 2.3 The antenna as a transducer structure [4]	17
Figure 2.4 Transmission line elements [4]	17
Figure 2.5 Transmission-line Thevenin equivalent of antenna in transmitting mode [1].....	18
Figure 2.6 Reflection coefficients representation on the Smith Chart	20
Figure 2.7 Coordinate system for antenna analysis. [1].....	21
Figure 2.8 3D far field radiation pattern of the antenna [6]	22
Figure 2.9 2D radiation pattern of directional antenna [1]	23
Figure 2.10 Various Shapes of Patch Antennas [1,14]	26
Figure 2.11 Microstrip antenna [1]	26
Figure 2.12 Typical feeds types for microstrip antennas [1].....	27
Figure 2.13 Types of microstrip line feed	28
Figure 2.14 Coaxial (probe) feed [29].....	29
Figure 2.15 Charge distribution and current density creation [1,14]	30
Figure 2.16 Radiation edge of microstrip antenna [14].....	32
Figure 2.17 Radiation edge of microstrip antenna [1,8].....	32
Figure 2.18 Physical dimension of patch antenna and fringing field [1]	33
Figure 2.19 Categorization of antenna array	36
Figure 2.20 Different arrangement of an antenna array [11].....	37
Figure 2.21 Antenna Coordinate System [11]	37
Figure 2.22 Pattern Multiplication [14].....	38
Figure 2.23 Linear array along z axis.....	39
Figure 2.24 Linear array of N isotropic elements positioned along the x-axis.....	42
Figure 2.25 Planar array geometry [1]	44
Figure 2.26 Normalized Array Factor for $d=1.5\lambda$, $N=32$	46
Figure 2.27 Array Factor vs Phase Function (ψ) Plot with $d=0.5\lambda$	48
Figure 2.28 Normalized Array Factor vs Phase Function (ψ) Plot with $d=0.5\lambda$	49
Figure 2.29 Normalized Array Factor in dB vs Phase Function (ψ) with $d=0.5\lambda$	50
Figure 2.30 Different Geometrical Configurations	51
Figure 2.31 Illustration of time delay due to additional travel distance.....	52

Figure 2.32 Basic Schema of a Phase scanned linear array [40]	53
Figure 2.33 Beam direction deviation for several frequency deviations.	55
Figure 2.34 Basic Schema of a Time Scanned linear array [40]	55
Figure 2.35 Feed Arrangement for Microstrip Patch Antenna Array [1]	56
Figure 2.36 Tapered Lines and Quarter Wavelength Transformers [1]	57
Figure 3.1 Graphical User Interface of Python Antenna Array Simulator	59
Figure 3.2 Normalized Array factor patterns of 32 element broadside uniform array along y axis at different spacing.....	60
Figure 3.3 Normalized Array factor patterns of uniform array along y axis with different element count.....	61
Figure 3.4 Normalized Array factor patterns of uniform array along y axis with different inter-element spacing at $\theta_0=35^\circ$	62
Figure 3.5 Normalized Array factor patterns of uniform array along y axis with different beam steering angles.....	63
Figure 3.6 Normalized Array factor patterns of uniformly spaced 16 elements linear array along y axis with different beam steering angles when the phase shifting is implemented....	65
Figure 3.7 Normalized Array factor patterns of uniformly spaced 16 elements linear array along y axis with different beam steering angles with the phase-shifter implementation in t Ka-band	67
Figure 3.8 Normalized Array factor patterns of uniformly spaced 16 elements linear array along y axis with different beam steering angles when the TTD is implemented.....	68
Figure 3.9 Normalized Array factor patterns of uniformly spaced 16 elements linear array along y axis with different beam steering angles when the TTD is implemented in Ka-band	70
Figure 3.10 Normalized Array factor patterns of uniformly spaced broadside linear arrays along x- axis.....	71
Figure 3.11 Normalized Array factor patterns of uniformly spaced broadside planar arrays along -x and -y axes	72
Figure 3.12 Normalized Array factor patterns of uniformly spaced broadside arrays with the same number of elements and different geometrical configuration.....	73
Figure 3.13 Different Array Layouts.....	74
Figure 3.14 Normalized Array factor patterns of Uniform and Asymmetrical Non-Uniform broadside linear arrays along x- axis.....	76
Figure 3.15 Normalized Array factor patterns of Uniform and Symmetrical Non-Uniform broadside planar arrays along x- and y- axes	78

Figure 3.16 Normalized Array factor patterns of Uniform and Symmetrical Non-Uniform broadside linear arrays along x- axis.....	80
Figure 3.17 Normalized Array factor patterns of Uniform and Symmetrical Non-Uniform broadside planar arrays along x- and y-axes	82
Figure 3. 18 Layout of HFSS.....	83
Figure 3.19 Final design of rectangular Patch antenna in HFSS	84
Figure 3.20 Graphical Representation of Simulation results of RMSA at 10 GHz.....	87
Figure 3.21 Final design of Linear arrays in HFSS	89
Figure 3.22 Graphical Simulation result of Linear array antennas 3D Gain Polar Plot.....	91
Figure 3.23 Gain comparison of 2x1 Linear Array with different inter-element spacing.....	92
Figure 3.24 Gain patterns of Uniform and Non-Uniform broadside linear arrays along x- axis	94
Figure 3.25 Final design of Planar arrays in HFSS.....	97
Figure 3.26 Graphical Simulation result of Linear array antennas 3D Gain Polar Plot.....	99
Figure 3.27 Gain Patterns of 8x1 Linear vs 4x2 Planar Arrays in HFSS	100
Figure 3.28 Gain patterns of Uniform and Non-Uniform broadside planar arrays along x- and y- axes	101
Figure 3.29 Comparison of Gain Patterns of Linear Arrays in HFSS and Theory	105
Figure 3.30 Comparison of Gain Patterns of Planar Arrays in HFSS and Theory	107
Figure 3.31 LPKF ProtoMat Machine [55]	108
Figure 3.32 Top view of printed antenna arrays	109
Figure 3.33 Measured input Return Loss of 4x1 and 4x2 patch antenna arrays.....	110
Figure 3.34 Received power results of Spectrum Analyzer	112
Figure 3.35 Comparison between the measured and simulated input return loss of proposed antenna arrays	114
Figure 4.1 Scenario for Ray Tracing.....	116
Figure 4.2 Arrays with the comparison of aforementioned materials in scenario-1.....	119
Figure 4.3 Arrays with the comparison of aforementioned materials in scenario-2.....	120
Figure 4.4 Comparison of performance of 4x2 and 8x1 array with same materials.....	121

List of Tables

Table 2.1 Features of Microstrip patch antennas	27
Table 2.2 Comparison of Feed Techniques	29
Table 3.1 Dimensions of Single Rectangular Microstrip Patch Antenna	85
Table 3.2 Numerical simulation result of Single Rectangular Patch Antenna	87
Table 3.3 Numerical Simulation Result of Linear Array Antennas	91
Table 3.4 Numerical simulation results of 8x1 linear arrays	94
Table 3.5 Numerical simulation results of 4x1 linear arrays	94
Table 3.6 Numerical Simulation Result of Planar Array Antennas	99
Table 3.7 Numerical simulation results of 4x2 planar arrays	101
Table 3.8 Numerical simulation results of 8x2 planar arrays	102
Table 3.9 Comparison Between Simulation and Measurement Results.....	113
Table 4.1 Features of Indoor Environments	117
Table 4.2 Material Properties.....	118

Abbreviations

mm-wave	Millimeter wave
Radar	Radio Detection and Ranging
IoT	Internet of Things
EM	Electromagnetic
HFSS	High Frequency Structure Simulator
FEM	Finite Element Method
RMSA	Rectangular Microstrip Patch Antenna
LF	Low Frequency
HF	High Frequency
VSWR	Voltage Standing Wave Ratio
RL	Return Loss
HPBW	Half Power Beam Width
FNBW	First Null Beam Width
BW	Bandwidth
G	Gain
D	Directivity
FBW	Fractional Bandwidth
W	Width
W _p	Width of the Patch antenna
L	Length
L _p	Length of the Patch antenna
h	Height
Cu	Copper
Au	Gold
TEM	Transverse Electric-Magnetic
AF	Array Factor
EF	Element Factor
RF	Radio Frequency
TTD	True Time Delay
BF	Beamforming
SLL	Side Lobe Level
EGB	Electromagnetic Bandgap

Tx	Transmitter
Rx	Receiver
PCB	Print Circuit Board
RT	Ray Tracing
MIMO	Multiple Input Multiple Output
LoS	Line of Sight
AoA	Angle of Arrival
MUSIC	Multiple Signal Classification
ESPRIT	Estimation of Signal Parameters via Invariant Techniques
MVDR	Minimum Variance Distortionless Response
GTP	Geometrical Theory of Propagation
GO	Geometrical Optics
UTD	Uniform Theory of Diffraction

List of Symbols

λ	Wavelength
Γ	Reflection Coefficient
c_0	Speed of light in vacuum
Ω	Ohm
ϵ	Permittivity of a dielectric medium
μ	Permeability of a material
σ	Electrical conductivity of a material
$\nabla \times$	Curl (mathematical operation)
$\nabla \cdot$	Divergence (mathematical operation)
ρ	Charge density per unit volume [coulombs/m ³]
\vec{E}	Electrical Field vector
\vec{H}	Magnetic Field vector
\vec{D}	Electric Flux Density
\vec{B}	Magnetic Flux Density
\vec{J}_{ext}	Current Density
Z_0	Characteristic Impedance
Z_{in}	Input Impedance
R	Resistance
L	Inductance
C	Capacitance
η	Efficiency
$U(\theta, \Phi)$	Radiation intensity
$G(\theta, \Phi)$	Array's Radiation Pattern
ϵ_{eff}	Effective Dielectric Constant
ϵ_r	Dielectric Constant
f_r	Resonance Frequency
ΔL	Extension of Length
d_n	Position of element
Δt	Time Delay
I_0	Excitation of isotropic radiator
k	wave number

β_n	Phase Shift
E_t	Total Electric Field
\widehat{a}_r	Unit Vector of Position
Ψ	Phase Function
$\tan\delta$	Loss tangent
R_{in}	Input Impedance
R_{rad}	Radiation Resistance
R_{loss}	Loss Resistance

1.

INTRODUCTION

In modern-days communication systems, antennas at millimeter waves (mm-wave) have attracted much attention as a result of the increasing demand of wireless data traffic as well as rapid development of 5G technology and Internet of Things (IoT). The application areas of mm-wave communications vary from cellular and radar communication to automotive radars, medical imaging, security and healthcare which involve diverse range of frequency starting from 10 GHz to 300 GHz [10]. To meet the requirements (i.e higher data rate and bandwidth (BW), increased coverage, etc.) of novel applications in IoT, higher operating frequencies with huge BW are required in most solutions. On the other hand, the mm-wave communications have a few limitations from sensitivity to blockage due to weak diffraction capability as well as dispersion and propagation losses due to the high frequency. The severe path loss at these frequencies is also a key issue which limits the communication distance. The large scale antenna array with increased gain and directivity must be utilized to overcome these severe losses. Accordingly, the use of a special antenna beamforming/beam steering technique can overcome the link margin limitations in a system due to higher path losses. Antenna beamforming are usually achieved via phased array antennas in which radiation pattern can be reinforced in a particular direction and suppressed in undesired direction. In other words, the phased array can be used to steer the transmitted or received electromagnetic energy along a certain direction. The beam-forming arrays are good selections to increase the coverage and data capacity of the mm-wave communication system. However, the design of an antenna array at mm-wave frequencies is quite complex process and includes several design challenges in high BW systems as follows:

- The inter-element spacing is essential factor for an antenna array design. If the spacing is sufficiently large compared to the wavelength, the in-phase addition of radiated field may occur in more than one direction. This causes multiple maxima of the far-field radiation pattern of the array which are called grating lobes. The presence of grating lobes needs to be avoided in phased array systems.

- To achieve the desired scanning performance and avoid the grating lobes, the inter-element spacing must be kept small. However, the close spacing of these elements cause high mutual coupling which degrades the array performance. Therefore, an optimum spacing must be applied to avoid aforementioned problems.
- The beam pattern provided by a phased array is frequency-dependent in the wideband systems. Using the same phase shifts across the band causes the beam direction to vary with frequency. This phenomenon is called beam squint which must be avoided.
- The size of an array can increase the hardware implementation size as well which requires a careful attention in terms of geometrical configuration and array layout. However, the small size of the array structure may encounter with the fabrication error and losses in the feed lines which heavily needs a special care in the design phase.

Considering all above, the applications of mm-wave require a thorough investigation and understanding on the design of mm-wave antennas, and phased array systems.

1.1 Thesis Goal

The goal of this thesis project is to investigate various antenna arrays with different geometrical configurations (i.e linear array, planar array), array layouts (i.e uniform and non-uniform spacing) and beamsteering techniques (i.e True Time-Delay, Phase shifting). Within the scope of it, a Python phased array simulator aligned with antenna array theory was developed in order to observe the behavior of the desired array characteristic rapidly without long simulations by changing the inter-element spacing, number of elements, array geometry and beamsteering techniques. Furthermore, the analytical simulations were also validated with 3D EM simulator as well as real time laboratory measurements. In addition, the beam patterns of proposed antenna arrays were integrated to observe their performance in Ray Tracing (RT) tool which is developed by the group of Research in Electromagnetic Propagation and Wireless Channel Modelling at the University of Bologna to predict radio propagation [61]. To actualize the desired investigations, X-band (10 GHz) was chosen because of low-cost, relatively easier fabrication& measurement and suitability for many radar applications. Owing to the fact that the theory for the array design behind the X-band as well as higher frequency bands (30-300 GHz) are the same in many aspects, this thesis presents a prior research for higher mm-wave frequency applications.

Accordingly, the following steps were completed in order to finalize the project successfully.

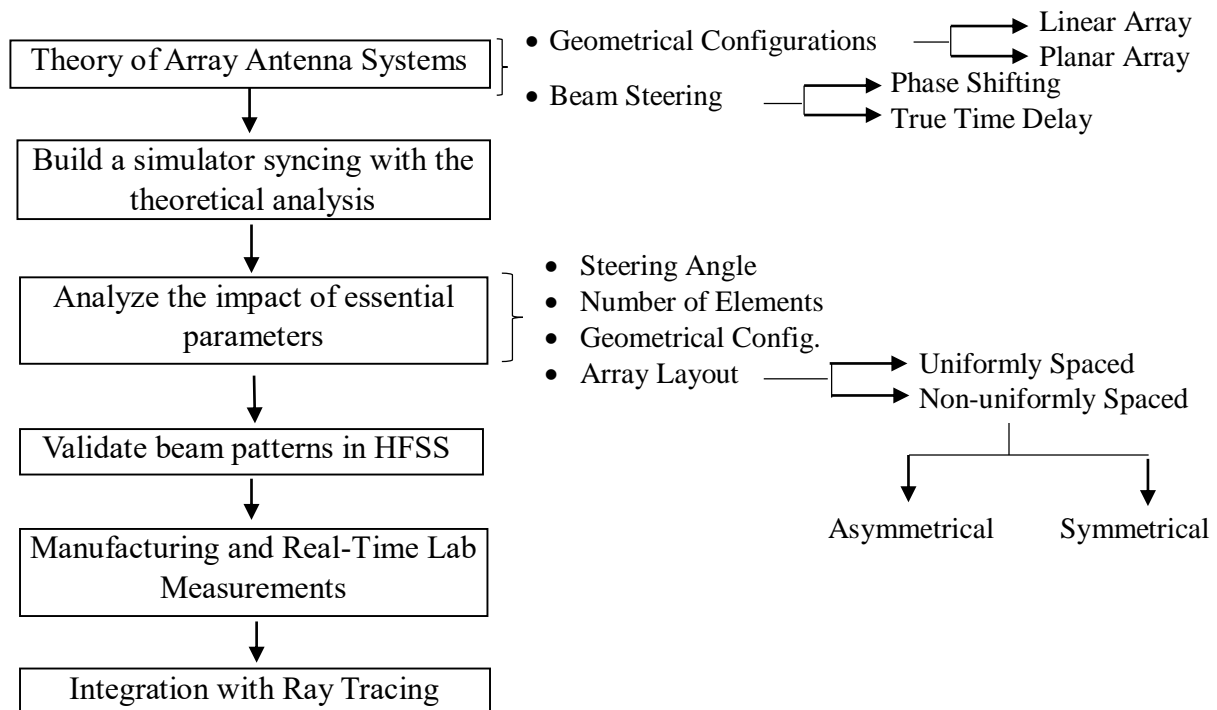


Figure 1.1 Summary of the Project's Step

1.2 Thesis Organization

The subsequent chapters in this thesis project are structured as follows:

Chapter 2 addresses the fundamentals of phased array antenna theory by providing a basic understanding of the antenna characteristics, microstrip patch antennas as well as antenna array theory.

Chapter 3 presents the various designs, simulations as well as fabrication and measurement results of proposed arrays with the comparison of the results.

Chapter 4 covers the integration of proposed arrays with ray tracing algorithm which enables to predict radio propagation in created indoor environment.

Chapter 5 gives the main conclusion of the research presented in this thesis and recommendations for future studies in the field of mm-wave communication systems.

2.

THEORY OF ANTENNA AND PROPAGATION

For a deeper understanding of antennas, the radiation mechanism is the most important aspect of the antenna theory. Electromagnetic radiation is generated in the case of the acceleration or deceleration of electric charges. (time-motion of electric charge). Maxwell's equations assist in the formulation of electromagnetic (EM) energy radiation from a current source. This occurs at any frequency [1]. To describe how electric and magnetic fields interact with one another, the set of partial differential Maxwell equations must be considered. These equations, which also explain the behaviour of microwave components such as antennas, waveguides, fiber, are given as follow [1,16]:

$$\nabla \times \vec{E} = -\frac{\partial \vec{B}}{\partial t} \quad (2.1)$$

$$\nabla \times \vec{H} = \frac{\partial \vec{D}}{\partial t} + \vec{J}_{ext} \quad (2.2)$$

$$\nabla \cdot \vec{D} = \rho \quad (2.3)$$

$$\nabla \cdot \vec{B} = 0 \quad (2.4)$$

where $\vec{H} \left[\frac{A}{m} \right]$ and $\vec{E} \left[\frac{V}{m} \right]$ define the magnetic and electric field vector, $\vec{B} \left[\frac{Wb}{m^2} \right]$: Magnetic flux density vector, $\vec{D} \left[\frac{C}{m^2} \right]$: Electric displacement density vector. $\rho \left[\frac{C}{m^3} \right]$: Local charge density per unit volume, $\vec{J}_{ext} \left[\frac{A}{m^2} \right]$: External current density vector.

Electric charges or electric currents produce the electric field \vec{E} , magnetic field \vec{H} , electric flux \vec{D} and magnetic flux \vec{B} , which are all time- and position- dependent parameters. Faraday's law and Ampere's law are defined by equations 2.1 and 2.2, respectively. The Gauss' law for magnetic and electric fields is the basis of equations 2.3 and 2.4.

Furthermore, the constitutive equations (or material equations) describe the interaction of electromagnetic waves and matter via vector notation as given by equations 2.5-6-7 [1].

$$\vec{D} = \epsilon \vec{E} \quad (2.5)$$

$$\vec{J} = \sigma \vec{E} \quad (2.6)$$

$$\vec{B} = \mu \vec{H} \quad (2.7)$$

where ϵ : Permittivity of a dielectric medium, σ : Electrical conductivity of a material, μ : Permeability of a material.

The EM wave equation (Helmholtz) is the most crucial second-order differential equation used to explain the propagation of electromagnetic waves in a medium or in a vacuum, and it is derived from both the constitutive equation and Maxwell's equation. Plane wave propagation in lossless homogeneous free space is the simplest solution of the wave equation. It must be noted that the following conditions must be met to obtain the plane wave solution [2,3]:

- i. The electric and magnetic field strength vectors are perpendicular to each other and mutually perpendicular to the propagation direction.
- ii. Free space and Far-field conditions must be satisfied.

2.1 Antenna Regions

The curvature of the electromagnetic field, which is called field pattern, directly related to the antenna dimensions and the distance from the corresponding antenna. Two forms of energy (radiating energy and reactive energy) are related to the surrounding electromagnetic fields which are divided into three regions as their boundaries illustrated by Figure 2.1 [1]:

- i. Reactive Near Field
- ii. Radiating Near Field (Fresnel Region)
- iii. Far-Field (Fraunhofer Region)

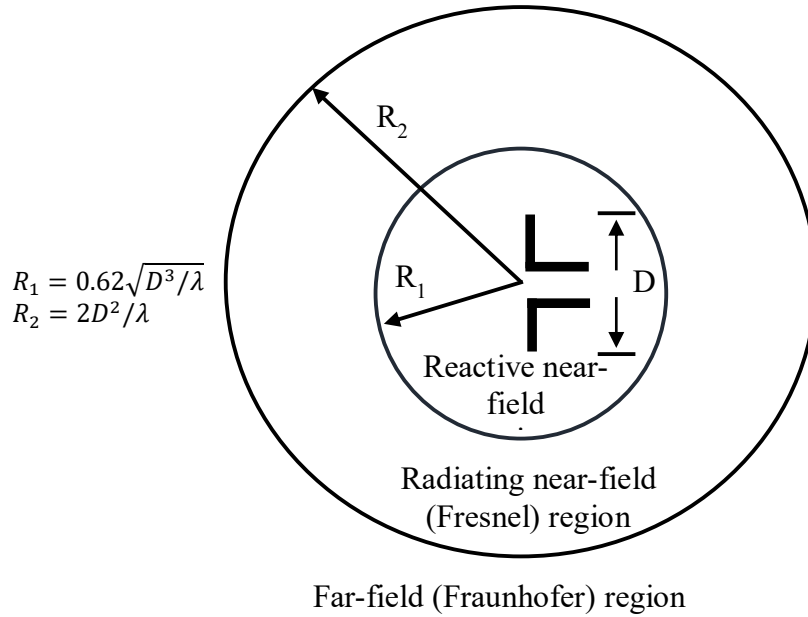


Figure 2.1 Field Region of antenna [1,66]

Reactive energy dominates in the reactive near-field region, causing the electric and magnetic fields to be out of phase by 90° . There is no energy dissipation since the energy is stored. The following equation describes this region's boundary [1]:

$$R_1 < 0.62\sqrt{\frac{D^3}{\lambda}} \quad (2.8)$$

where R_1 : The distance from the antenna, D : The largest dimension of the antenna, λ : wavelength.

Equation 2.9 gives the boundary of Fresnel region where the form of the radiation pattern cannot be fully described although the radiating near field is dominant [1]:

$$0.62\sqrt{\frac{D^3}{\lambda}} < R < \frac{2D^2}{\lambda} \quad (2.9)$$

where R : The distance from the antenna, D : The largest dimension of the antenna, λ : wavelength.

The far-field region has the greatest impact on antenna characteristics and performance. The antenna radiation pattern is established in this region where the electric and magnetic fields are orthogonal to each other and they are mutually perpendicular to the direction of propagation and the plane wave's wave-front remains stable. Hence, the angular field distribution is independent of the distance from the antenna [1]. The boundary of far-field region is calculated as follow [1]:

$$R_2 \geq \frac{2D^2}{\lambda} \quad (2.10)$$

where R_2 : The distance from the antenna, D : The dimension of the antenna, λ : Wavelength.

2.2 Antenna Key Parameters

The main goal of this section is to provide an overview for the most significant parameters (space quantities) that play a role in the design of an appropriate antenna. Accordingly, the simulation results presented in the following chapters would be comprehended well. Due to the reciprocity feature of the transmitting and receiving antennas, the direction of energy conversion has no major impact on the antenna's operating concept during the energy conversion process [2]. In other words, antenna parameters are the same for both sides. However, it must also be noted that there are two types of antennas as passive and active antennas and active antennas lack a reciprocity feature [2]. To observe the antenna's performance a number of parameters must be considered as illustrated by Figure 2.2.

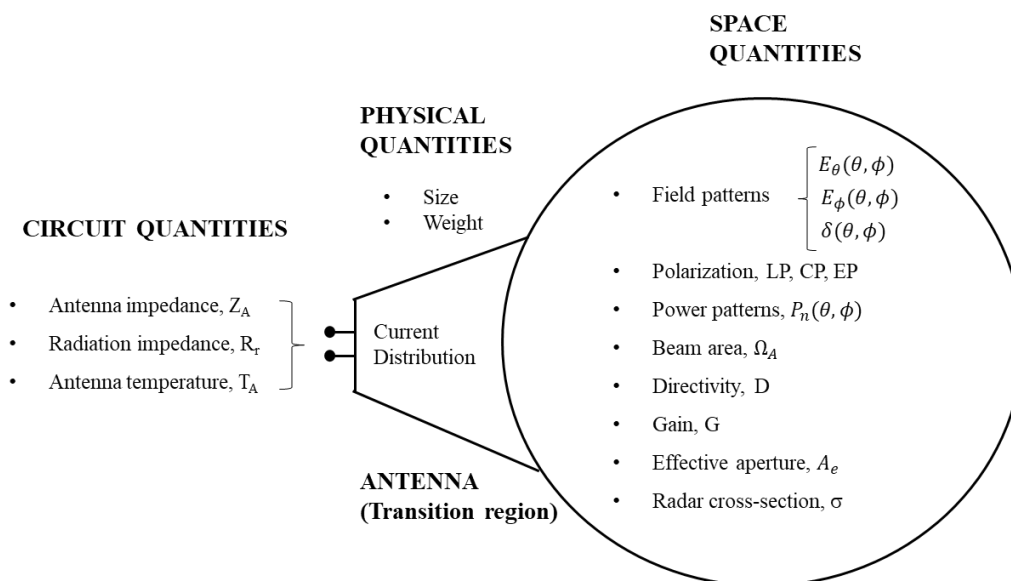


Figure 2.2 Schematic diagram of antenna fundamental parameters [2,66]

As it is mentioned, the antenna is a reciprocal device which can be utilized as a transmitter or receiver. The antenna is the transducer which represents the area of transition between free space wave and guided wave as it is shown in Figure 2.3.

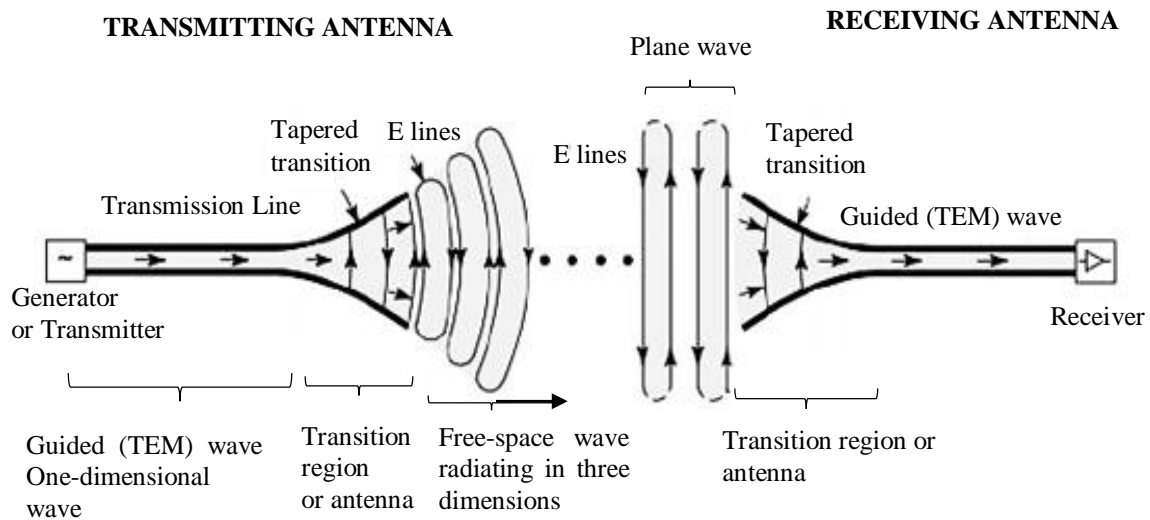


Figure 2.3 The antenna as a transducer structure [4]

The transmission line is a necessary component for transferring source power to the antenna ideally without loss. Therefore, the antenna must be connected to the transmission line, which allows radiation of generated power from the antenna to free space. To do so, characteristic impedance of transmission line is necessary. Depending on which transmission line is used, the characteristic impedance (Z_0) may have a different value such as 50Ω or 75Ω is standard for coaxial cables depending on the application and the frequency [1,5,68]. One of the most serious issues is impedance mismatch loss which is caused by the transmission line. The 'Telegrapher Equation' defines the relationship of voltage and current on the transmission line and the characteristic impedance is calculated as given by equation 2.11 (a) and (b) [68].

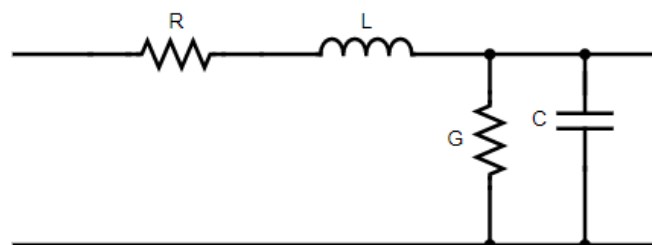


Figure 2.4 Transmission line elements [4,66]

$$Z_0 = \sqrt{\frac{R' + j\omega L'}{G' + j\omega C'}} = \sqrt{\frac{\frac{R'}{j\omega} + L'}{\frac{G'}{j\omega} + C'}} \quad (2.11) \text{ (a)}$$

There is a fact that R' and G' elements tends to be zero for high frequency and the equation transforms as follows:

$$\lim_{\omega \rightarrow \infty} Z_0 = \sqrt{\frac{\frac{R'}{j\omega} + L'}{\frac{G'}{j\omega} + C'}} = \sqrt{\frac{L'}{C'}} \quad (2.11) \text{ (b)}$$

where R [Ω]: Transmission line resistance, L [H]: Transmission line inductance, G [S]: Transmission Line conductance, C [F]: Transmission line capacitance, ω : Angular frequency [Hz].

In addition, the antenna system can be modelled as Thevenin equivalent electrical circuit as shown by Figure 2.5. The source represented by an ideal generator, the transmission line is represented by a line with characteristic impedance Z_0 and the antenna is represented by a load impedance Z_A . R_r is used to represent the radiation resistance and X_A is used to represent the imaginary part, if the impedance is associated with radiation of the antenna. R_L is referred to conduction and dielectric losses are related to the antenna structure. The goal is to transfer all energy from generator to radiation resistance R_r [1].

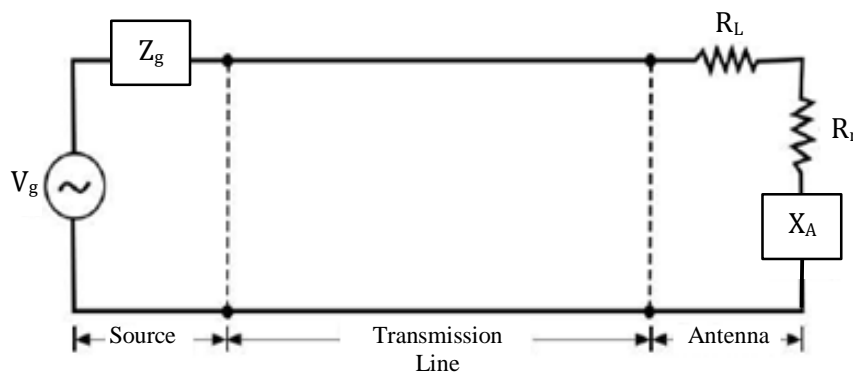


Figure 2.5 Transmission-line Thevenin equivalent of antenna in transmitting mode [1]

For that purpose, the **matching** is the most crucial and challenging issue of the antenna since the antenna impedance (load impedance) must precisely match with source impedance in order to absorb all of the power in the load. In fact, a small amount of power is reflected back to the source. Therefore, both impedances should be similar as much as possible in practice.

Besides this, since the characteristic impedance varies with frequency, it also requires to match the operating frequency of antenna's load impedance. In case the load impedance Z_A does not 100% match with the characteristic impedance Z_0 , the mismatch appears which means some of the power is reflected. The **reflection coefficient (Γ)**, which is the complex ratio of the reflected (backward) voltage wave to the forward (incident) voltage or current wave, is used to determine the amount of reflected power back to the source [68].

$$\Gamma(l) = \frac{V_0^-}{V_0^+} = \frac{Z_L - Z_0}{Z_L + Z_0} e^{-2\gamma l} \quad (2.12) \text{ (a)}$$

$$\text{At the end of the line (where } l=0\text{): } \Gamma(l=0) = \frac{V_0^-}{V_0^+} = \frac{Z_L - Z_0}{Z_L + Z_0} \quad (2.12) \text{ (b)}$$

where Γ : Reflection Coefficient, V_0^- : Reflected voltage wave, V_0^+ : Forward incident wave, Z_L : Load impedance, Z_0 : Characteristic impedance, γ : Propagation coefficient, l : Transmission line length

The reflection coefficient is a complex number that varies depending on the frequency. Some fundamental reflection coefficients should be remembered [69]:

- The line is perfectly matched with $\Gamma=0$ and $Z_L = Z_0$.
- The line is open-circuited (maximum positive reflection) with $\Gamma=1$ and $Z_L = \infty$,
- The line is short-circuited (maximum negative reflection (180° phase shift)) with $\Gamma=-1$ and $Z_L = 0$

The graphical representation of the reflection coefficient is commonly shown by **Smith Chart** which is a simple way to observe the performance of the impedance matching as given by Figure 2.6.

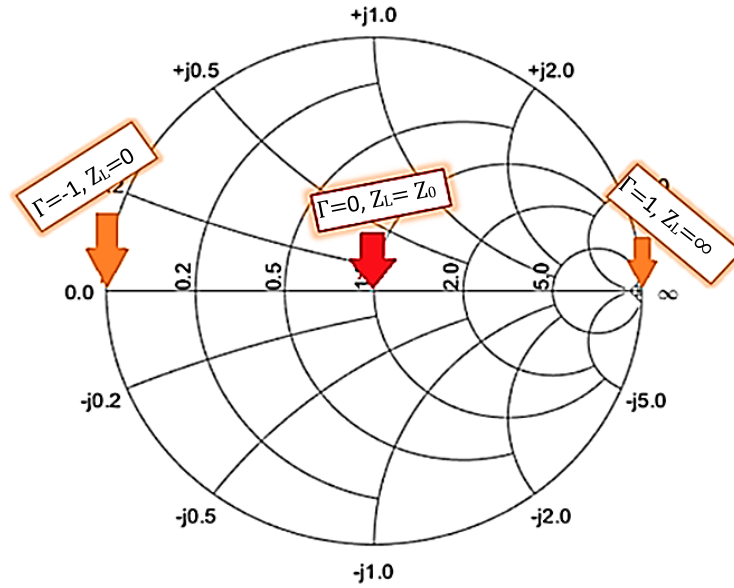


Figure 2.6 Reflection coefficients representation on the Smith Chart [66]

The **maximum power transfer theorem** is frequently used to verify matching. A standing wave occurs in case the matching condition is not met. The **voltage standing wave ratio (VSWR)**, which is the ratio of the highest voltage to the minimum voltage, characterizes these standing waves [7].

$$VSWR = \frac{V_{max}}{V_{min}} = \frac{|V_0^+| + |V_0^-|}{|V_0^+| - |V_0^-|} \quad (2.13)$$

where V_0^+ : Incident wave voltage, V_0^- : Reflected wave voltage

VSWR value can also be calculated via the reflection coefficient [1,7]:

$$VSWR = \frac{1 + |\Gamma|}{1 - |\Gamma|} \quad (2.14)$$

Return Loss, in addition to VSWR, is a parameter used to describe the quality of RF power transfer and is calculated via equation 2.15. Moreover, S11 of Scattering parameter, which is used to measure high frequency component behaviour, also enables to calculate the return loss. It should be remembered that the higher the return loss, the better the antenna's characteristic since it indicates the difference between forward radiated power and backward reflected power.

$$RL_{dB} = -20 \log |\Gamma| = -20 \log |S_{11}| \quad (2.15)$$

The antenna's **input impedance** is another essential parameter to determine the feed point of the antenna. The voltage-to-current ratio at the antenna's terminal is the way of calculating it as mathematically given by equation 2.16 [7].

$$Z_A = \frac{V_A}{I_A} = R_A + jX_A \quad (2.16)$$

The imaginary part, X_A , gives the power stored in the near-field region. R_A , which represents the real part of input impedance, is the summation of radiation resistance and loss resistance ($R_A = R_r + R_L$ [6]) as schematically given by Figure 2.5. The location of feed, antenna's type and size as well as the radiated power are decisive parameters for the radiation resistance. On the other hand, the loss resistance is associated with material properties such as dielectric loss, conductor loss, etc. Moreover, the 3D polar plot of radiated fields distribution of the antenna as a function of ϕ (azimuth angle) and Θ (elevation angle) in space is called the **radiation pattern**. Figure 2.7 gives the overview of the coordinate system utilized in radiation pattern visualization.

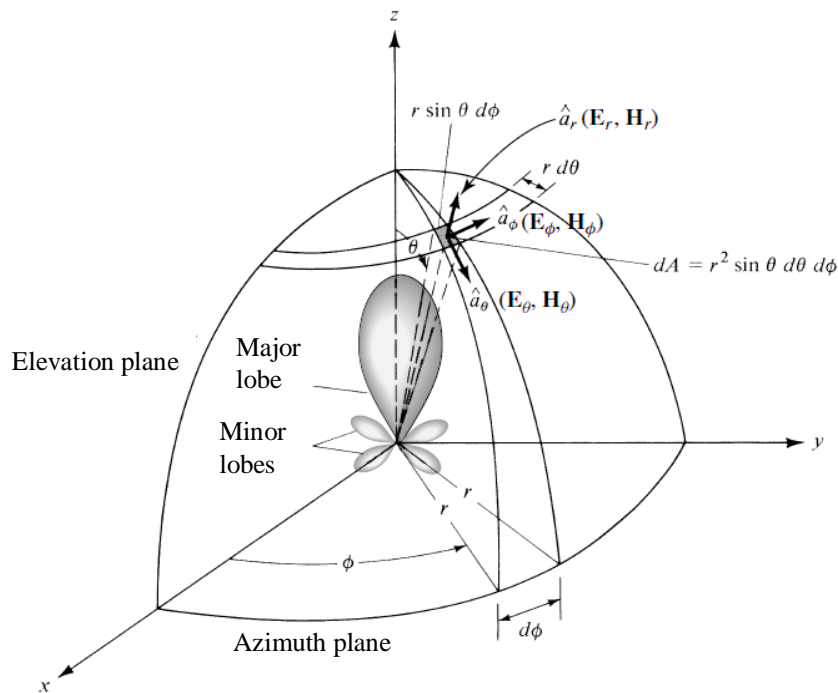


Figure 2.7 Coordinate system for antenna analysis. [1]

Figure 2.8 which is also a common way of illustration of radiation pattern shows here the donut-shaped (omnidirectional) radiation pattern as an example. It is useful for visualizing the directions in which the antenna is radiating.

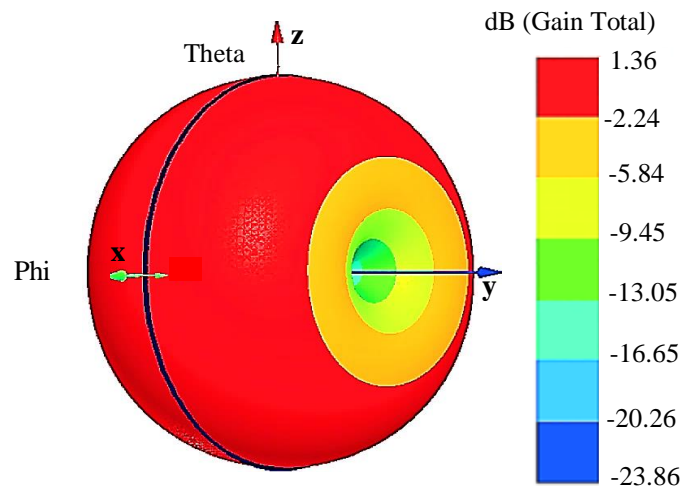


Figure 2.8 3D far field radiation pattern of the antenna [6,66]

The omnidirectional, isotropic and directional patterns are the three major types of radiation patterns. In fact, the isotropic pattern does not occur in practice because it necessitates the same radiation in all directions. The omnidirectional pattern is isotropic in a single plane as shown in Figure 2.8 where the maximum radiation exists in the x - z plane. A directional pattern is one that radiates in a single direction. In addition, the elevation plane (E-plane) and the azimuth plane (H-plane) patterns give the most significant observation about the direction of maximum radiation power. The E-plane is defined as the plane where the electric field E lies on and the H-plane is the plane where the magnetic field H lies on [1]. Instead of 3D pattern, 2D is also a common plotting that is indeed the slice of the 3D plane. These plots are useful for visualizing the direction in which the antenna radiates. Accordingly, Figure 2.9 where y - axes are on linear scale gives the 2D radiation pattern including major, minor and sidelobes. The intense radiated power is shown by the main lobes, which are prerequisite for defining the half power beamwidth (HPBW) and first null beamwidth (FNBW). The undesired radiation is represented by the minor and side lobes, which should be suppressed as low as possible. A detailed explanation about these lobes with examples is given in Chapter 2.5.

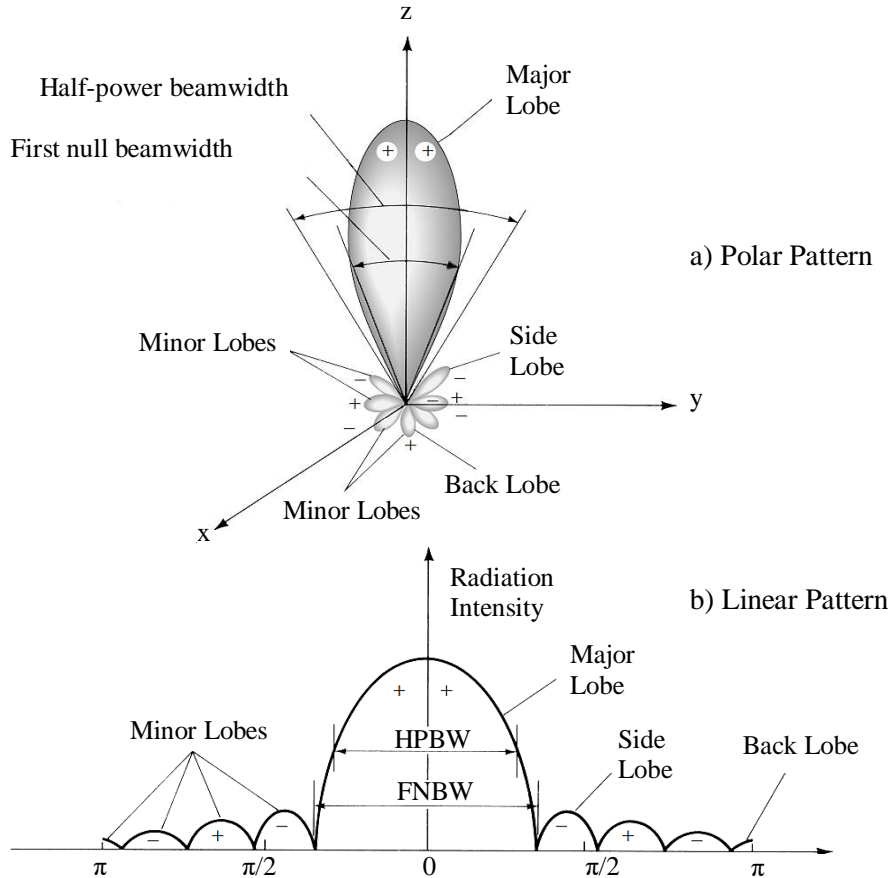


Figure 2.9 2D radiation pattern of directional antenna [1]

Beamwidth describes the angular width of the major lobe which provides the coverage region of antenna radiation. There are two forms of beamwidth: HPBW and FNBW as thoroughly seen in Figure 2.9. The angular width between the first two nulls is known as FNBW and between two certain points (at 3dB) called HPBW. The poor radiation intensity in the pattern is represented by the minor lobes, side lobes and back lobes. Moreover, the ability of the antenna to concentrate energy in a single desired direction is measured by the term of **Directivity (D)**, which is generally defined in a logarithmic scale. is the ratio of the antenna's total radiated power to its radiation intensity $U(\theta, \phi)$ as follows [2]:

$$D = \frac{U(\theta, \phi)}{(P_{rad})/4\pi} \quad (2.17)$$

where $U(\theta, \phi)$ =Radiation intensity, P_{rad} : Radiated power

There is a fact that an antenna does not transform all electromagnetic energy into radiation because of several losses such as reflection which causes the dissipation of input power as heat and material losses (i.e. dielectric loss, conductor loss). Thus, **efficiency** is necessary for measuring the association of the input and radiated power as mathematically defined below [2].

$$\eta = \frac{P_{rad}}{P_{in}} \quad (2.18)$$

where; η :Efficiency, P_{rad} : Radiated power, P_{in} :Input power

Efficiency is also calculated by the ratio of Gain and Directivity. Here, **Gain (G)** is a metric for determining the degree of directivity of an antenna's radiation pattern. It indeed determines how much power the antenna radiates in a specific direction. The ratio of radiation intensity to input power is also known as gain [2]. Gain remains constant in case the antenna is used either as a transmitter or receiver due to the reciprocity property of the passive antennas.

$$G = \frac{U(\theta, \Phi)}{(P_{in})/4\pi} \quad (2.19)$$

where G: Gain, $U(\theta, \Phi)$: Radiation intensity, P_{in} : Input power

$$G = \eta \cdot D \quad (2.20)$$

The working frequency range of the antenna is measured by **Bandwidth (BW)** that defines the energy radiated or received at a specific frequency interval. BW is indeed the difference between higher and lower frequencies. The application becomes broadband if the ratio of the upper operating frequency (f_H) to the lower operating frequency (f_L) is equal or greater than 2 [3].

$$BW = f_H - f_L \quad (2.21)$$

$$\frac{f_H}{f_L} > 2 \Rightarrow \text{Broadband application} \quad (2.22)$$

Secondly, fractional BW (FBW), which is linked to the center frequency, is also used to describe the antenna's frequency in narrowband [3].

$$FBW(\%) = \frac{f_h - f_l}{f_c} \quad (2.23)$$

where f_c : Center frequency of the antenna, f_h : Higher frequency of the antenna, f_l : Lower frequency of the antenna range

In addition to aforementioned terms, **impedance bandwidth** which depends on several parameters such as dielectric thickness, size of the ground plane and feed technique refers to return loss bandwidth [25]. It is frequently measured via return loss plot at -10 dB.

2.3 Antenna Propagation Aspect

The motion of electric charges generates electromagnetic waves which can be efficiently transmitted and received by a receiver at a distance using a suitable antenna that serves as a link between the circuit and the wireless channel. The antenna's propagation characteristics are influenced by a variety of parameters such as power, gain and efficiency of the antenna. Besides this, permittivity (ϵ) and permeability (μ) and conductive loss tangent (σ), which are the properties of the medium in which the electric and magnetic field line propagates, must be investigated properly. These parameters have a direct impact on the wavelength which is corresponding to design and performance of the antenna [3].

$$\lambda_{medium} = \frac{c_0}{f\sqrt{\epsilon_r}} \quad (2.24)$$

where c_0 : Speed of light in vacuum ($\sim 3 \times 10^8$ m/s), ϵ_r : Dielectric constant, f : Operation frequency of the antenna. In the free space, the wave velocity is given by $\frac{1}{\sqrt{\epsilon_0 * \mu_0}} = c_0$

(ϵ_0 : 8.854×10^{-12} F/m, μ_0 : $4\pi \times 10^{-7}$ H/m, $\sigma=0$ S/m)

2.4 Microstrip Patch Antennas

In today's radio communication systems, the microstrip patch antennas have been playing a significant role since it was firstly patented in 1955 [26] due to relatively easier design procedure and fabrication [1,27]. The structure of a patch antenna consists of a ground plane, dielectric substrate and a metallic trace (patch) embedded on it. Here, the permittivity of the dielectric layer (should be kept between 2.2 and 12 [1]) and the patch thickness (should be much less than the antenna's operating wavelength) are decisive parameters for the performance of the antenna. Since it provides a larger bandwidth, better reliability and better radiation, a thick substrate with a very low dielectric constant is ideal for good antenna performance. On the other hand, the antenna height increases in such a scenario therefore an optimum trade-off must be done at the design phase to get an enhanced performance at a particular operating frequency [1,28]. A patch antenna may be formed by diverse shapes such as rectangular, square, circular, elliptical, etc. as illustrated by Figure 2.10. The rectangular and circular geometries of microstrip antennas are the most frequently used ones in the design process [1].

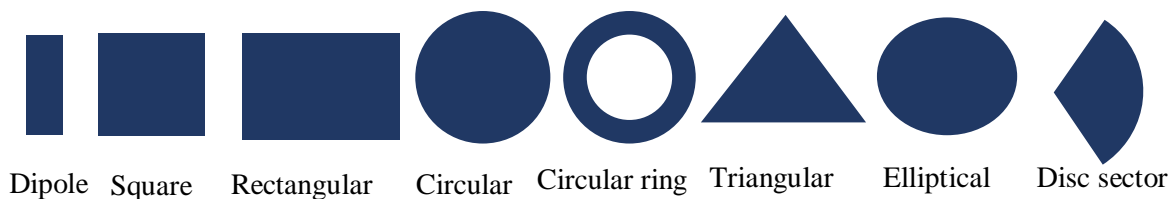


Figure 2.10 Various Shapes of Patch Antennas [1,14,66]

A rectangular patch antenna with its critical design parameters (The width (W), length (L) and height (h)) is shown by Figure 2.11.

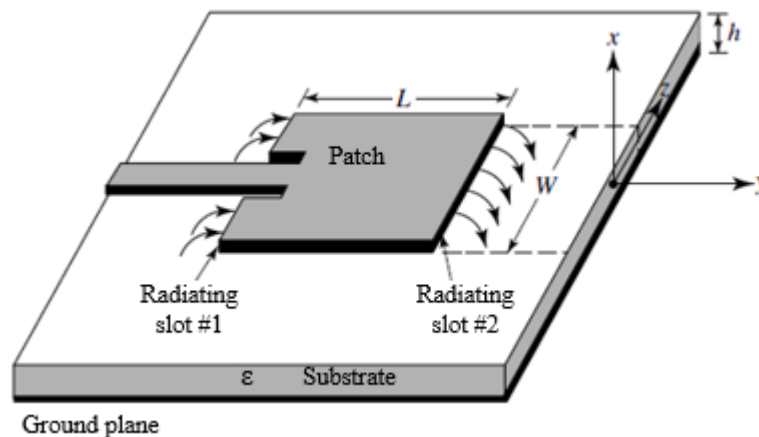


Figure 2.11 Microstrip antenna [1]

Table 2.1 is a beneficial summary of advantages and disadvantages of patch antennas [1,17].

Table 2.1 Features of Microstrip patch antennas

Advantages	Disadvantages
Linear and circular polarizations are possible	Narrow bandwidth (Volume increased is required for higher BW)
Thin profile and thereby Low weight and volume	Low efficiency because of dielectric and conductor loss
Low fabrication cost	Low gain
Easy integration	Excitation of surface waves causes spurious radiation
Dual and triple frequency operations are possible	Temperature- and humidity- sensitive
Flexible gain and pattern option via various feed methods	Limitation on maximum gain

2.4.1 Feed Techniques of Microstrip Antennas

The feed technique is a crucial parameter which has a significant effect on antenna characteristics such as VSWR, bandwidth, and return loss. There are two types of feed techniques: contacting feed and non-contacting feed [13]. The power is fed directly to the radiating patch via the connecting line in the contacting feed technique (i.e microstrip line, coaxial probe). Figure 2.12 depicts the microstrip line and coaxial probe, which are the most popular contacting feed techniques [6,29], used in this thesis project as well. Besides, non-contacting feed techniques such as proximity coupling and aperture coupling are used to transfer power between the connecting part and the radiating patch. The microstrip line feed and coaxial feed were used in this thesis.

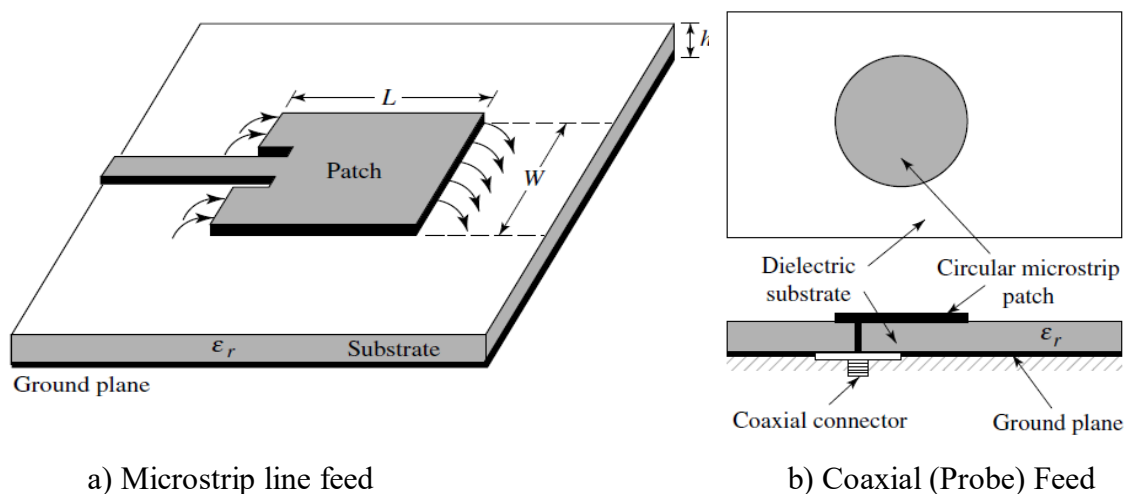


Figure 2.12 Typical feed types for microstrip antennas [1]

2.4.1.1 Microstrip Line Feed

Microstrip line feed is a method where the conducting strip is connected to the microstrip patch directly and its width is smaller than the patch's width as shown by Figure 2.13. Direct connection to the patch's edge and inset cutting are two fundamental methods for the implementation of this method. Figure 2.13 shows a microstrip line feed based on cutting a slot (inset) in the patch and a standard microstrip line feed (edge feed). Inset cutting is relatively easier to achieve impedance matching [30]. The input impedance of the microstrip patch antenna is affected by inset cutting. Therefore, the inset depth (F_i) and notch width (g) take an important role in the design of a microstrip patch antenna. Furthermore, it should be noted that the feed radiation may sometimes causes spurious radiations.

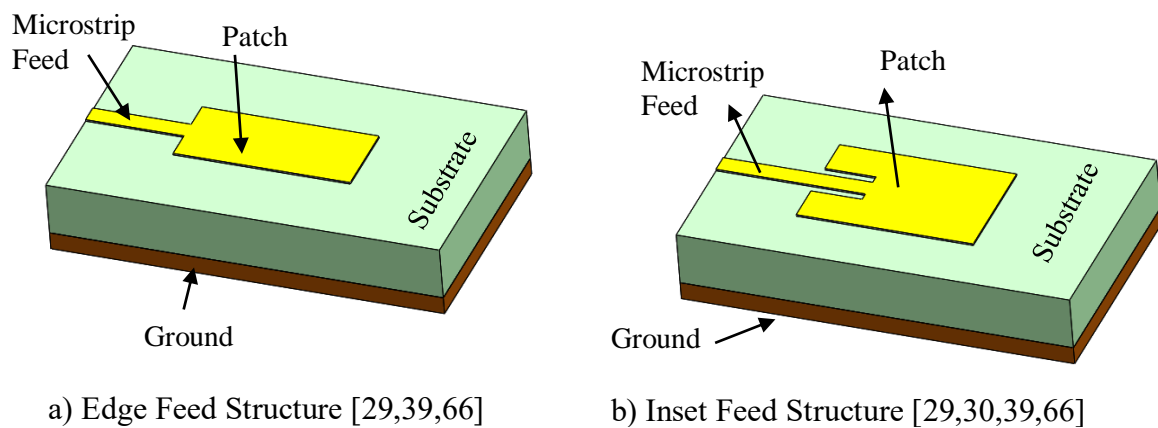


Figure 2.13 Types of microstrip line feed

2.4.1.2 Coaxial Feed

In coaxial feed technique, the inner conductor of coaxial feed is connected to the patch and the outer conductor is connected to the ground plane as displayed by Figure 2.14. Coaxial feed technique consists of an inner conductor, an outer conductor and a dielectric material in between.

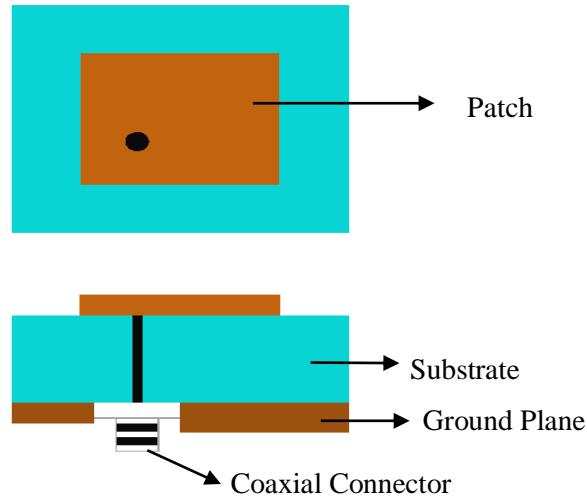


Figure 2.14 Coaxial (probe) feed [29,66]

The possibility to position the feed anywhere within the patch for impedance matching and low spurious radiation is one of the most significant benefits of coaxial feed. The coaxial feed, on the other hand, is ineffective the antenna is operated at a high frequency and the substrate is thicker [8]. Accordingly, the input impedance becomes more inductive with a thicker substrate, which allows the probe length to be extended, resulting in matching problem [1]. Besides, the skin effect occurs when the antenna is operated at high frequencies, causing significant cable attenuation and, as a result, an increase in VSWR. This feed technique also has the disadvantage of having narrower bandwidth, which is not always desirable. The advantages and drawbacks of the coaxial feed and microstrip line feed techniques are summarized in Table 2.2 [30,39,66].

Table 2.2 Comparison of Feed Techniques

Co-axial Feed Technique		Microstrip Line Feed Technique	
Advantages	Disadvantages	Advantages	Disadvantages
Adjustment of input impedance level.	Thicker substrate causes a longer probe which increases spurious radiation from the probe.	Easy fabrication. The feed can be etched on the same substrate.	The thickness of the substrate increases the spurious radiation from surface wave as well as the bandwidth.
Higher antenna efficiency and higher antenna gain.	Narrow Bandwidth	Simplicity for modelling impedance matching	The radiation also leads to undesired cross-polarized radiation.

2.4.2 Method of Analysis

Modelling and analysing microstrip patch antennas can be done in two ways: approximate model and full-wave model [10]. The full-wave model is more reliable and robust but also relatively complicated than the approximate model. In comparison to the full-wave model, the approximate model, which is used in this thesis project, provides good physical insight with a faster time solution. This model is divided into two classes based on the equivalent magnetic current distribution around the patch edges: the **transmission line model** and the **cavity model** [11]. The transmission line model is simpler and more useful for understanding the fundamental characteristics of a microstrip antenna. Patch antenna transmission model is characterized by two simple slots separated by a transmission line length L and a low impedance Z_c [1,7, 12]. On the other hand, this model has also a few drawbacks, including an inability to account for radiating edge field variance and the fact that it is only suitable for rectangular patch antennas [8,13].

To solve these types of drawbacks, the cavity model is favoured. This model examines the microstrip antenna under the assumption that the space between the patch and the ground is filled with a cavity and is bounded on both sides by electric conductors. There are some assumptions in the cavity model for thin substrates ($h \ll \lambda$) [1, 13,14,66]:

- In the region between the microstrip patch and the ground, the electric field has only a z-component and the magnetic field has only a xy- component,
- For a thin substrate, the interior fields do not vary with the z component,
- There is no component for electric current that is normal to the patch edge, so the magnetic field has a negligible tangential component along the edge.

As the power is applied to the microstrip patch antenna, the motion of charge distribution begins on the upper and lower surfaces of the patch, as well as at the bottom of the ground plane, as Figure 2.15 illustrates [1,14].

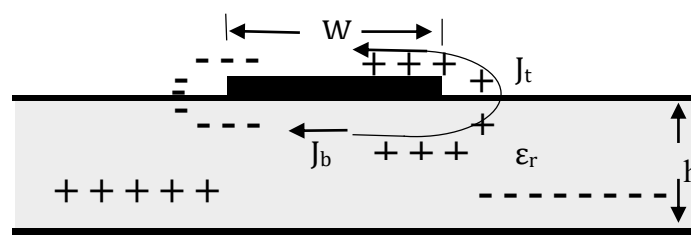


Figure 2.15 Charge distribution and current density creation [1,14,66]

There are two mechanisms for controlling the charge distribution: **attractive** and **repulsive mechanisms**. The repulsive mechanism is associated with the charge at the bottom of the patch surface which helps to transfer the charge from the bottom to the top. The attractive mechanism takes the opposite charge into account on the patch's bottom side and the ground plane. The charge distribution, which produces the current density J_b within the dielectric constant at the bottom of the patch, is involved in this mechanism. Both mechanisms lead to create densities J_t on the patch's top and bottom surfaces. When the substrate thickness is much greater than the width (W_p) of a microstrip patch antenna ($W_p \ll h$), the attractive mechanism is dominant and charges concentrate inside the dielectric substrate [8]. Since the ratio of substrate thickness to patch width decreases, the current flow around the edge can be ignored. This might lead the patch's four side walls to form a perfect magnetic conducting surface that doesn't disrupt the magnetic field [1]. To put it another way, this cavity model leads to the side walls being treated as perfect magnetic conducting surfaces.

2.4.3 Guide to Design a Microstrip Patch Antenna

The microstrip patch antenna is made up of a metal strip (patch) that can be any form as already shown by Figure 2.10 and be composed of thin ($t \ll \lambda_0$, where λ_0 is the free space wavelength) conducting material such as Au (gold) or Cu (copper) [1]. This strip conductor with height h , width W and length L is placed on the top of the substrate with dielectric constant ϵ_r which also lies on a ground plane. The length of the patch, which is commonly ranged as $\lambda_0/3 < L < \lambda_0/2$, is correlated to the patch's height and width as well as the dielectric constant of the substrate [1]. Different types of substrates may be used in the design process with dielectric constants ranging from 2.2 to 12 [1]. The dielectric constant must be carefully chosen because it has a significant impact on antenna characteristics. In order to provide better reliability and high efficiency, the dielectric constant should be low [31]. On the other hand, a thin substrate with a high dielectric constant can occasionally be necessary in the microwave circuit to minimize coupling and spurious radiation [31]. Figure 2.16 illustrates the working principle of this antenna where the charges are accelerated in the source (feed line) and reach to patch. Afterward, they radiate in the patch's edge.

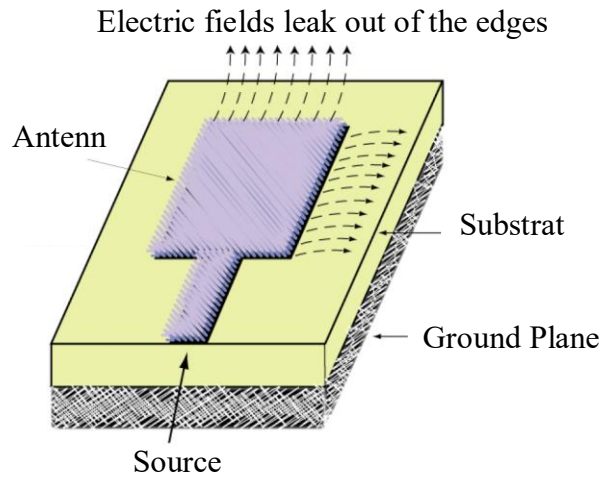


Figure 2.16 Radiation edge of microstrip antenna [14,66]

The transmission line model is widely used as an analysis method for rectangular microstrip antennas [16,17]. As shown in Figure 2.17 (a) [1,8], the transmission line model considers the patch antenna as a structure consisting of a radiating aperture (slot) with thickness t and width W . The radiating electrical field along the edges of a microstrip patch antenna fringes due to its finite length and width as Figure 2.17 (b) depicts [1,8].

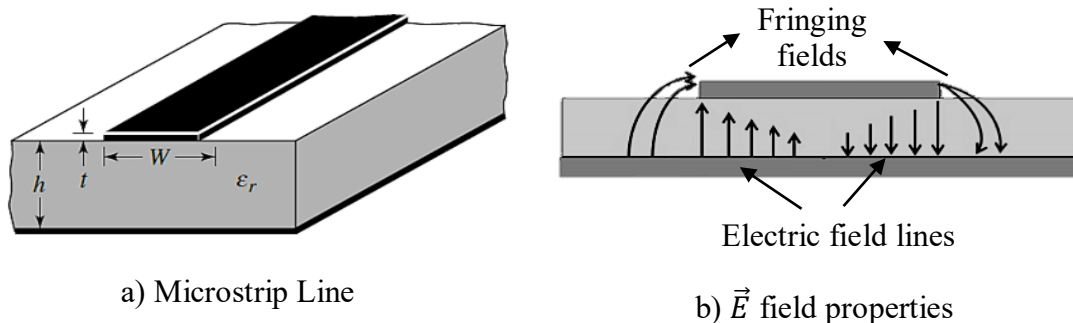


Figure 2.17 Radiation edge of microstrip antenna [1,8]

The electric field (fringing) lines are strongly correlated to the patch's size, the substrate's height, and the dielectric constant [1]. The electric field lines travel through the substrate while some parts of them spreads through the air. As a result of the fringing, the microstrip line becomes electrically wider than its physical dimensions [8]. Thus, because of the different phase velocity of air and substrate, the transmission line does not accept transverse electric-magnetic (TEM) mode [1,8]. Accordingly, quasi-TEM mode would be the dominant mode. Hence, an appropriate dielectric constant must be determined to account for fringing and wave propagation in the transmission line. The operating frequency affects the effective dielectric constant as well [1].

The fringing sector, for example, concentrates more on the substrate as the operating frequency increases. Equation 2.26 gives the calculation of the effective dielectric constant which is an approached value of the dielectric constant of the substrate [9]:

$$\epsilon_{reff} = \frac{\epsilon_r + 1}{2} + \frac{\epsilon_r + 1}{2} \left[1 + 12 \frac{h}{W} \right]^{-1/2}, W/h > 1 \quad (2.26)$$

where ϵ_r : Dielectric constant, h: Height of the substrate, W: Width of the patch antenna

According to the theory based on the half wavelength ($\lambda/2$) [1,8], a microstrip patch antenna is designed and thereby the patch length should be slightly less than $\lambda/2$. In general, this type of antenna operates in the TM₀₁ mode, which means that the field varies by one $\lambda/2$ cycle along the length but not across the width [1,17]. Figure 2.18 (a) shows two slots separated by a transmission line and open-circuited at both ends. Due to open circuit ends, voltage is the highest in the patch's width and current is the lowest [1]. With respect to the ground plane, the fields at the edges can be divided into normal and tangential components. The normal component towards the width and in the opposite direction is shown on 2.18 (b). Since some of the fields spread in the air and others place in the substrate, they are actually not in phase along the $\lambda/2$ cycle and cancel each other [8]. Because the tangential components are in phase, the highest radiating field occurs on the structure's surface. The radiating slots' fringing effect can be modelled as an electrically patch of microstrip antenna that appears larger than normal design. Accordingly, the patch's dimension will be expanded on each end by ΔL , which is a function of the effective dielectric constant ϵ_{reff} and the ratio of width to height ratio (W/h).

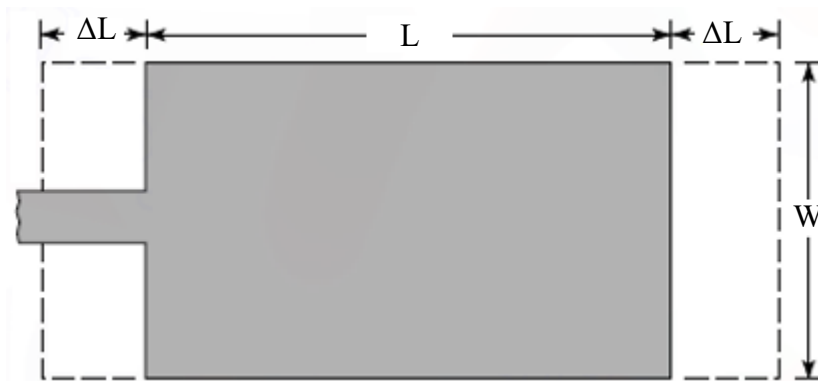


Figure 2.18 Physical dimension of patch antenna and fringing field [1]

Equation 2.27 gives the mathematical calculation of ΔL [9]:

$$\frac{\Delta L}{h} = 0.412 \frac{(\epsilon_{reff}+0.3)\left(\frac{W}{h}+0.264\right)}{(\epsilon_{reff}-0.258)\left(\frac{W}{h}+0.8\right)} \quad (2.27)$$

Accordingly, patch's length and width can now be calculated via the following equations [9]:

$$L = \frac{c_0}{2f_r \sqrt{\epsilon_{reff}}} - 2\Delta L, \quad W = \frac{c_0}{2f_r} \sqrt{\frac{2}{\epsilon_{r+1}}} \quad (2.28)$$

where L: Length, W: Width, c_0 : Speed of light in vacuum, ϵ_r : Dielectric substrate, f: Operation frequency

Then, resonance frequency of the patch antenna for the mode TM_{mn} is calculated as [9]:

$$f_0 = \frac{c_0}{2\sqrt{\epsilon_{reff}}} \left[\left(\frac{m}{L}\right)^2 + \left(\frac{n}{W}\right)^2 \right]^{\frac{1}{2}} \quad (2.29)$$

where c_0 : Speed of light in vacuum, ϵ_{reff} : Effective Dielectric constant, L: Length of the patch antenna, W: Width of the patch antenna, m, n: operating modes along the L and W

The width of microstrip line, which is associated with the characteristic impedance, can be calculated via equation 2.30 [70]:

$$Z_0 = \begin{cases} \frac{60}{\sqrt{\epsilon_{reff}}} \ln \left[\frac{8h}{W_f} + \frac{W_f}{4h} \right] & \text{for } W_f/h \leq 1 \\ \frac{120\pi}{\sqrt{\epsilon_{reff}} \left[1.393 + \frac{W_f}{h} + \frac{2}{4 \ln \left(\frac{W_f}{h} + 1.444 \right)} \right]} & \text{for } \frac{W_f}{h} > 1 \end{cases} \quad (2.30)$$

where Z_0 [ohm]: Characteristic impedance, L_p [mm]: Length of the patch antenna, F_i [mm]: Inset depth of the patch antenna, W_f : The width of microstrip line

Here, there is an important fact that the ratio of W_f/h is calculated by taking the characteristic impedance Z_0 , dielectric constant ϵ_r and the substrate's thickness h into account [1]:

$$\frac{W_f}{h} = \begin{cases} \frac{8e^A}{e^{2A}}, & \text{for } \frac{W_f}{h} < 2 \\ \frac{2}{\pi} \left[B - 1 - \ln(2B - 1) \frac{\epsilon_r - 1}{2\epsilon_r} \left\{ \ln(B - 1) + 0.39 - \frac{0.61}{\epsilon_r} \right\} \right], & \text{for } \frac{W_f}{h} > 2 \end{cases} \quad (2.31)$$

where $A = \frac{Z_0}{60} \sqrt{\frac{\epsilon_r + 1}{2}} + \frac{\epsilon_r - 1}{\epsilon_r + 1} \left(0.23 + \frac{0.11}{\epsilon_r} \right)$ $B = \frac{377\pi}{2Z_0\sqrt{\epsilon_r}}$

Equation 2.32 gives the calculation of the feed length [9]:

$$L_f = \frac{\lambda_0}{4\sqrt{\epsilon_r}}, \quad \frac{\lambda_0}{\sqrt{\epsilon_r}} = \lambda_g \quad (2.32)$$

where λ_g : guide wavelength

2.5 Antenna Array Theory

The array antennas are promising techniques to satisfy the requirements of modern antenna systems such as RADAR and satellites [8]. The array antenna is desirable since it radiates the energy in a particular direction in order to maximize the signal power. They are consisting of multiple stationary antennas called as the antenna elements which can be identical or different in terms of shape, material, etc [1]. However, due to relatively simpler design and fabrication, identical array antennas are usually preferred. The individual element may be any type such as microstrip patch antenna, wires dipoles, etc. The array antenna gives the best solution in terms of enhancement of directional gain and allocation of power to beams. The amplitude and the phase of the beam can be controlled by creating a phased array [8]. The main advantage of these sort of arrays is to control the amplitude and the phase of each antenna element in the array. This implies that the array antenna can be equivalent to a mechanically rotating antenna without the requirements of moving part. On the other hand, the main drawback of array antennas is the complexity of their architecture and high cost. The general procedure of pattern designs in the array antenna consists of several variables which can be changed to achieve the overall array pattern.

There are five control variables that might be used to shape the overall pattern of the antenna as follow [1]:

- Geometrical Configuration
- Array Layout (Placement of array elements)
- Excitation amplitude of each Element
- Excitation phase of each Element
- Patterns of array elements

The array architecture has a vital role in today’s wireless communication in terms of obtaining low-cost and high-performance systems in parallel with the desired purpose. The continuous growth in this field has become advantageous for the design of today’s array antenna which can be divided into several categories with respect to design parameters such as geometrical configuration, array layout, feed mechanism and beamforming architecture. Each category is also broadly subdivided into several classes according to the design procedure. Figure 2.19 represents the categories that are used in this thesis project.

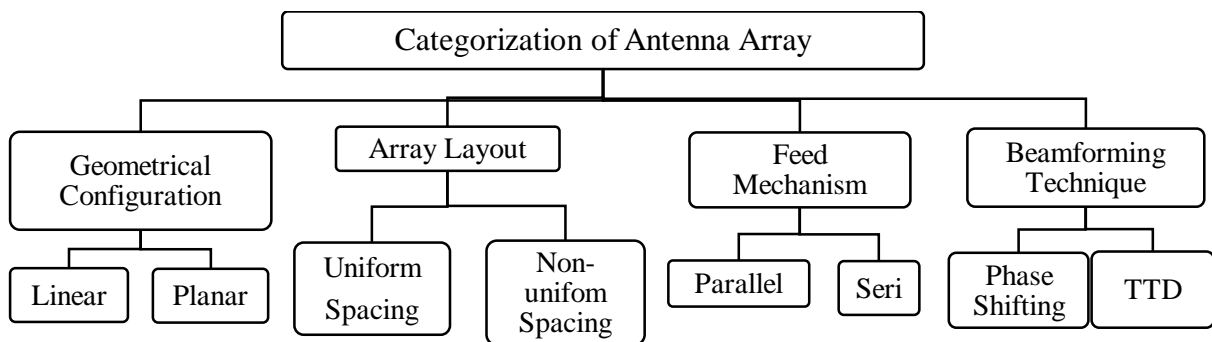


Figure 2.19 Categorization of antenna array

2.5.1. Geometrical Configuration

There are different types of arrays which are Linear, Planar and Circular.

- Linear Array: The antenna elements are arranged along a straight line.
- Planar Array: The antenna elements are arranged to over some planar surface such as a rectangular array.
- Circular Array: The antenna elements are arranged along a circular ring.

Figure 2.20 illustrates a few examples of one- and two-dimensional arrays consisting of identical antennas [11]. Each of these configurations have different characteristics.

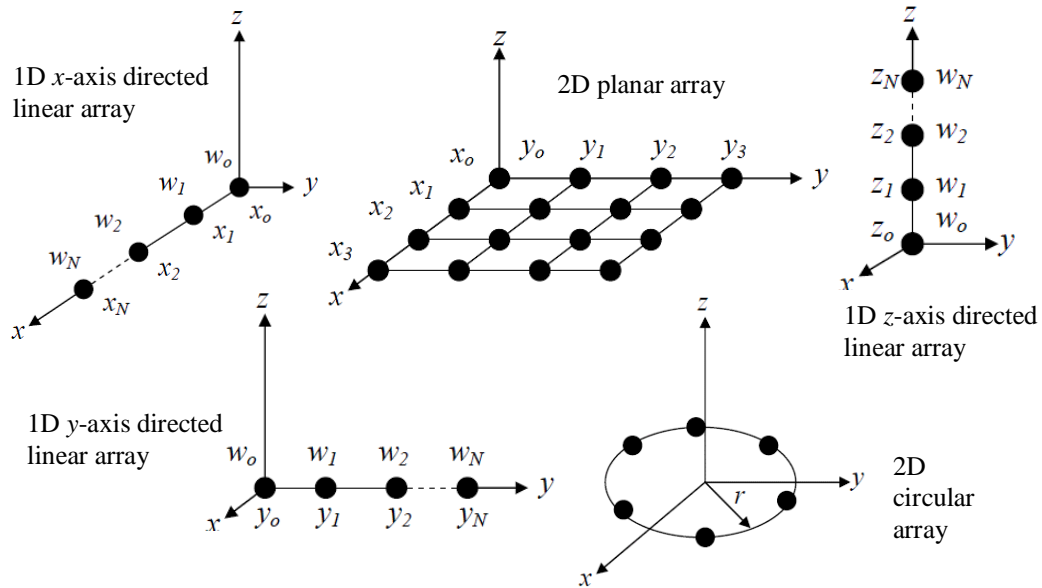


Figure 2.20 Different arrangement of an antenna array [11]

The position of array elements is represented by the antenna spherical coordinate system as illustrated by Figure 2.21. The angle ϕ refers to the azimuthal (x-y) plane which is defined with respect to the +x axis and is rotated in the x-y plane about the z axis for $0 < \phi < 2\pi$. Besides, θ refers to the elevation (z) plane which is defined with respect to the +z-axis and is defined for $0 < \theta < \pi$ [11].

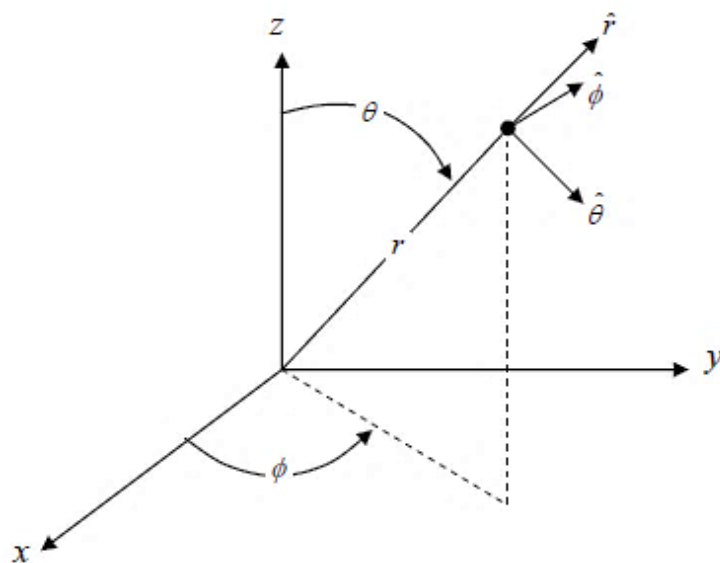


Figure 2.21 Antenna Coordinate System [11]

There are two key factors utilized to represent the total radiation pattern of an antenna array in the far-field $E(\theta, \phi)$: **Element Factor $EF(\theta, \phi)$** and **Array Factor $AF(\theta, \phi)$** . $EF(\theta, \phi)$, which depends on physical dimensions and electromagnetic characteristics, represents the radiation pattern of an individual element in the array. $AF(\theta, \phi)$, which depends on the amplitude, phase and position of the elements, represents the radiation pattern of an array composed of isotropic elements. The functional relationship of these factors is given by equation 2.33 [8, 12] and 2.34 [13].

$$G(\theta, \phi) = AF(\theta, \phi) \cdot G_e(\theta, \phi) \quad (2.33)$$

$$G(\theta, \phi) = AF(\theta, \phi) + G_e(\theta, \phi) \text{ in dB} \quad (2.34)$$

where $G(\theta, \phi)$: Array's radiation pattern, $AF(\theta, \phi)$: Array Factor, $G_e(\theta, \phi)$:Element Factor

Figure 2.22 illustrates the array radiation pattern of horizontal and vertical oriented two short dipole arrays separated by $d = \lambda/2$ as a result of pattern multiplication.

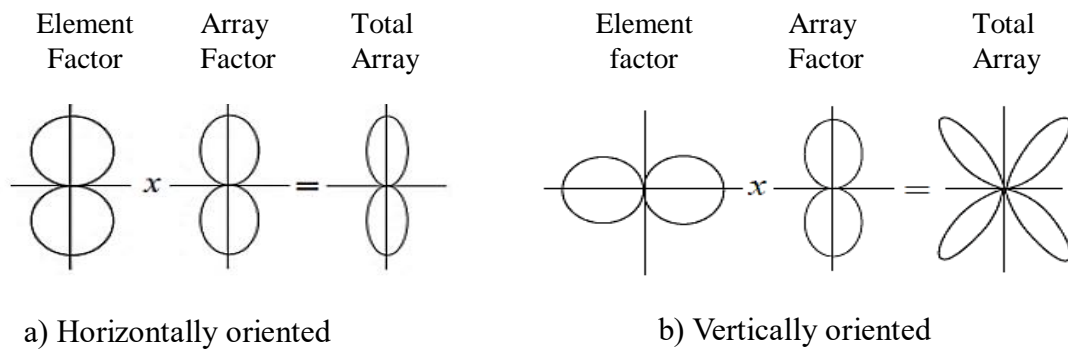


Figure 2.22 Pattern Multiplication [14]

Pattern multiplication allows performing the array design only focusing on the synthesis of the function $AF(\theta, \phi)$ without prior selection of the radiating elements, avoid the use of full-wave simulations to analyse the whole array response and enable to analyse irregular and unconventional array configurations [15].

2.5.1.1 Linear Array Along Z-Axis

In order to give a better physical interpretation of the theory, N- element array along a line (z axis) are considered as shown in Figure 2.23. The total field of this array, assuming no mutual coupling effect between the elements [1,8], is determined by the vector addition of the fields radiated by the individual elements. Here, r_1, r_2, \dots, r_N represent the distance of the individual element to the far-field observation point and d_1, d_2, \dots, d_N represent the distance of each array elements from the first (reference) element.

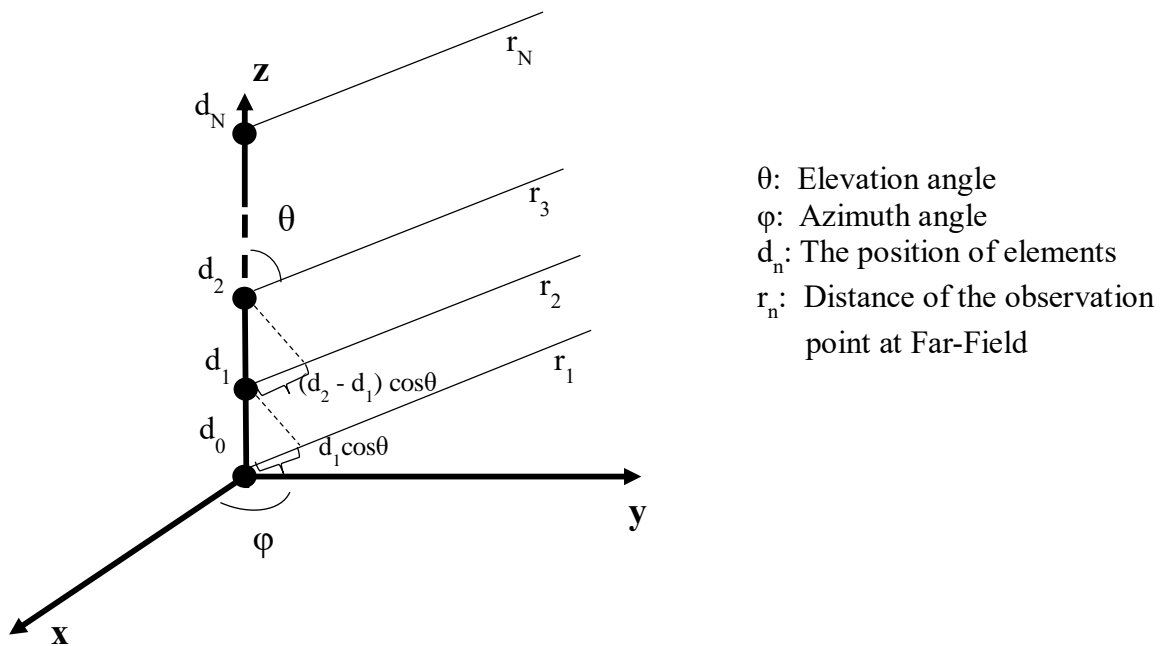


Figure 2.23 Linear array along z axis

Accordingly, the far electromagnetic fields of the first elements is calculated as follows [1]:

$$E_1 = I_0 \frac{e^{-jkr_1}}{4\pi r_1} \quad (2.35)$$

where E_1 : The field of an isotropic radiator located at the origin, I_0 : Excitation of the isotropic radiator, r_1 : Distance of the observation point from the origin, k : wave number = $2\pi/\lambda$, λ : wavelength

In addition to this, the current magnitudes of the array elements are supposed to be equal and the current on the array element located at the origin is considered as the phase reference (zero phase). Thus,

$$I_1 = I_0, \quad I_2 = I_0 e^{j\beta_2}, \quad \dots, \quad I_N = I_0 e^{j\beta_N} \quad (2.36)$$

where β represents the phase difference of the signals in adjacent elements. Antenna arrays can be controlled by the relative phase β between the elements.

It is explicitly seen from Figure 2.23 that the path length of the wave received at element 1 is greater than the path length of element 2. This path length difference effects directly the propagation of wave whether the waves interfere constructively or destructively. Assume the array is in far field, the path length will become approximately parallel that allows to use simple trigonometry to define path difference.

Since the field point is in the far field, the vectors from elements are assumed parallel. If the signals arrive from angle θ to the antenna boresight, then according to geometry in Figure 2.23, the relationship of individual elements' distances from the observation point is formed by the reference distance r_1 as follows:

$$r_2 = r_1 - d_1 \cos\theta, \quad (2.37)$$

$$r_3 = r_2 - (d_2 - d_1) \cos\theta \Rightarrow r_3 = r_1 - d_2 \cos\theta \quad (2.38)$$

⋮

$$r_N = r_1 - d_{N-1} \cos\theta \quad (2.39)$$

It should be noted that $d \cos\theta \ll r$. Therefore, the subtraction in the denominator of equations (2.40-42) can be ignored in order to calculate the far electromagnetic fields of other elements.

Hence,

$$E_2 = I_0 e^{j\beta_2} \frac{e^{-jk(r_1 - d_1 \cos\theta)}}{4\pi(r_1 - d_1 \cos\theta)} \Rightarrow E_2 = E_1 e^{j(\beta_2 + kd_1 \cos\theta)} \quad (2.40)$$

$$E_3 = I_0 e^{j\beta_3} \frac{e^{-jk(r_1 - d_2 \cos\theta)}}{4\pi e^{-jk(r_1 - d_2 \cos\theta)}} \Rightarrow E_3 = E_1 e^{j(\beta_3 + kd_2 \cos\theta)} \quad (2.41)$$

⋮

$$E_N = I_0 e^{j\beta_N} \frac{e^{-jk(r_1 - d_{N-1} \cos\theta)}}{4\pi(r_1 - d_{N-1} \cos\theta)} \Rightarrow E_N = E_1 e^{j(\beta_N + kd_{N-1} \cos\theta)} \quad (2.42)$$

Then, the overall array far field is calculated using superposition:

$$E_t = \sum_{m=1}^N E_m \Rightarrow E_t = E_1 [1 + e^{j(\beta_2 + kd_1 \cos\theta)} + \dots + e^{j(\beta_N + kd_{N-1} \cos\theta)}] \quad (2.43)$$

It is apparent from the equation (2.43) that the total field of the array is equal to the field of a single element positioned at the origin (E_1) multiplied by a factor which is known as the **Array Factor**.

$$AF = [1 + e^{j(\beta_2 + kd_1 \cos\theta)} + \dots + e^{j(\beta_N + kd_{N-1} \cos\theta)}] \quad (2.44)$$

The array factor of a linear array along z axis is obtained as:

$$AF = \sum_{n=0}^{N-1} e^{j(kd_n \cos\theta + \beta_n)} \quad (2.45)$$

where k: the wave propagation constant ($k=2\pi/\lambda$), d_n : distance of n^{th} element from the reference.
N: Total number of elements in the array, β : Phase Shift

2.5.1.2 Linear Array Along X- or Y- Axis

In this part, the aim is to show the solution of the antenna array which may be oriented either in y-z plane or x-z plane. In Figure 2.24, \hat{a}_r is the unit vector of position vector r (the unit vector along the direction of the incoming signal) and γ is the angle between the array axis and the position vector.

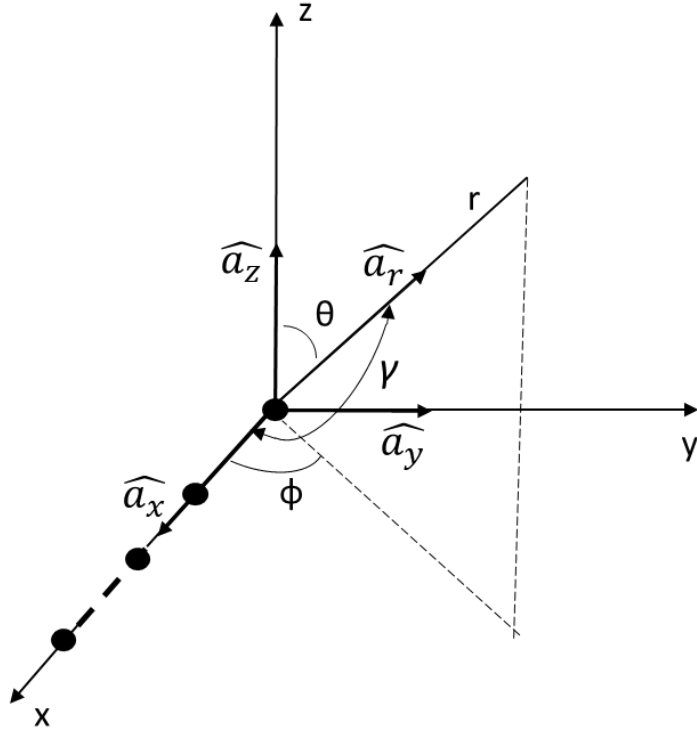


Figure 2. 24 Linear array of N isotropic elements positioned along the x-axis [1,11].

According to Figure 2.24,

$$\widehat{a}_r = \sin \theta \cos \phi \widehat{a}_x + \sin \theta \sin \phi \widehat{a}_y + \cos \theta \widehat{a}_z \quad (2.46)$$

where $\widehat{a}_x, \widehat{a}_y, \widehat{a}_z$ are unit vectors along the relevant axis.

Hence, for an array along x-axis [1,17]:

$$\cos \gamma = \widehat{a}_x \cdot \widehat{a}_r \quad (2.47)$$

$$\cos \gamma = \widehat{a}_x (\sin \theta \cos \phi \widehat{a}_x + \sin \theta \sin \phi \widehat{a}_y + \cos \theta \widehat{a}_z) \quad (2.48)$$

$$\Rightarrow \cos \gamma = \sin \theta \cos \phi \quad (2.49)$$

For an array along y-axis:

$$\cos \gamma = \widehat{a}_y \cdot \widehat{a}_r \quad (2.50)$$

$$\cos \gamma = \widehat{a}_y (\sin \theta \cos \phi \widehat{a}_x + \sin \theta \sin \phi \widehat{a}_y + \cos \theta \widehat{a}_z) \quad (2.51)$$

$$\Rightarrow \cos \gamma = \sin \theta \sin \phi \quad (2.52)$$

For an array along z-axis:

$$\cos\gamma = \widehat{a}_z \cdot \widehat{a}_r \quad (2.53)$$

$$\cos\gamma = \widehat{a}_z (\sin\theta \cos\phi \widehat{a}_x + \sin\theta \sin\phi \widehat{a}_y + \cos\phi \widehat{a}_z) \quad (2.54)$$

$$\Rightarrow \cos\gamma = \cos\theta \quad (2.55)$$

Considering all of the above, the array factor for an array along y-axis and z-axis are calculated as follows:

$$\text{Array Factor of a linear array along x axis : } AF = \sum_{n=0}^{N-1} e^{j(kd_n \sin\theta \cos\phi + \beta_n)} \quad (2.56)$$

$$\text{Array Factor of a linear array along y axis : } AF = \sum_{n=0}^{N-1} e^{j(kd_n \sin\theta \sin\phi + \beta_n)} \quad (2.57)$$

$$\text{Array Factor of a linear array along z axis : } AF = \sum_{n=0}^{N-1} e^{j(kd_n \cos\theta + \beta_n)} \quad (2.58)$$

In general, array factor can be written as:

$AF = \sum_{n=0}^{N-1} e^{j(\psi)}$	<p>where ψ: Phase function, the real part of the exponential function that varies depending upon the axis. (2.59)</p> <p>n: nth element from the reference</p> <p>N: Total number of elements in the array</p>
-------------------------------------	---

To sum up, array factor characterizes each element with respect to experienced phase shifts and coordinate origin. The factor of e^{jkr} is coming from the single antenna at origin that common all term of antenna array and it says that radiation pattern of an antenna array will be product of radiation pattern of single antenna.

2.5.1.3 Planar Array

Besides placing along a line, array elements can be positioned in rectangular grid as illustrated by Figure 2.25. Unlike linear arrays, planar arrays scan the main beam along both θ and ϕ and thereby possess some additional advantages such as higher gain, lower sidelobes. These sorts of improvements are given thoroughly in Chapter 3 via simulation results.

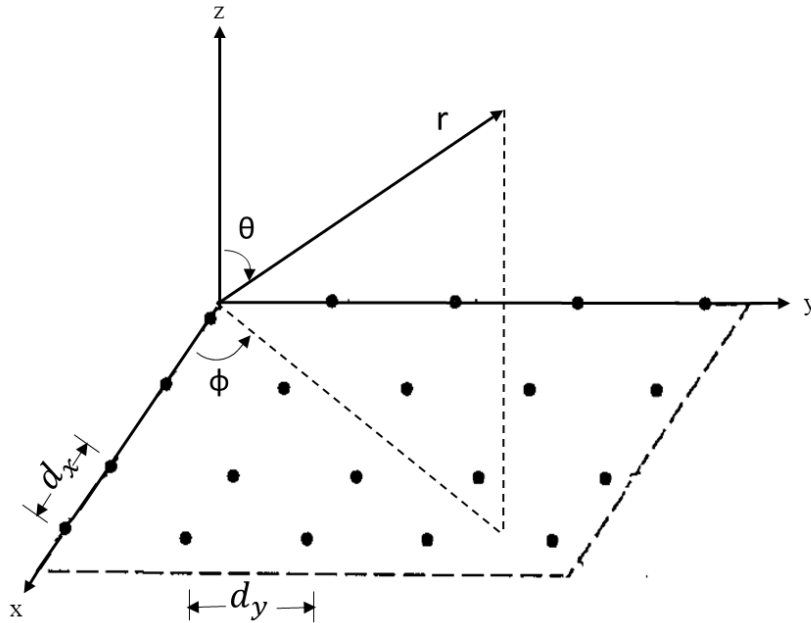


Figure 2.25 Planar array geometry [1]

The design principles and the derivation of array factor for planar arrays are similar to those presented earlier for the linear arrays. If N elements are initially placed along y axis, the array factor of this linear array is expressed with respect to aforementioned equation 2.57 as:

$$AF = \sum_{n=0}^{N-1} e^{j(kd_n \sin\theta \sin\phi + \beta_n)} \quad (2.60)$$

Now, if M elements such arrays are placed next to each other in the x - direction, the array factor for the entire planar array can be expressed as [1, 17]:

$$AF = \sum_{m=0}^{M-1} \left[\sum_{n=0}^{N-1} e^{j(kd_n \sin\theta \sin\phi + \beta_n)} \right] e^{j(kd_m \sin\theta \cos\phi + \beta_m)} \quad (2.61)$$

The equation 2.61 can then be separated into the product of two terms as follows:

$$AF = \sum_{m=0}^{M-1} e^{j(kd_m \sin\theta \cos\phi + \beta_m)} \sum_{n=0}^{N-1} e^{j(kd_n \sin\theta \sin\phi + \beta_n)} \quad (2.62)$$

More general, array factor of a planar array can be written as the product of the array factors of linear arrays in the x- and y- directions:

$$AF_{planar} = AF_{linear \text{ along } x\text{-axis}} * AF_{linear \text{ along } y\text{-axis}} \quad (2.63)$$

2.5.2 Array Layout

Modern applications in today's communication engineering field require the phased array with multiple functionalities, larger bandwidth, smaller size, reduced weight and lower costs. Various array layouts, i.e. unequal spacing between adjacent elements, can help to possess these extra capabilities with higher gain and potentially reduced side lobe levels (SLL). In this thesis, the phased arrays are structured either as uniform (equal inter-element spacing) array or non-uniform (unequal inter-element spacing) array. As already mentioned in Chapter 2.2, the radiation pattern is a function of the angular distribution of radiated electric field voltage or power enforced in a particular angle in space and it consists of several lobes which characterize specific angular regions where a main beam of the array radiation is directed. There are five lobes exist in radiation pattern as follows:

- Major lobes: The point where the maximum direction of propagation is directed.
- Minor lobes: These are any lobes other than major lobes. The minor lobes are divided itself three sub-lobes which are:
 - Side lobes: Any lobe with radiation in the same hemisphere of the main beam. It represents the radiating energy in unintended directions. Side lobes are undesirable and the reduction of side lobe is one of the main targets for antenna array applications.
 - Back lobe: A lobe with radiation direction directly opposite to the main lobe.
 - Grating lobes: These are side lobes that are equal to main beam which is totally undesirable.

Grating lobes may appear in case the inter-element spacing is not chosen attentively (i.e. spacing greater than the wavelength) as it is illustrated by Figure 2.26. Different spacing arrangements are given in Chapter 3 in detail.

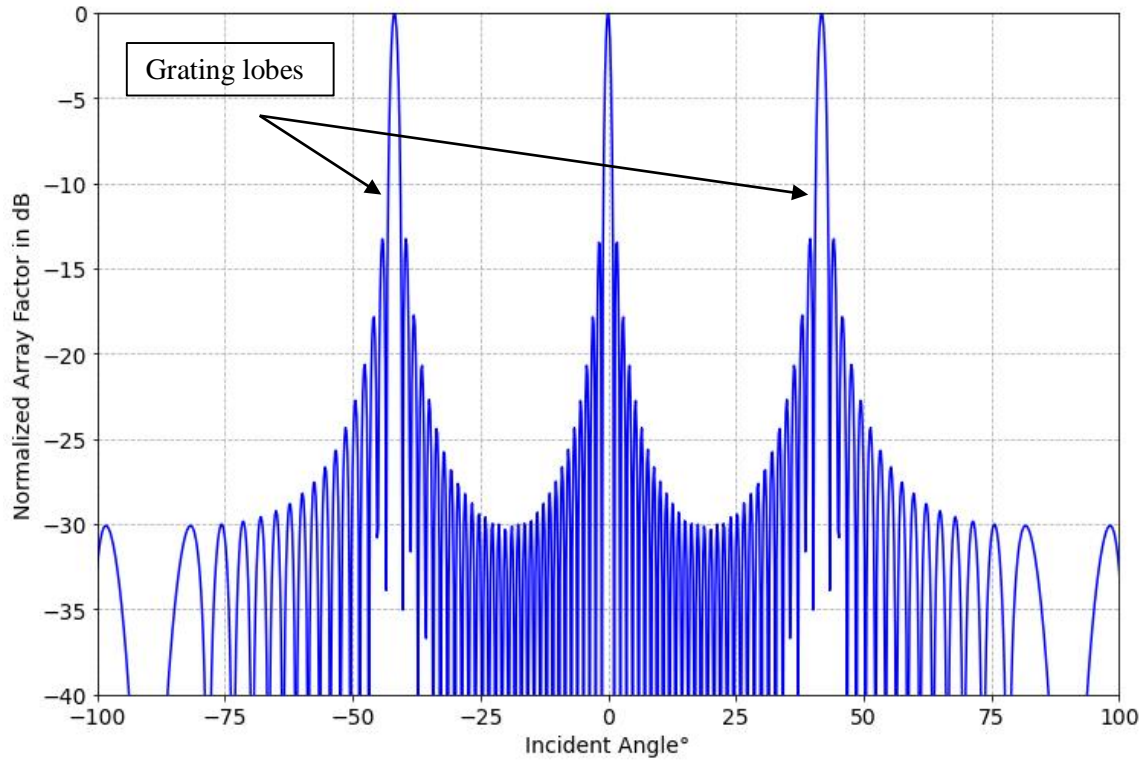


Figure 2.26 Normalized Array Factor for $d=1.5\lambda$, $N=32$

2.5.2.1 Uniformly Spaced Array

It is quite common phenomenon to have equal spacing between adjacent elements in array antennas. On the other hand, non-uniform spacing may be considered in order to obtain a desired beamwidth with considerably fewer elements than an equal spaced array [8]. This fact is also proved in Chapter 3 via simulations of the array factor patterns for both cases.

For uniformly spaced arrays, the element locations are converted to $d_n = nd$ where d is the uniform distance between the elements. In this case, the array factor becomes:

$$AF = \sum_{n=0}^{N-1} e^{j(n\psi)} \quad \text{where } \psi: \text{ the real part of the exponential function varies} \quad (2.64)$$

depending upon the axis. n : n^{th} element from the reference

N : Total number of elements in the array

In literature [1, 8, 13], the array factor is also expressed many times in a compact and closed form as a result of simple mathematical conversion:

$$AF = [1 + e^{j\psi} + e^{j2\psi} + e^{j3\psi} \dots + e^{j(N-1)\psi}] \quad (2.65)$$

Multiply both sides of equation 2.65 by $e^{j\psi}$ and subtract from both sides the original array factor expression:

$$e^{j\psi}AF - AF = AF(1 + e^{jn\psi} + e^{j2n\psi} + e^{j3n\psi} \dots + e^{j(N-1)\psi}) - AF \quad (2.66)$$

$$\Rightarrow AF (e^{j\psi} - 1) = e^{jN\psi} - 1 \quad (2.67)$$

Then,

$$AF = \frac{e^{jN\psi} - 1}{e^{j\psi} - 1} = \frac{e^{j\frac{1}{2}N\psi} (e^{j\frac{1}{2}N\psi} - e^{-j\frac{1}{2}N\psi})}{e^{j\frac{1}{2}\psi} (e^{j\frac{1}{2}\psi} - e^{-j\frac{1}{2}\psi})} \quad (2.68)$$

According to Euler's rule, equating 2.67 can be expressed in sinus form:

$$\Rightarrow AF = e^{j(\frac{N-1}{2})\psi} \frac{\sin(\frac{1}{2}N\psi)}{\sin(\frac{1}{2}\psi)} \quad (2.69)$$

The coefficient of $\frac{N-1}{2}$ in the term $e^{j(\frac{N-1}{2})\psi}$ represents the physical centre of the array. This array centre launches a $\frac{N-1}{2}\psi$ phase shift. If the position of the array shifted and the array centre is located at the origin, the physical centre is at 0 and this phase factor can be neglected.

Then, equation 2.69 can be rewritten as:

$$AF = \frac{\sin(\frac{1}{2}N\psi)}{\sin(\frac{1}{2}\psi)} \quad (2.70)$$

where AF_n : Array factor of uniformly spaced array, N: Number of Elements, ψ : Phase Function

There is an important fact the maximum array factor (when the first derivative of equation 2.70 is 0) exists when $\psi = 0$. That causes to have an indeterminate form as $AF = \frac{0}{0}$. Thus, L'Hôpital's rule must be applied to be able to get maximum value of Array Factor. In this case;

$$AF_{max} = \lim_{\psi \rightarrow 0} \frac{\frac{d\psi}{dAF} \sin(\frac{1}{2}N\psi)}{\frac{d\psi}{dAF} \sin(\frac{1}{2}\psi)} \Rightarrow AF_{max} = N \quad (2.71)$$

As it is seen from equation 2.71, the maximum array factor would occur with respect to the number of elements in the array. Figure 2.27 illustrates this behaviour for different values of N with the uniform element spacing of half wavelength.

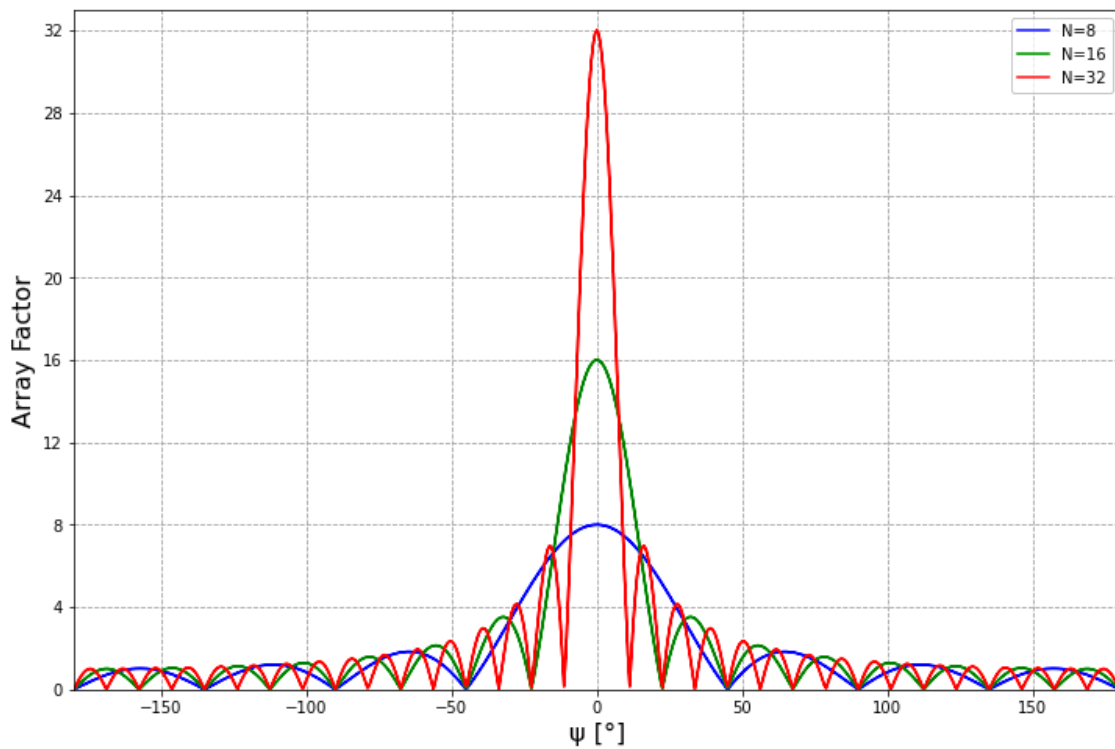


Figure 2.27 Array Factor vs Phase Function (ψ) Plot with $d=0.5\lambda$

In order to make the maximum value of AF unity for any N value, the normalized array factor must be considered by multiplying the function with $\frac{1}{N}$ as follows:

$$AF_n = \frac{1}{N} \frac{\sin(\frac{1}{2}N\psi)}{\sin(\frac{1}{2}\psi)} \quad (2.72)$$

where AF_n : Normalized array factor, N: Number of Elements, ψ : Phase function

Figure 2.28 depicts the plot of normalized array factor and the phase function with the uniform element spacing of half wavelength. It should be noted that a higher N gives a narrower major lobe as well as lower side lobe levels which leads to have higher directivity.

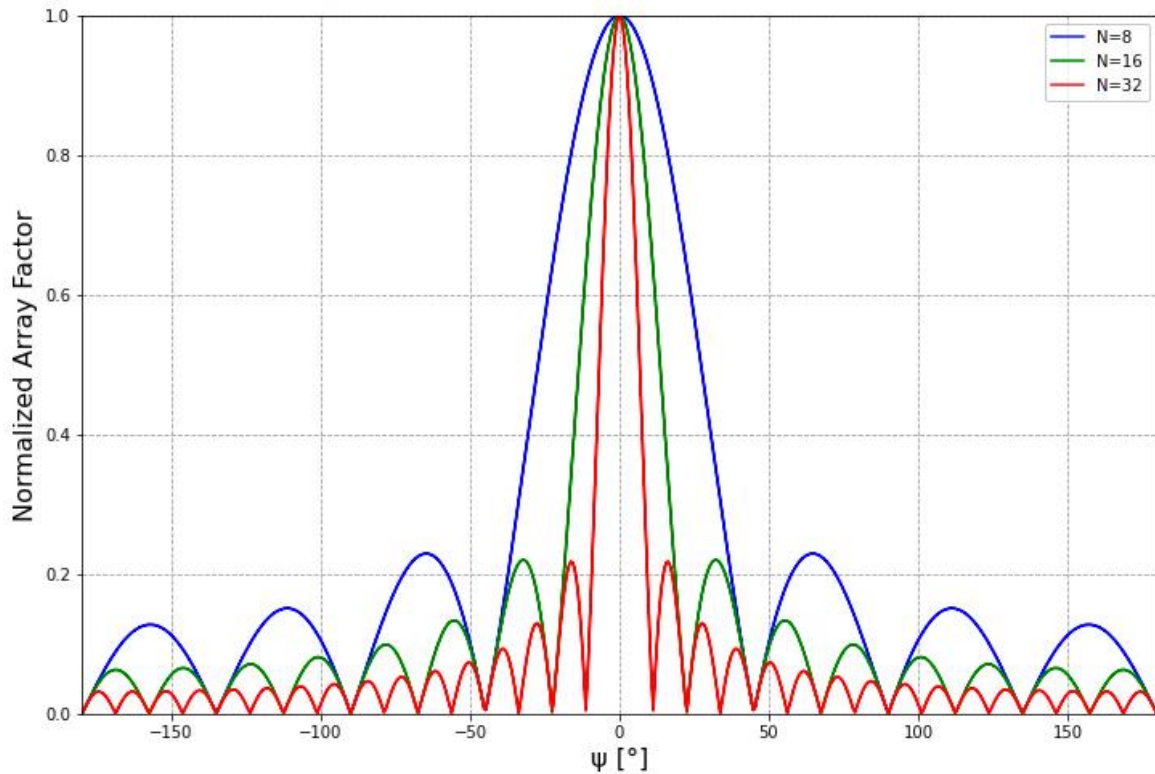


Figure 2.28 Normalized Array Factor vs Phase Function (ψ) Plot with $d=0.5\lambda$

All plots given in Chapter 3 are created in accordance with this methodology. At this point, it must be noted that these plots are all sketched with respect to the phase function which is varied by the corresponding axis as already described in equation 2.59. As illustrated by Figures 2.26-27-28, the major lobe occurs when the phase function is equal to zero. By varying phase shift (β), the direction of the major lobe can be steered. This is called beam (phase) steering which is thoroughly explained in Section 2.4.3.

Furthermore, normalized array factor is generally expressed by dB unit which is desirable because a logarithmic scale gives point in more details to the pattern with very low values (i.e. minor lobes). Accordingly, Figure 2.29 demonstrates the normalized array factor in dB.

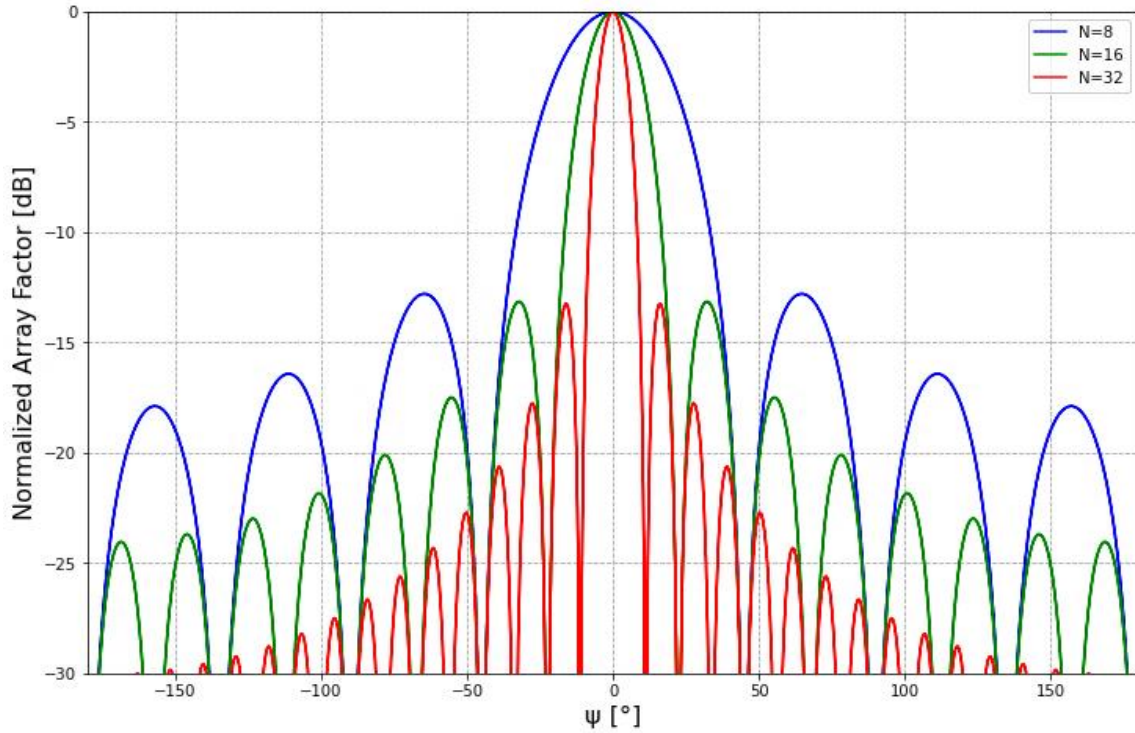
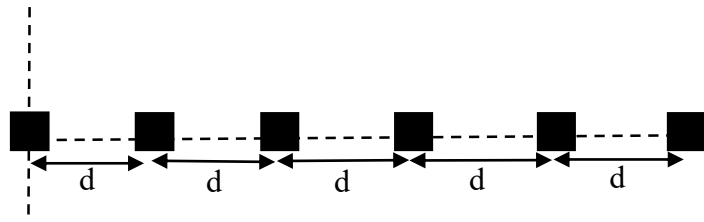


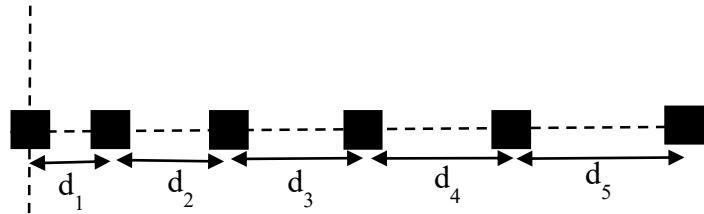
Figure 2.29 Normalized Array Factor in dB vs Phase Function (ψ) with $d=0.5\lambda$

2.5.2.2 Non-Uniformly Spaced Array

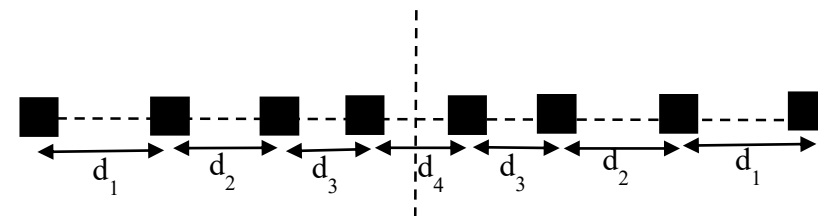
The SLL can be reduced to any desired level by two well-known methods: weighting the amplitude of the element's excitation or utilization of arbitrary element positioning [17]. There are different types of weighting methods such as Binomial, Blackman, Hamming, Gaussian and Kaiser-Bessel [16,17]. In this thesis work, arbitrary element positioning (unequal inter-element spacing) with fixed current distribution is taken into account since weighting the excitation requires a complicated feed system [18]. Accordingly, Tan et al. [32] propose two easily applicable methods for non-uniformly spaced arrays: Non-Uniformly Asymmetrical and Non-Uniformly Symmetrical placed arrays. Figure 2.30 illustrates three different geometrical configurations which are uniformly spaced array, non-uniformly asymmetrical spaced array and non-uniformly symmetrical array. If the number of radiating elements is kept constant, the non-uniformly spaced arrays become relatively larger because the elements are located with increased inter-element spacing to achieve the desired side lobe performance. However, fewer elements can also be used if the aim is to achieve comparable beamwidth as obtained with the uniformly spaced array.



a) Uniformly spaced Linear array



b) Non-Uniformly Asymmetrical Linear array



c) Non-Uniformly Symmetrical Linear array

Figure 2.30 Different Geometrical Configurations

The relation of each distance for non-uniform configurations are associated with ‘**increase rate**’ which is mathematically expressed as the difference between two successive positions of the array elements:

$$\text{increase rate} = d_n - d_{n-1} \quad (2.73)$$

2.5.3 Phased Array Antennas

The phased array antenna, which is also known as a smart antenna, is a directive antenna consisting of individual radiating elements that generate radiation pattern and provides flexibility to steer transmitted signals to the desired angle [33]. The use of phased array brings inevitable technology in a wide variety of applications to compensate the high propagation loss in mm-wave communication since it pioneers in achieving highly directive and steerable beams. The concept of the phased array is firstly introduced in the early 1940s [34] and mechanical rotation was initially being used for beam steering [35].

The technology gradually evolved from mechanically to electronically steering the beam which permits beams to be moved from point to point in space in just microseconds rather than seconds or longer [14]. The process by which phased array steers the beam is known as **beam steering** which can be accomplished by several techniques available for mm-wave applications as comprehensively presented by Uchendu and Kelly [36]. In this thesis work, **beamforming**, which is one of the well-known conventional techniques, is used. The term beamforming implies the process of combining signals from an array to form a highly directional beam of radiation. In other words, it aims to precisely align the phases of an incoming signal from different parts of an array to form a beam in a specific direction. This process is accomplished by implementing a time delay on each element's signal [37] which is illustrated in Figure 2.31. While this technique can be implemented for any array geometries, the following discussion refers to a uniformly spaced linear array with element spacing d along y - axis (for $\phi = 90^\circ$).

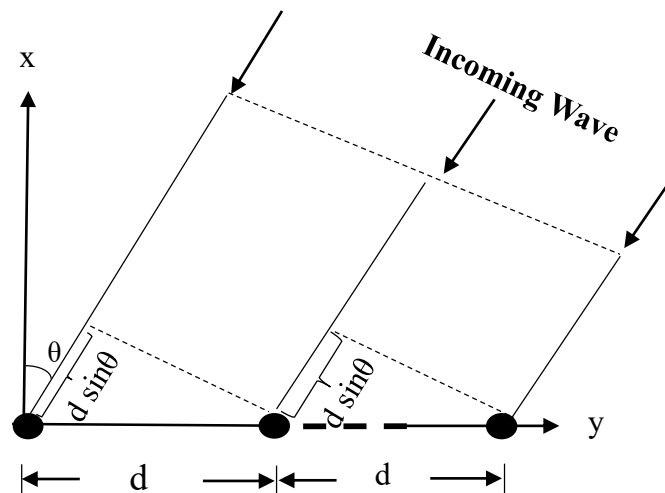


Figure 2.31 Illustration of time delay due to additional travel distance

If the signal arrives from an angle of θ off the antenna boresight, then the signal must travel an additional distance ($d \sin \theta$) to arrive at each successive element according to the geometry. Hence, the time delay per element in arrival becomes:

$$\Delta t = \frac{d \sin \theta}{c_0} \quad (2.74)$$

where Δt : Time delay, c_0 : Speed of light in vacuum, θ : Beam incoming angle

2.5.3.1 Beamforming Techniques

Beamforming is generally achieved by either phase shifters or true time delay (TTD) systems. Phased arrays consisting of phase shifters, which is known as **Analog RF beamforming** [10, 36], have been the conventional way of steering beams electronically over years. By changing the phase of each array element by phase shifters, the combined beam of the array is able to be steered. A Phase shifter is the device adds a constant phase difference to the signal through the operating frequency band without changing the signals' amplitude [39]. In other words, phase shifters at each array elements lead to change the relative phase among the elements. Figure 2.32 gives the basic schema of a linear array combined with phase shifters.

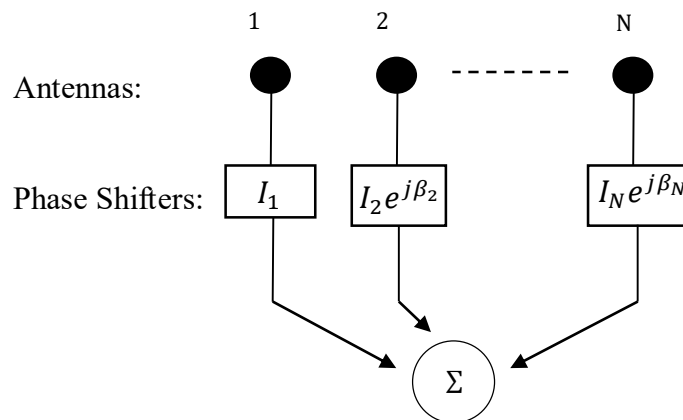


Figure 2.32 Basic Schema of a Phase scanned linear array [40]

The phase difference between adjacent elements, β , can be associated with the time delay in arrival as follows [13,41]:

$$\beta = 2\pi f \Delta t \Rightarrow \beta = \frac{2\pi d \sin \theta}{\lambda} \quad (2.75)$$

where Δt : Time delay, c : Speed of light in free space, θ : Beam arriving angle, λ : The wavelength of incoming signal, d : Inter-element spacing

In phase shifting method, a constant frequency dependent phase shift is produced to steer the array to a desired angle θ_0 . Accordingly, the array factor of N-element linear array via phase shifting is calculated by [40, 41]:

$$AF = \sum_{n=0}^{N-1} e^{j\left(\frac{2\pi}{\lambda}d_n \sin\theta - \frac{2\pi}{\lambda_0}d_n \sin\theta_0\right)} \quad (2.76)$$

where θ : Beam arriving angle, θ_0 : Beam steering angle, λ_0 : The wavelength at the design (center) frequency, λ : The wavelength of incoming signal, d_n : The position of the element

The phase shifting systems are not suitable for high-frequency applications due to the use of variable passive components that require amplifiers to compensate the gain variation [10]. Besides this, in case of a wide bandwidth requirement, the use of phase shifters is challenging because of their frequency-dependent characteristics. This results in **beam squint** which implies the change in beam direction across the RF signal's frequency. It causes a limitation for the applications at mm-wave frequencies where large bandwidth is fundamental. Beam squint, or in other words the beam direction deviation, can be calculated as [52]:

$$\Delta\theta = \arcsin\left(\frac{f_0}{f} \sin\theta_0\right) - \theta_0 \quad (2.77)$$

where $\Delta\theta$: Beam direction deviation, f_0 : Center frequency, f : signal frequency, θ_0 : Beam Steering angle

Equation 2.77 is graphically demonstrated in Figure 2.33 where the beam direction derivation is associated with the frequencies. According to the figure, few observations can be summarized as follows:

- A frequency above the center frequency results in a smaller deviation than a frequency below the center frequency.
- The deviation in beam angle increases as beam angle becomes greater.

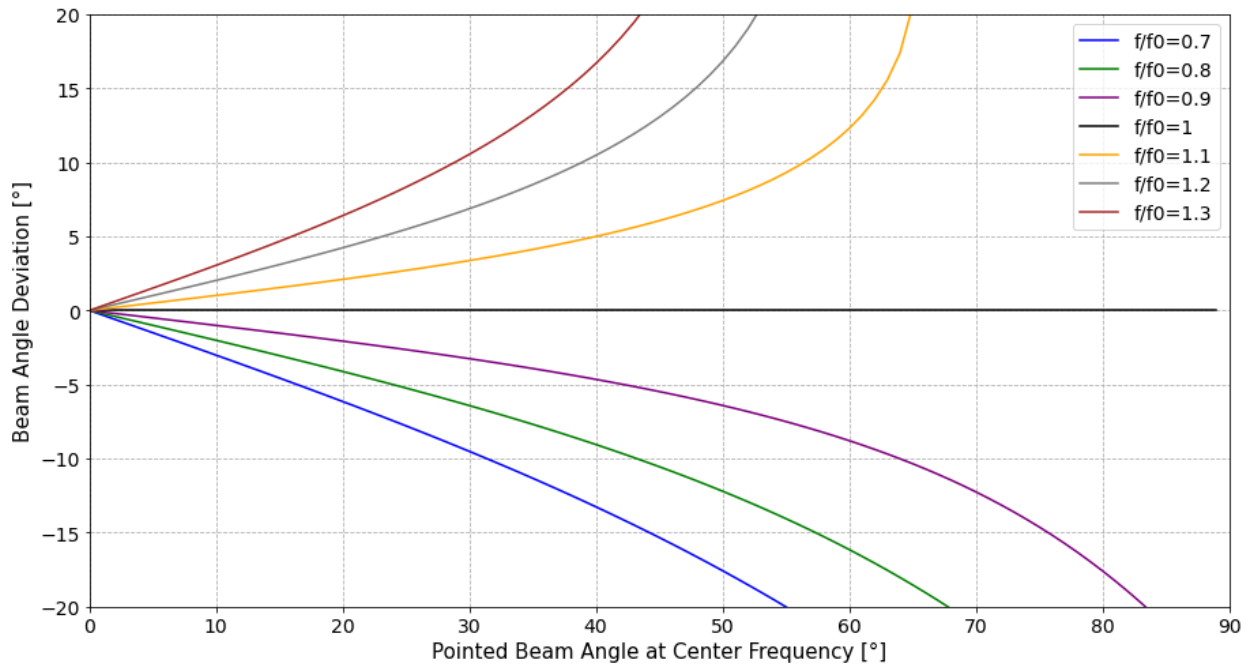


Figure 2.33 Beam direction deviation for several frequency deviations.

As a result of beam squint effect, phase compensation based on center frequency is replaced by TTD circuits to compensate for the wave path difference in arrival and to obtain enhanced bandwidth. The familiar way to provide time delays is to insert incremental lengths of transmission line (delay lines) of length ($L = dsin\theta$) [26]. There are two common techniques to implement the delay lines for TTD systems: Optical Delay Lines which uses optical fibers and Electronic Delay Lines which uses traditional microstrip lines or coax cable to delay the signal [41]. Figure 2.34 illustrates the basic schema where the time delay is varied for each element.

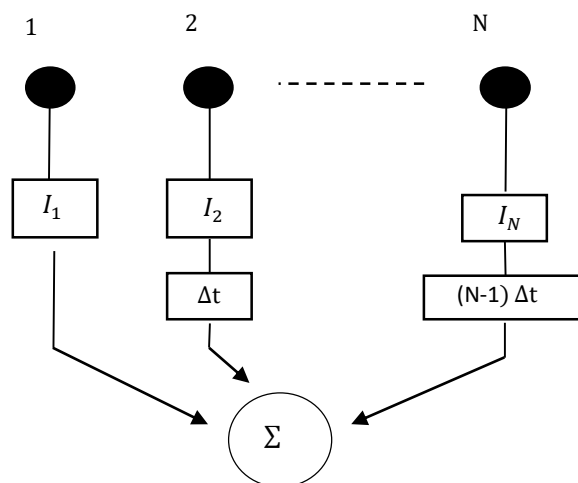


Figure 2.34 Basic Schema of a Time Scanned linear array [40]

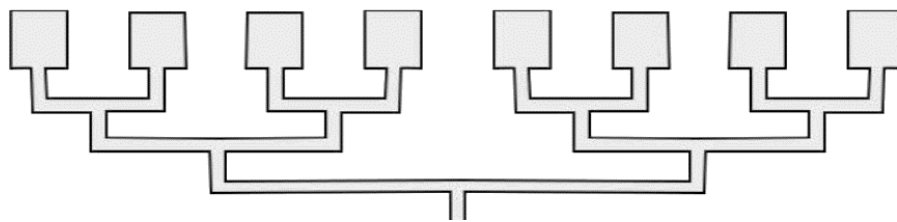
Accordingly, the array factor of N-element linear array via true time delay is calculated by [40]:

$$AF = \sum_{n=0}^{N-1} e^{j\left(\frac{2\pi}{\lambda}d_n(\sin\theta - \sin\theta_0)\right)} \quad (2.78)$$

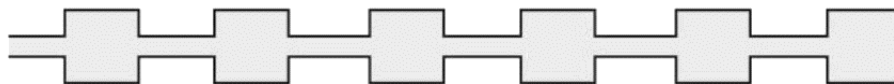
where θ : Beam arriving angle, θ_0 : Beam steering angle, λ : The wavelength of incoming signal, d_n : The position of the element

2.5.4 Antenna Array Feed Structure

The selection of a proper feed technique is another important quantity which has a vital role in the performance of the array in terms of bandwidth, beam angle, grating/side lobe level, the required antenna gain, power handling capacity and polarization [1]. In general, there are two common types of feed structure which are parallel and series feed network as illustrated in Figure 2.35.



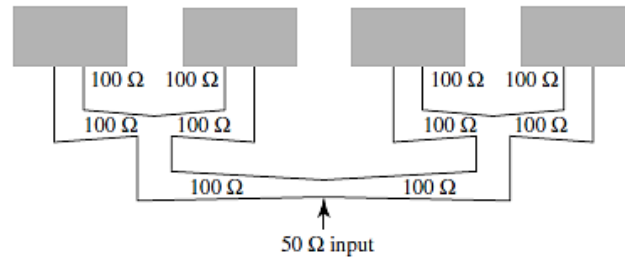
a) Parallel Feed Network



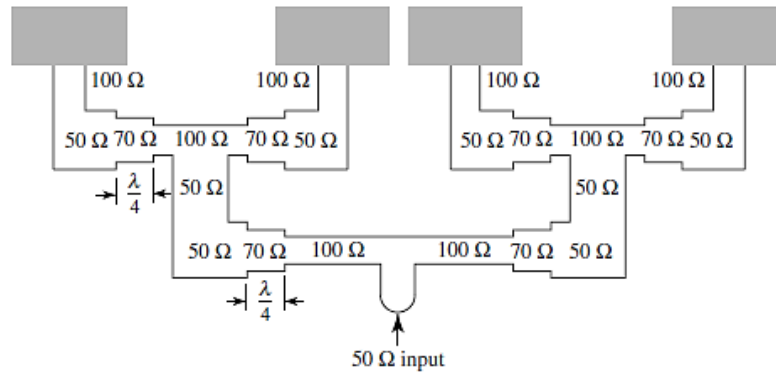
b) Series Feed network

Figure 2.35 Feed Arrangement for Microstrip Patch Antenna Array [1]

The parallel feed network is consisting of branching network of two-way power splitter. Those splitters can be made by tapered lines or quarter wavelength impedance transformers [1] which are shown in Figure 2.36



a) Tapered lines



a) $\lambda/4$ transformers

Figure 2.36 Tapered Lines and Quarter Wavelength Transformers [1]

The parallel feed configuration (also called as corporate feed) is more versatile and widely used in industry due to its advantages: The power is equally split at each junction, the beam position is independent of frequency [6] and provides more controllable feed of each element as well as beam direction by using suitable phasor and line extensions [1]. The independency of frequency makes the feed is broadband so that the bandwidth of parallel feed microstrip array is limited by two factors which are bandwidth of individual patch element and the impedance matching circuit of power dividing transmission such as quarter-wave transformer. The parallel feed can achieve a wider bandwidth than the series fed array network [1]. The disadvantage of parallel feed is related to the long transmission line between input port and the radiating elements which causes the large value of insertion loss [6]. On the other hand, in the series feed network, multiple elements are linearly arranged and fed serially by a single transmission line as shown in Figure 2.35 (b). The major advantage of series feed network is the lowest insertion loss but it has narrower bandwidth and weakest polarization control. The bandwidth is narrow because of transmission line goes through the patches that effects directly the phase between the adjacent elements. This phase is the function of transmission line length and patches' input impedance. Therefore, the phases are different for each array element. In this thesis project, the parallel feed network is preferred due to its aforementioned features.

2.5.5 Mutual Coupling

The development of reduced size radio transceivers has endorsed the emergence of small-size antenna arrays in recent years. Such new trends oblige the study of **mutual coupling** between the radiating elements which is an electromagnetic phenomenon that depends primarily on the radiation characteristic of the individual element, the array elements' orientation and the feed mechanism. The most significant effects occur on the antenna input impedance. Current in a single radiating element affects the phase and amplitude of the currents in neighbouring elements and thereby results in an interchange of radiated energy which limits the performance of the array antenna. Since the phases and amplitudes of the currents at each element change with scan angle, the mutual coupling is also influenced by scan angle. This should be noted that mutual coupling between the elements increases by decreasing the spacing between them. However, the spacing can not be increased superficially due to the existence of grating lobes. In recent years, lots of favourable methods have been proposed in the literature to bring down mutual coupling effect between the elements as given below:

- Grounded dielectric slab loaded by slot [42]
- Usage of metamaterial structure in between patches [43, 44]
- Defected ground structures in ground plane [45,46]
- Electromagnetic band gap (EBG) structures in between patches [47]

In this thesis project, no methods have been implemented regarding mutual coupling of the proposed arrays. This can be a further step that may be taken into account.

3.

SIMULATIONS & MEASUREMENTS

This chapter is split into two main parts: Theoretical simulation results obtained via developed **Python Simulator** which is solely based on the array factor theory and **3D HFSS tool** which is more realistic and comprehensive analysis based on ‘Floquet Model’ approach as thoroughly explained in [48,49].

3.1. Development of Python Simulator

Array factor patterns of proposed arrays were simulated with respect to fundamental equations given in Chapter 2.5 via Python simulator developed within the scope of this thesis project. It makes the process relatively faster to observe the behaviour of array pattern by assigning the essential input parameters such as inter-element spacing, geometrical array configuration, beam steering angle and beam steering technique. Given the simulator is based on theoretical foundation, it is not frequency dependant hence it can be used for wide frequency range. Figure 3.1 illustrates the graphical user interface which is an open source and publicly can be reached via: <https://github.com/Barkhausen-Institut/AntennaArraySimulator>.

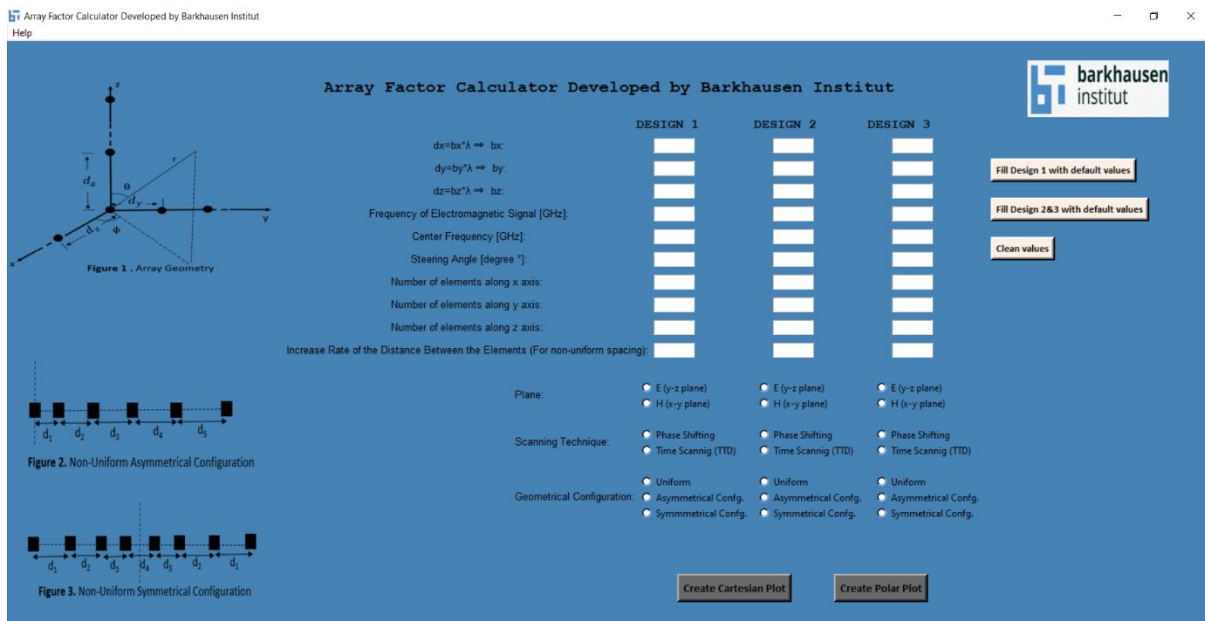


Figure 3.1 Graphical User Interface of Python Antenna Array Simulator

3.2 Effects of Essential Parameters

This subchapter examines the effect of essential parameters such as inter-element spacing, the total number of array elements, beam steering angle on the radiation pattern of the antenna array. All observations are also consistent with the results already reported in the literature [11,19-22]. These effects can be easily observed via Python Simulator without needing long HFSS simulations.

3.2.1 Inter-Element Spacing

This section aims to explicate why an element spacing of half wavelength ($\lambda/2$) is such a common metric in phased arrays. To demonstrate it, 32 element arrays with different inter-element spacing were simulated. Accordingly, Figure 3.2 exhibits the normalized array factor patterns of uniformly spaced linear broadside arrays which were computed using different values of inter-element spacing ranges from 0.25λ to 1.5λ . It is apparently seen that array structures with inter-element spacing below half-wavelength would produce excellent beam radiations. In contrast, the undesirable grating lobes occur when the inter-element spacing between the elements is greater than half wavelength. It is also observed that HPBW decreases with the increment in inter-element spacing.

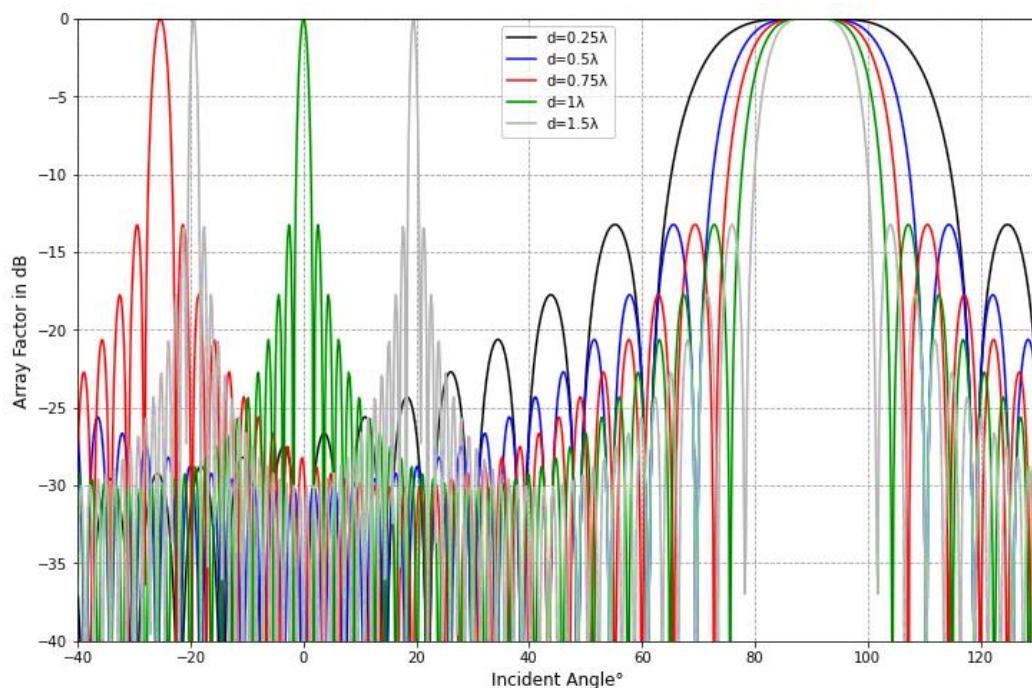


Figure 3.2 Normalized Array factor patterns of 32 element broadside uniform array along y-axis at different spacing

3.2.2 Effects of the Number of Elements in the Array

In this part, results were computed for the different number of elements at inter-element spacing of half wavelength. Figure 3.3 illustrates the comparison of arrays composed of different element numbers of 8,16 and 32. Accordingly, outstanding observations from this result can be summarized as follows:

- The higher number of elements in a large antenna array increases the number of side lobes in the AF pattern,
- Regardless of the number of elements in an array, the first sidelobe exists at -13dB. (Note: This is the case where the element number is greater than five [14].)
- The higher the number of elements, the lower the beamwidth.
- The number of nulls increases with the higher number of elements.

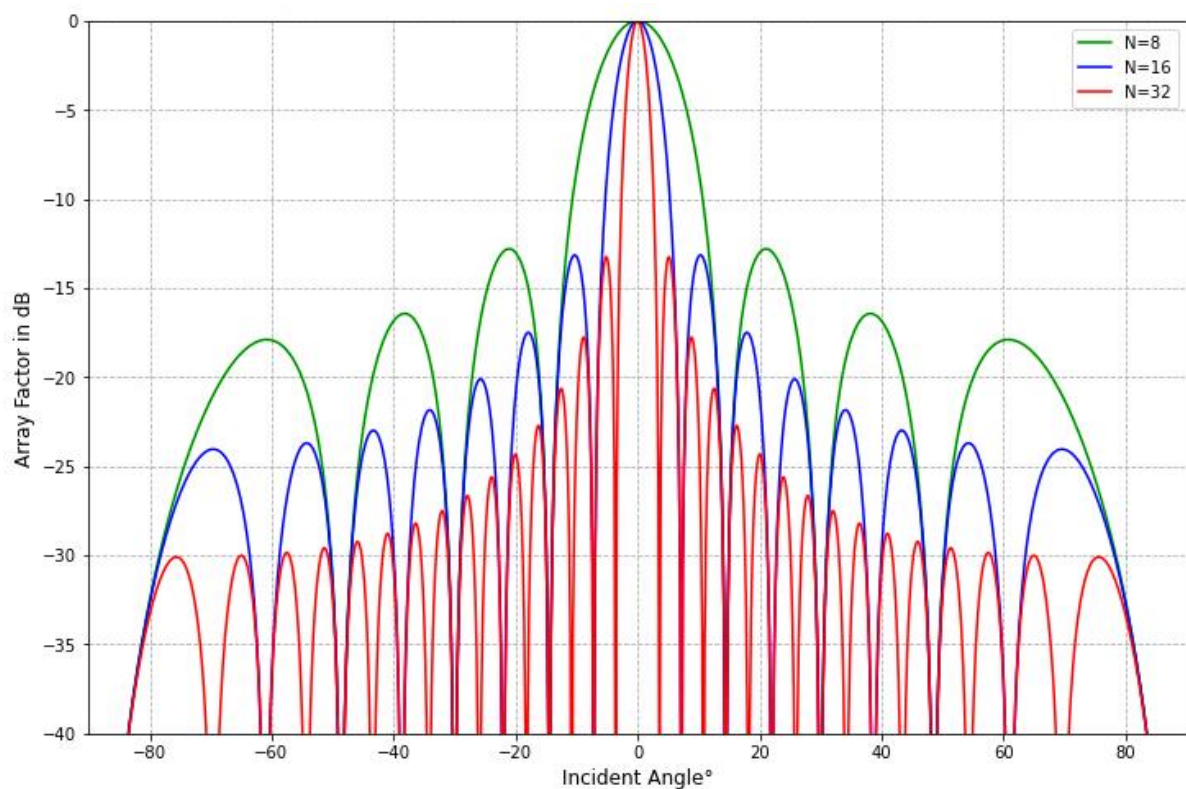


Figure 3.3 Normalized Array factor patterns of uniform array along y axis with different element count

3.2.3 Steering angle

Equations 2.59, 2.76 and 2.78 state that the main beam of the antenna pattern can be steered to an angle θ_0 by the insertion of the proper phase/time scanning at each element of the array. As already discussed, the inter-element spacing of half-wavelength is the common way to avoid grating lobes. However, it can also be slightly lower/higher than $\lambda/2$ with respect to the beam steering angle. The mathematical relation is given by the following equation [8,50]:

$$\frac{d}{\lambda} < \frac{1}{1 + \sin |\theta_0|} \quad (3.1)$$

Let's assume that beam steering angle is equal to $\theta_0=35^\circ$. According to equation 3.1, the inter-element spacing is allowed to be smaller than 0.63λ . Figure 3.4 is the proof of the condition where the grating lobe occurs. It also provides inter-element spacing can be 0.55λ when the beam is steered to 35° to have narrower bandwidth, thereby more directive array without grating lobes. In addition to this, mutual coupling effect can be degraded due to the increase of the inter-element spacing.

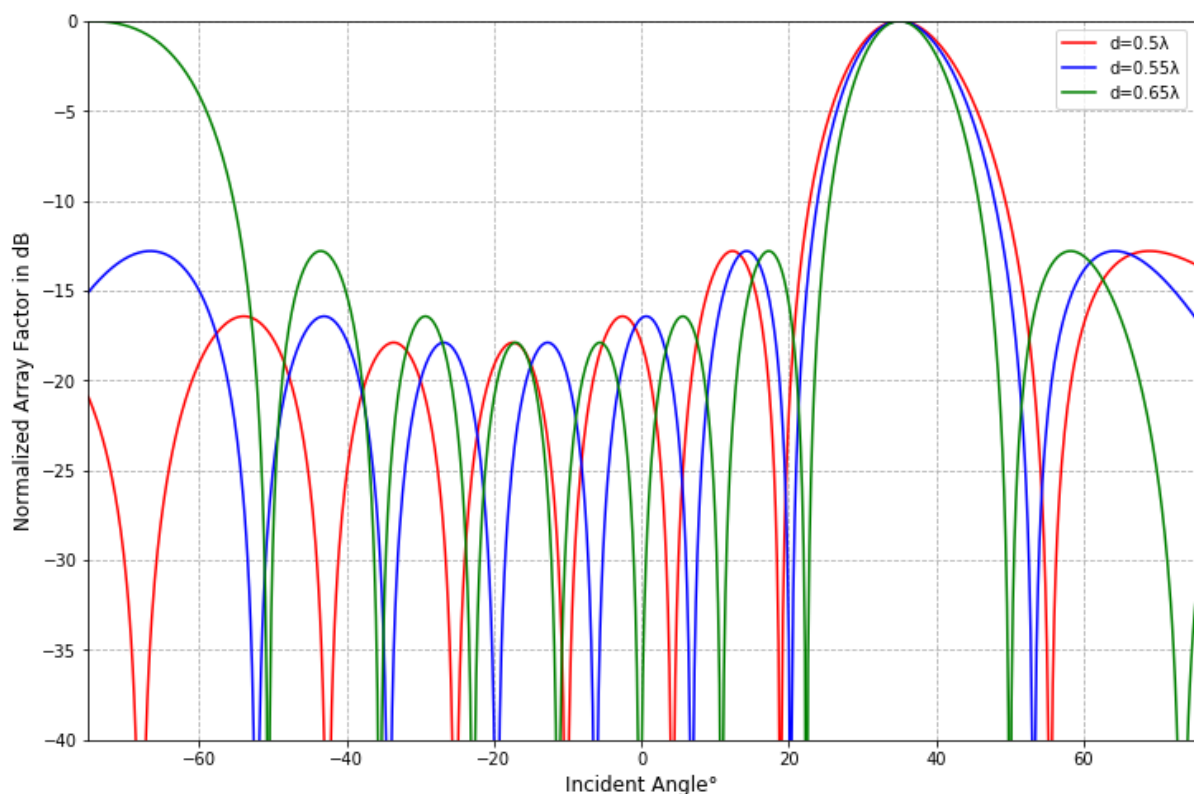


Figure 3.4 Normalized Array factor patterns of uniform array along y axis with different inter-element spacing at $\theta_0=35^\circ$.

Furthermore, Figure 3.5 shows how the array radiation pattern behaves when the different steering angles is implemented for the uniformly spaced linear array with 0.5λ spacing consisting of 32 elements. Accordingly, it can be concluded that the higher beam steering angle causes the wider beamwidth.

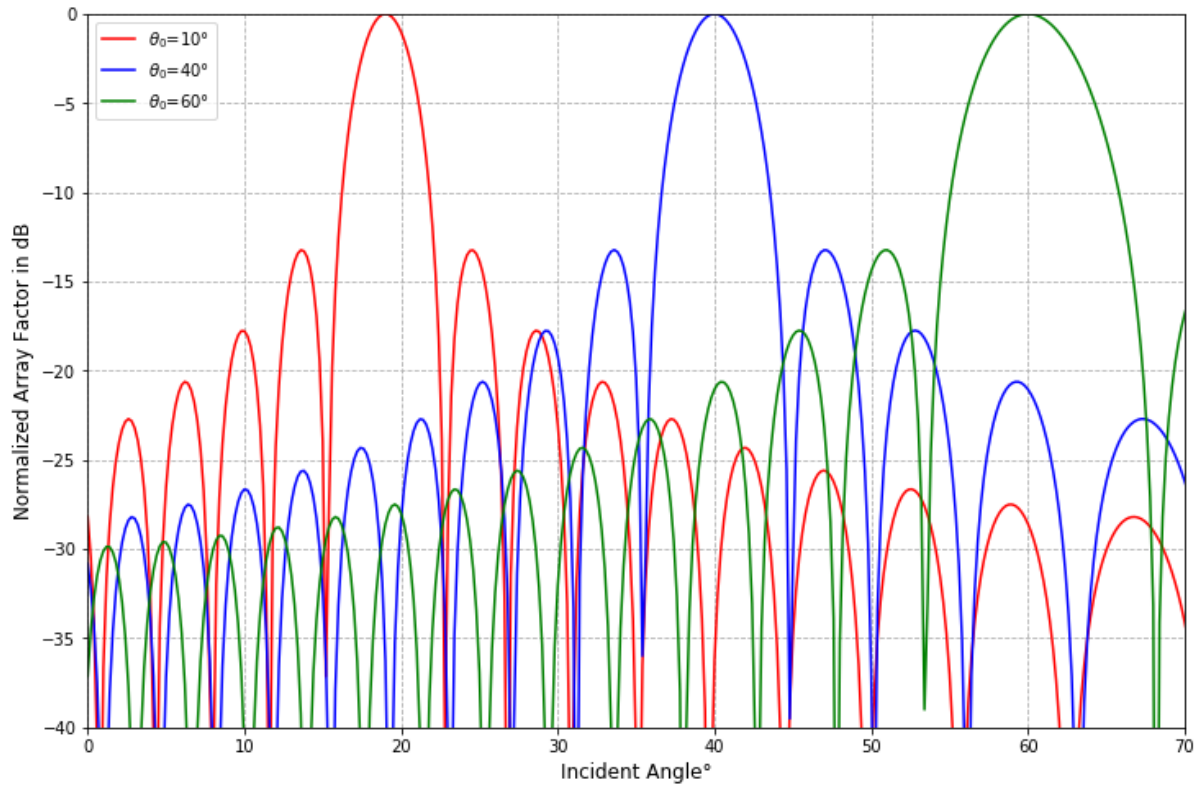
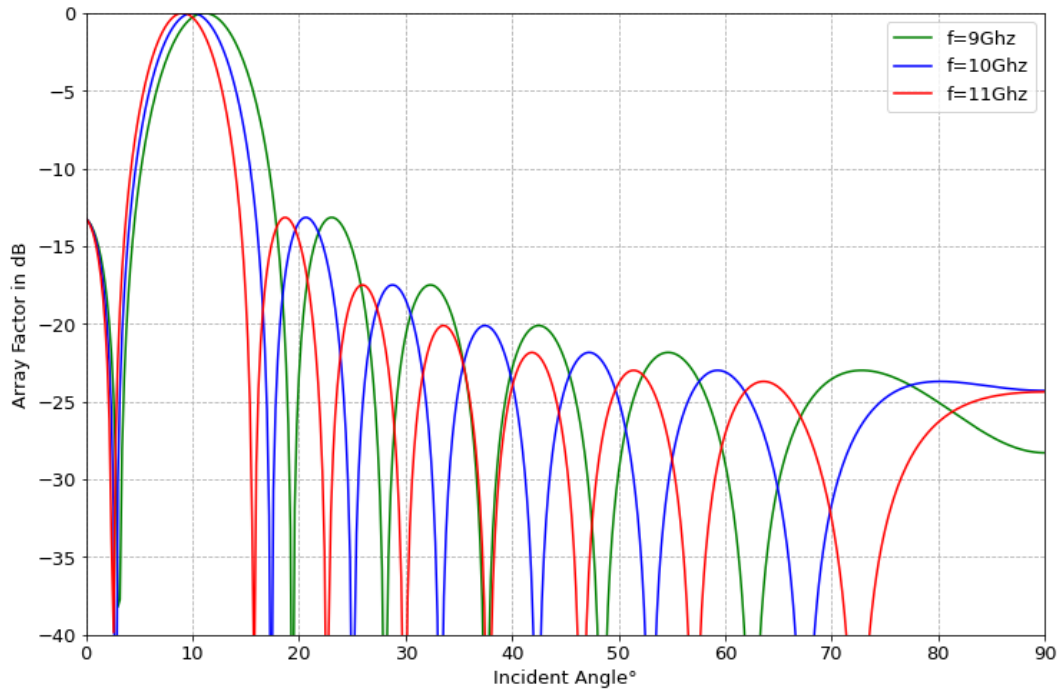


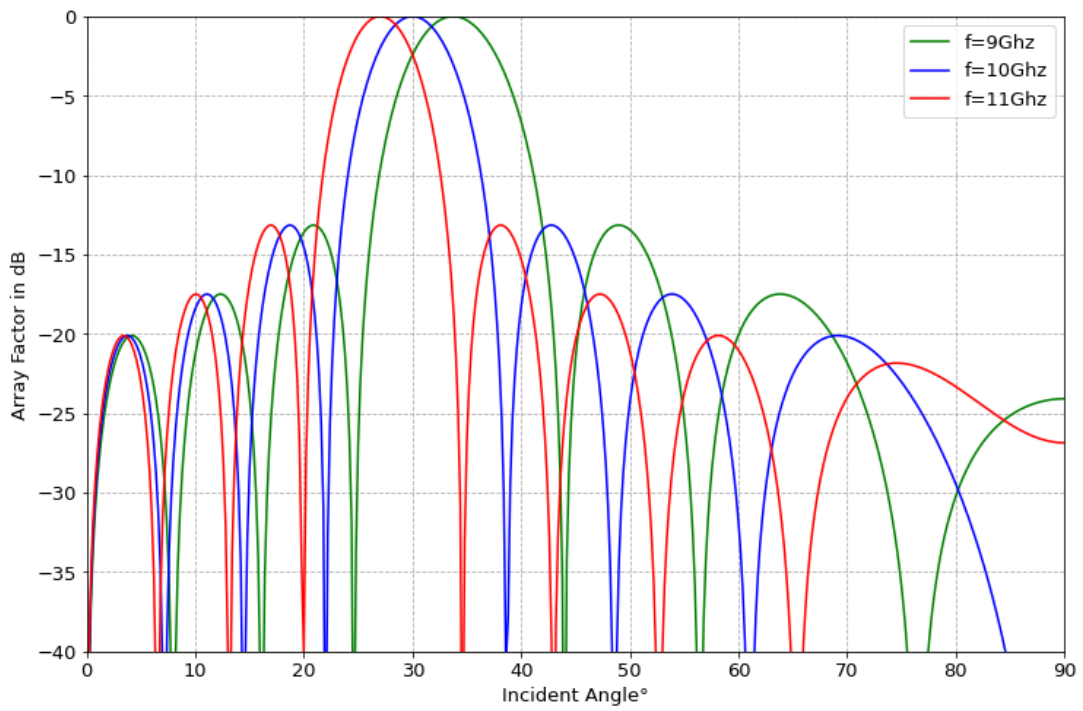
Figure 3.5 Normalized Array factor patterns of uniform array along y axis with different beam steering angles

3.2.4 Comparison of Phase Shifter and TTD

This section aims to give the comparison of array factor patterns in case of the implementation of TTD and phase shifting methods. As earlier discussed in Chapter 2.5.3.1, beam squint effect is visible in Figure 3.6 when the phase shifting method is implemented with three different frequencies as 9 GHz, 10 GHz and 11 GHz. Besides, this figure also shows the variation of beamwidth with different beam steering angles as 10° , 30° , 50° respectively. Accordingly, the greater beam steering angle leads to results in wider beam width.



a) $\theta_0=10^\circ$



b) $\theta_0=30^\circ$

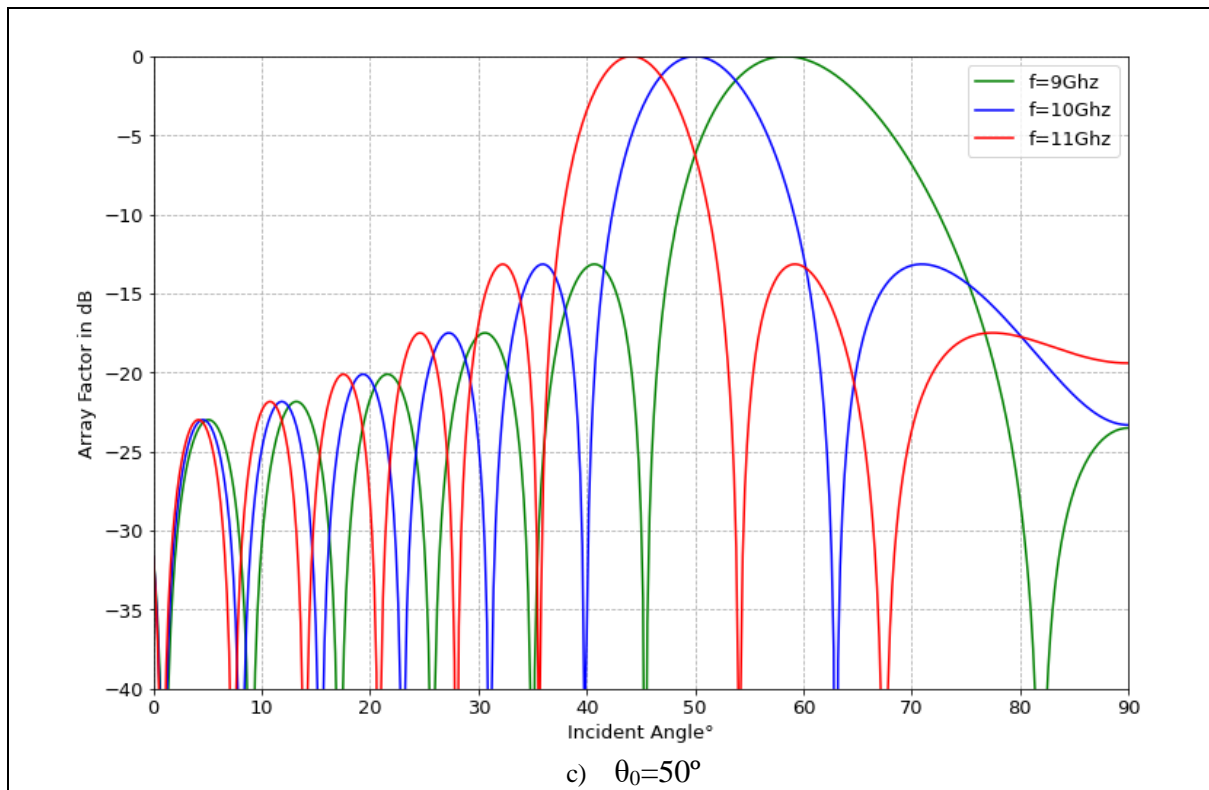
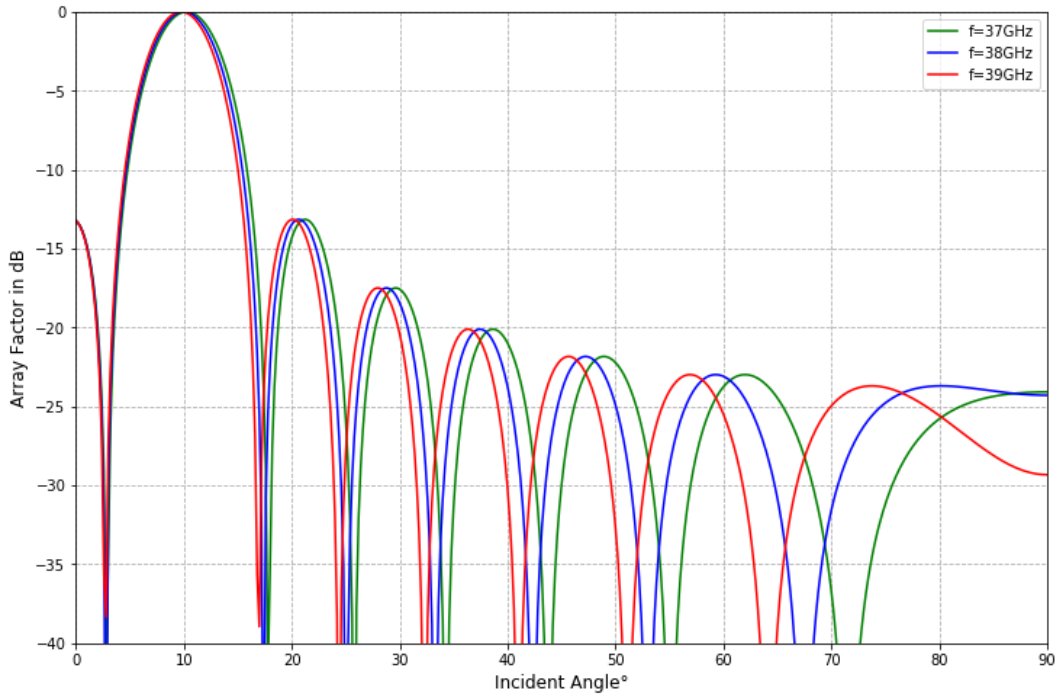
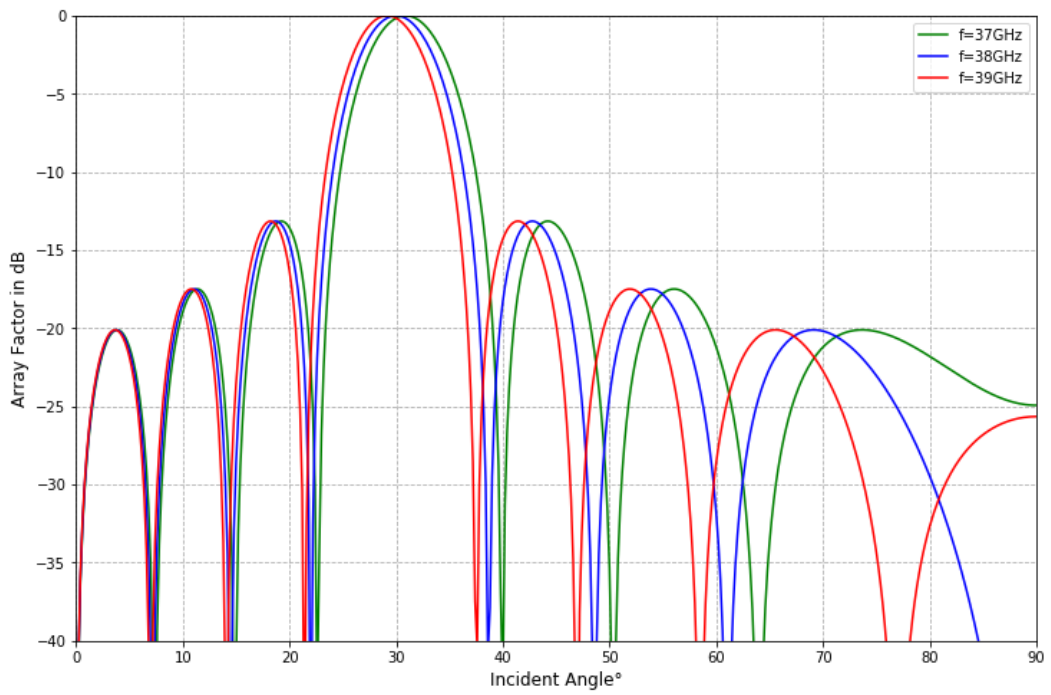


Figure 3.6 Normalized Array factor patterns of uniformly spaced 16 elements linear array along y axis with different beam steering angles when the phase shifting is implemented

In addition to X-band, Figure 3.7 also presents the results of Ka-band frequencies with implementation of Phase shifter. As already mentioned, the developed simulator can work at any frequency. According to graphical results, when the frequency is increased, the behaviour of the array completely changes because the phase shifter does not suitable for wide band frequencies.



a) $\theta_0=10^\circ$



b) $\theta_0=30^\circ$

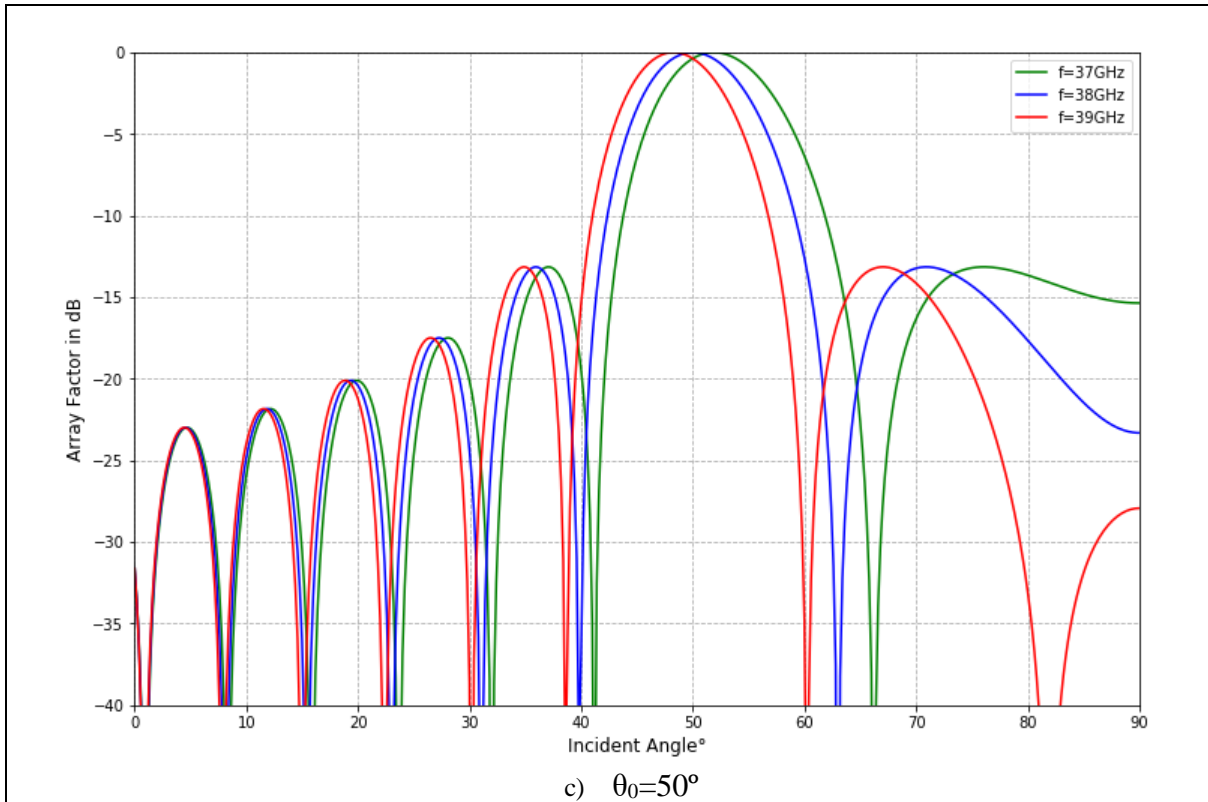
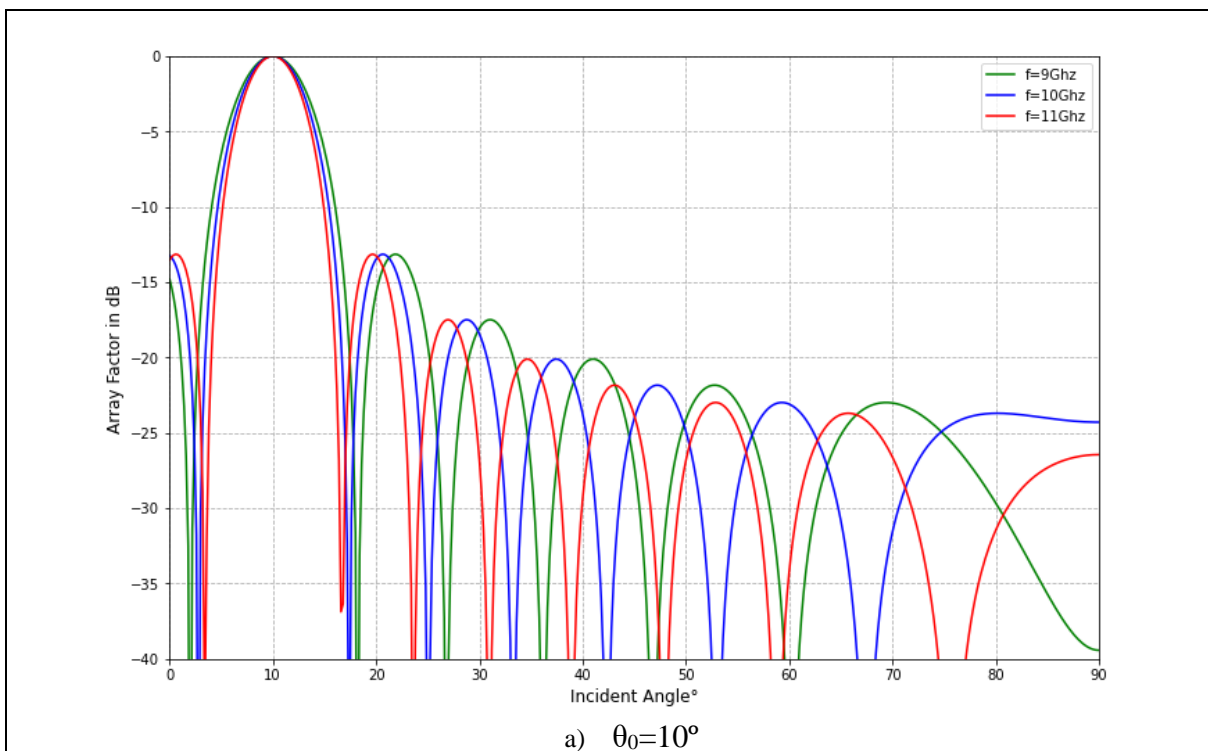


Figure 3.7 Normalized Array factor patterns of uniformly spaced 16 elements linear array along y axis with different beam steering angles with the phase-shifter implementation in Ka-band

On the other hand, the plot of the array factor patterns with the TTD implementation for the same three frequencies are given by Figure 3.8 which clearly shows the benefits of TTD beam steering to avoid beam squint.



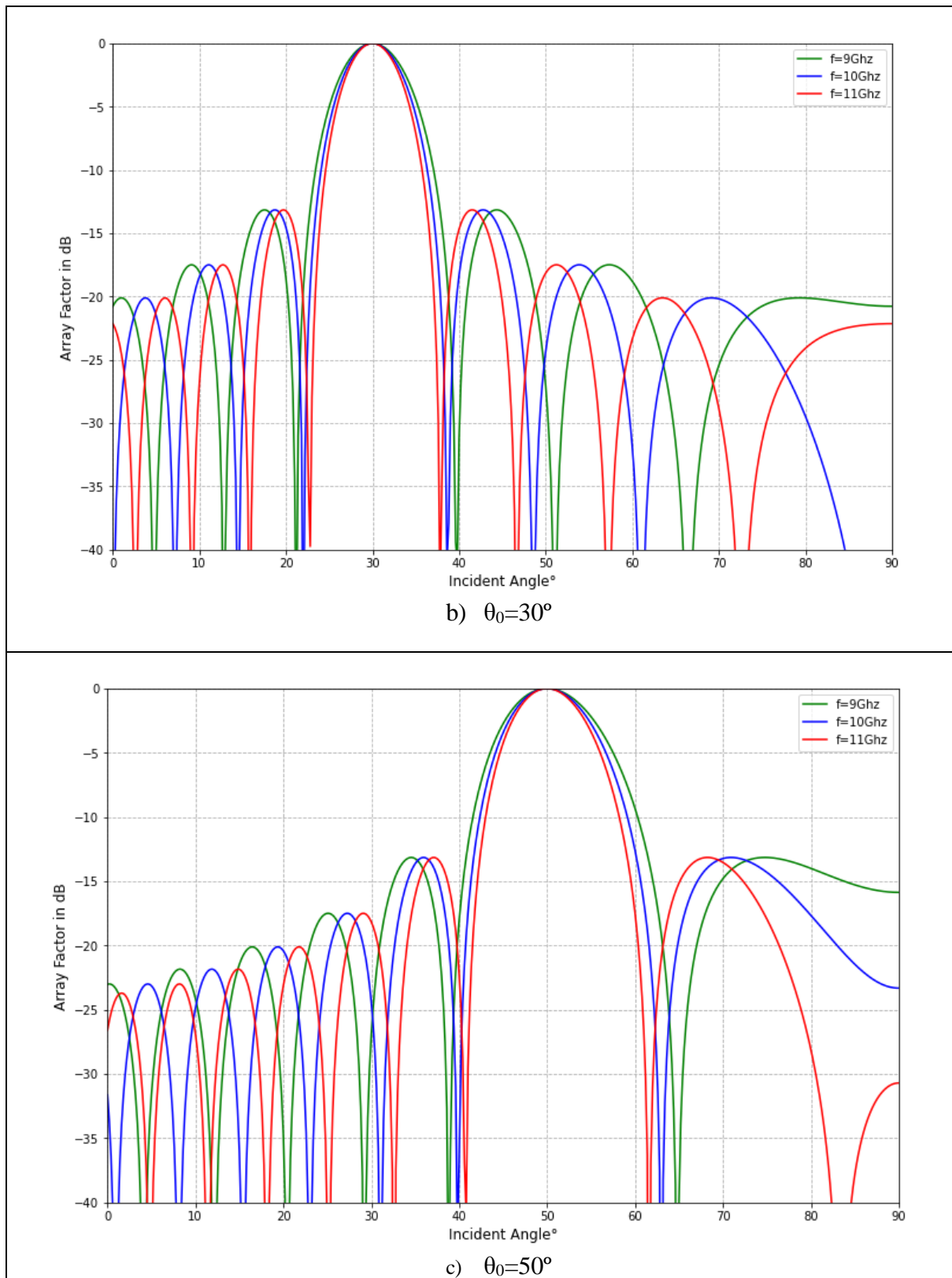
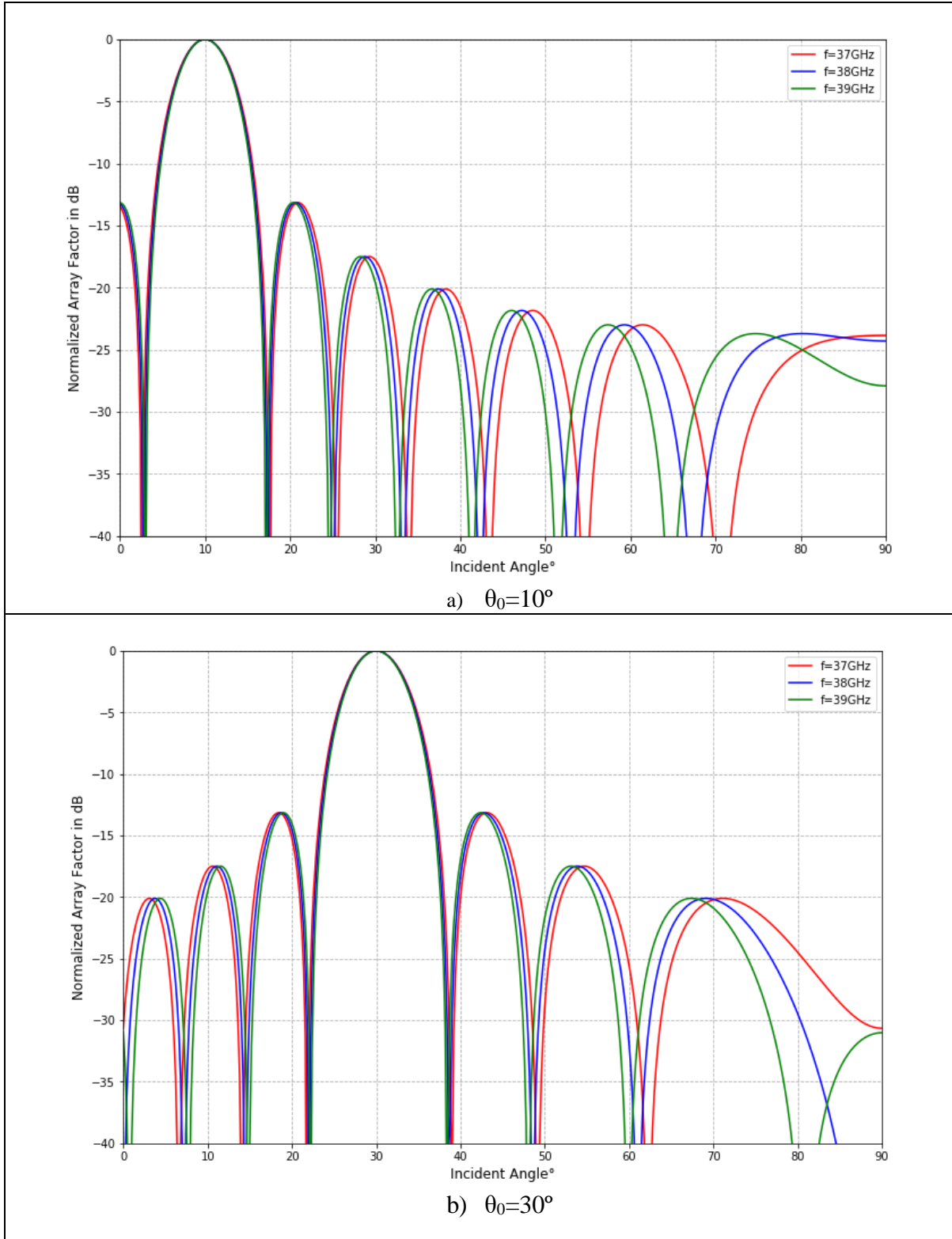


Figure 3.8 Normalized Array factor patterns of uniformly spaced 16 elements linear array along y axis with different beam steering angles when the TTD is implemented

Figure 3.9 presents the results of Ka-band frequencies with implementation of TTD. According to graphical results, TTD is more suitable than the phase shifter especially in the wide-band frequencies.



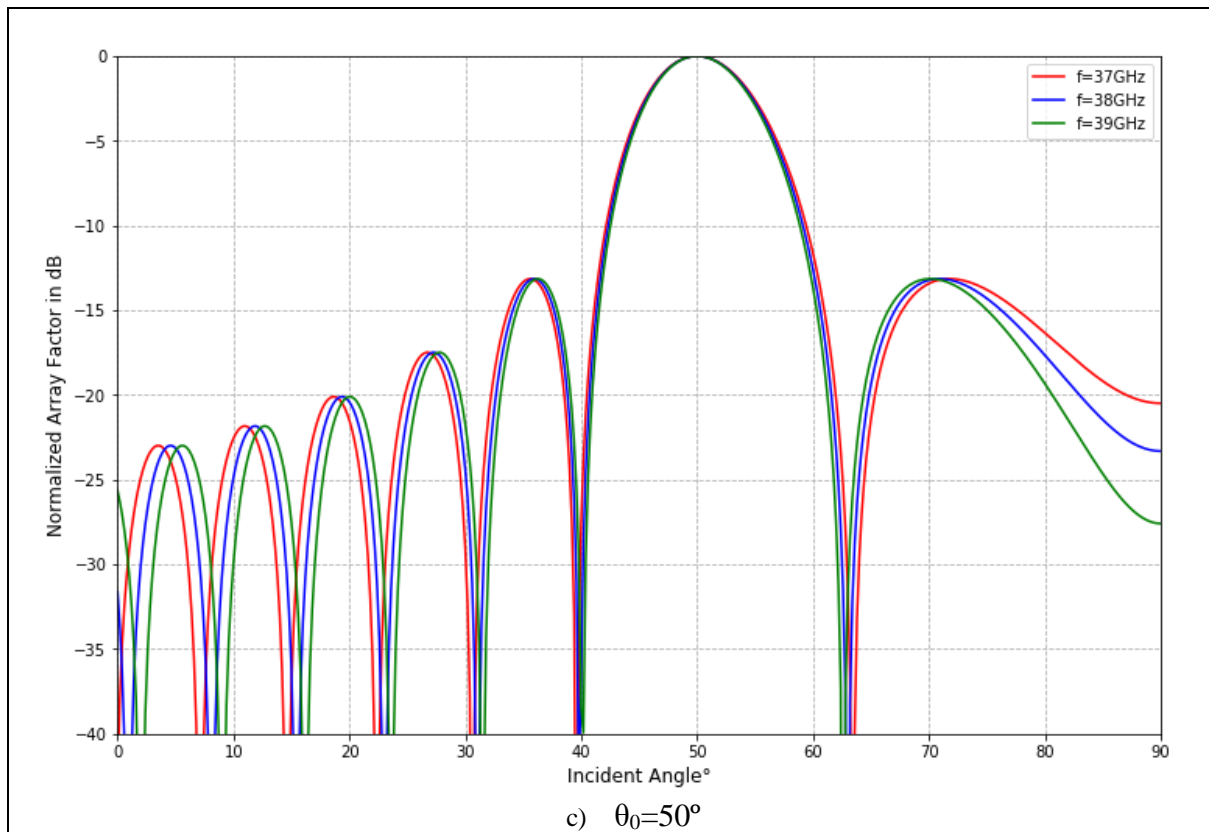


Figure 3.9 Normalized Array factor patterns of uniformly spaced 16 elements linear array along y axis with different beam steering angles when the TTD is implemented in Ka-band

3.3 Proposed Antenna Arrays

In this thesis project, uniformly and non-uniformly spaced linear and planar arrays were designed and simulated with uniform amplitude current excitation. This section aims to give an overview of the simulation results obtained via Python Simulator for each proposed array.

3.3.1 Uniformly Spaced Arrays

Graphical representation of normalized array factor patterns of broadside linear arrays consisting of 2, 4 and 8 elements for inter-element spacing of 0.5λ are given by Figure 3.10. The result reveals that the main lobe beamwidth decreases and the number of side lobes increases with the higher number of elements.

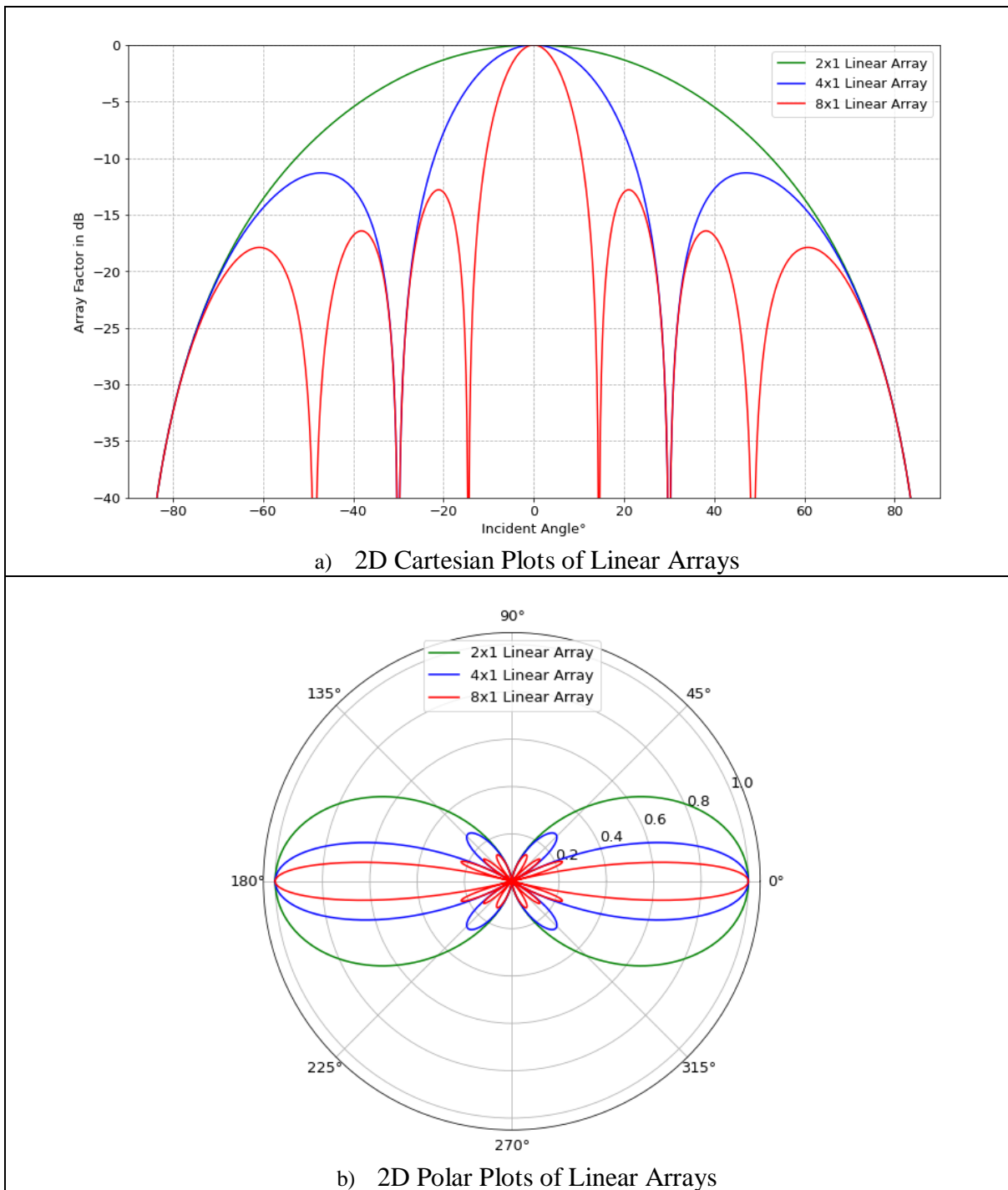


Figure 3.10 Normalized Array factor patterns of uniformly spaced broadside linear arrays along x- axis

Figure 3.11 gives the normalized array factor patterns for planar arrays consisting of 4, 8 and 16 elements. The same behavior as observed via linear arrays appears when the number of elements increases in planar configurations as well.

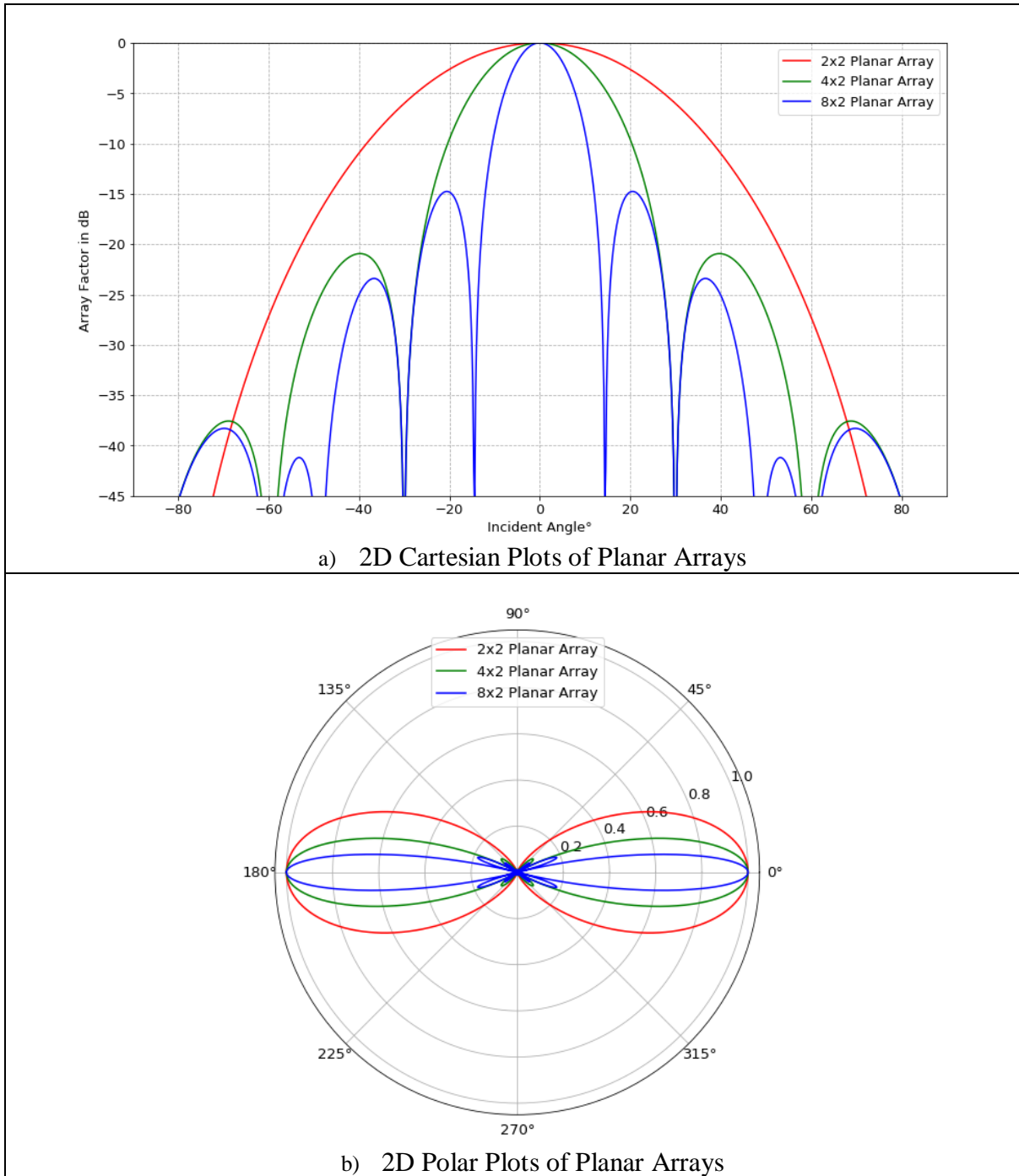


Figure 3.11 Normalized Array factor patterns of uniformly spaced broadside planar arrays along -x and -y axes

In addition to this, the comparison of 8x1 linear and 4x2 planar arrays as well as 4x1 linear and 2x2 planar arrays can also be made here since each has the same elements number. Accordingly, planar arrays provide wider beamwidth with reduced side lobe levels and side lobe numbers which thereby leads to have higher directivity as shown by Figure 3.12.

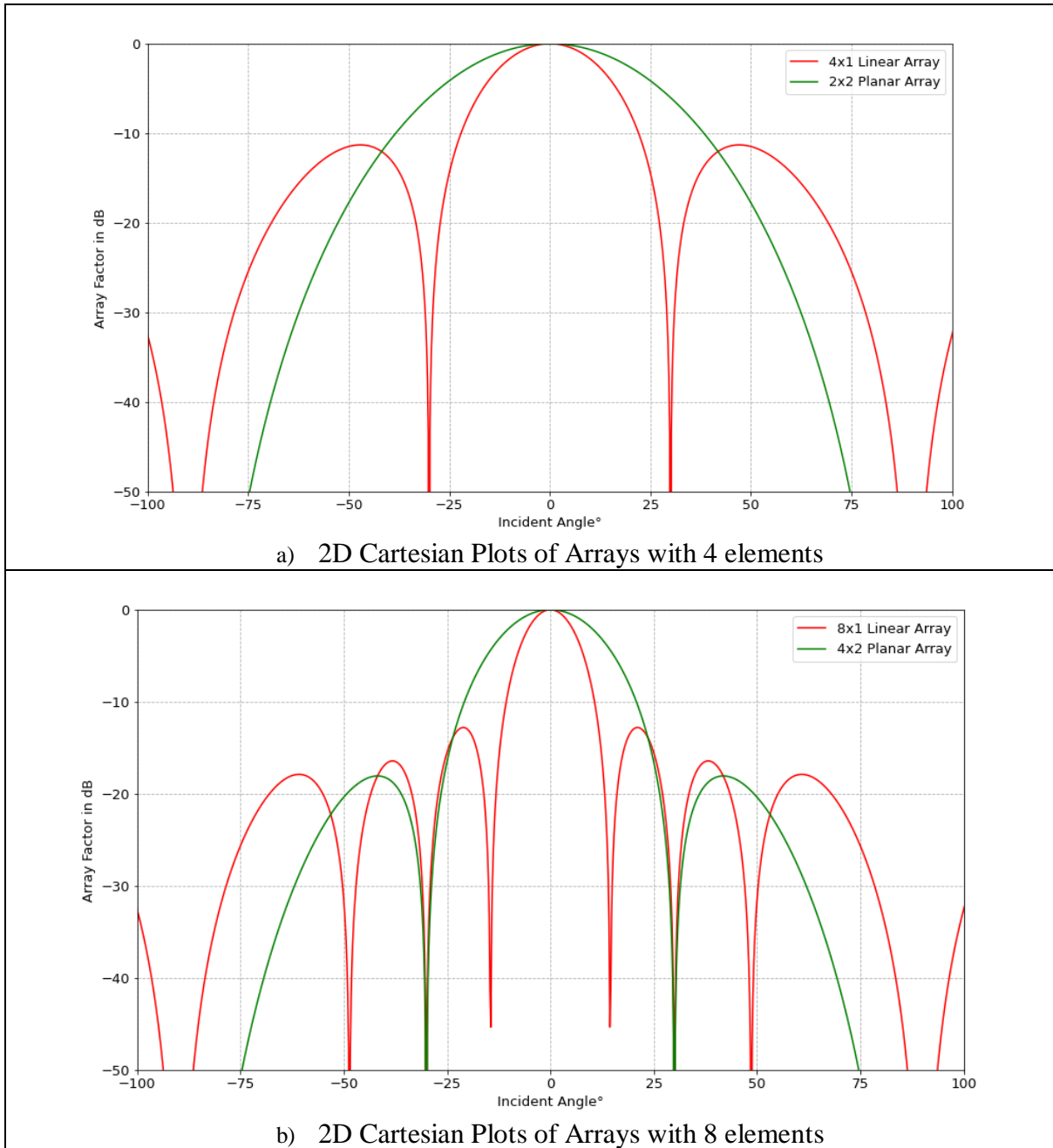


Figure 3.12 Normalized Array factor patterns of uniformly spaced broadside arrays with the same number of elements and different geometrical configuration

3.3.2 Non-Uniformly Spaced Arrays

As a first advantage, non-uniform symmetric arrays can be utilized to get the comparable beamwidth with fewer elements to the uniform array. Accordingly, Figure 3.13 illustrates the comparison of 6 elements non-uniform symmetric array with the increase rate of 0.1λ and 7 elements uniform array where HPBW is equal to 8° in both cases.

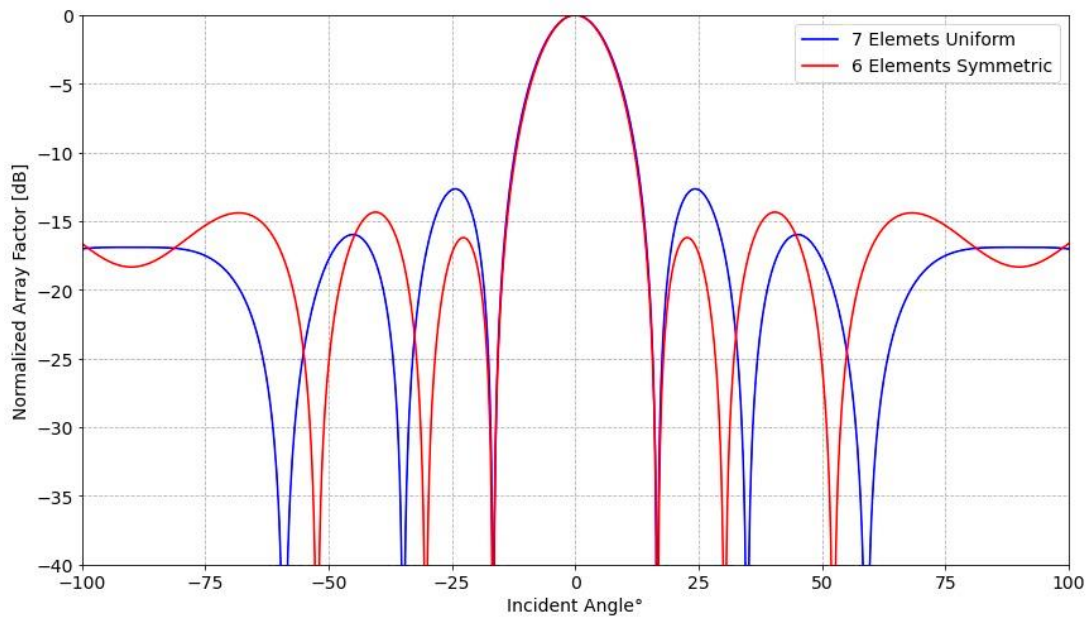
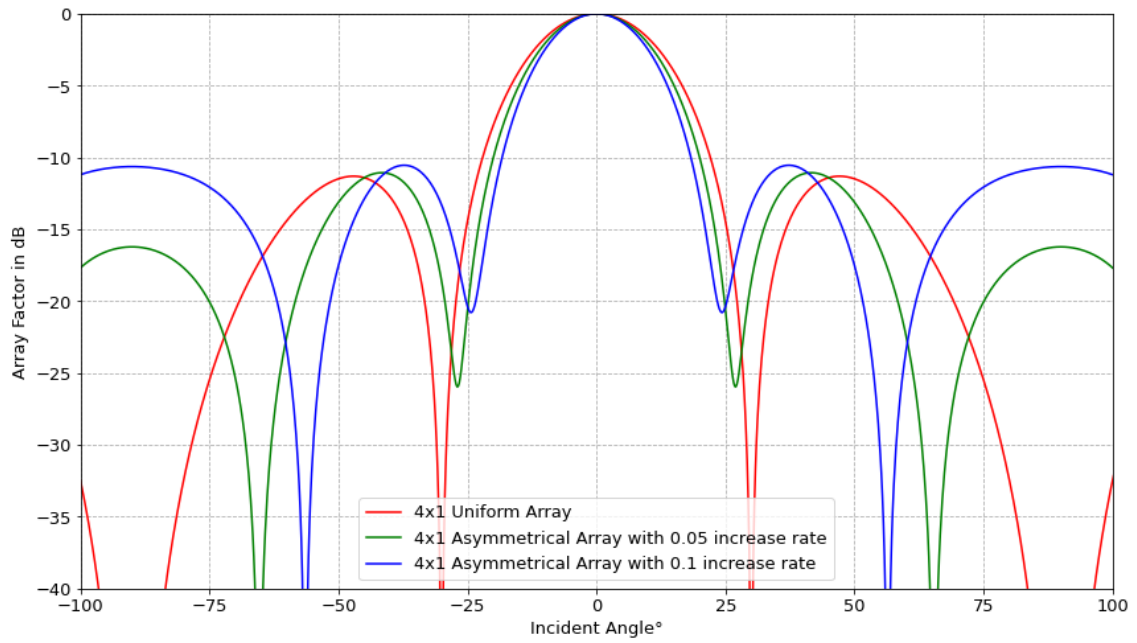
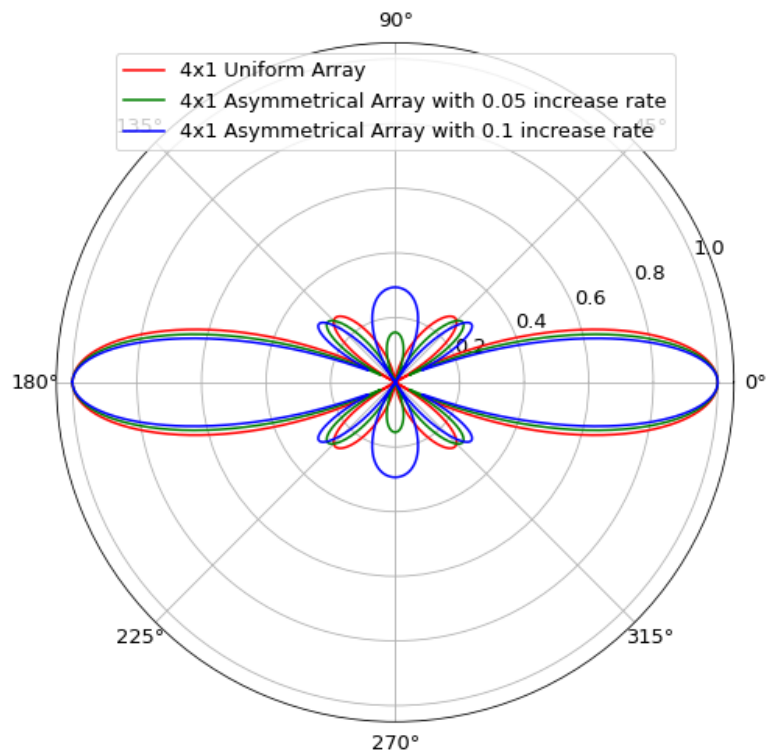


Figure 3.13 Different Array Layouts

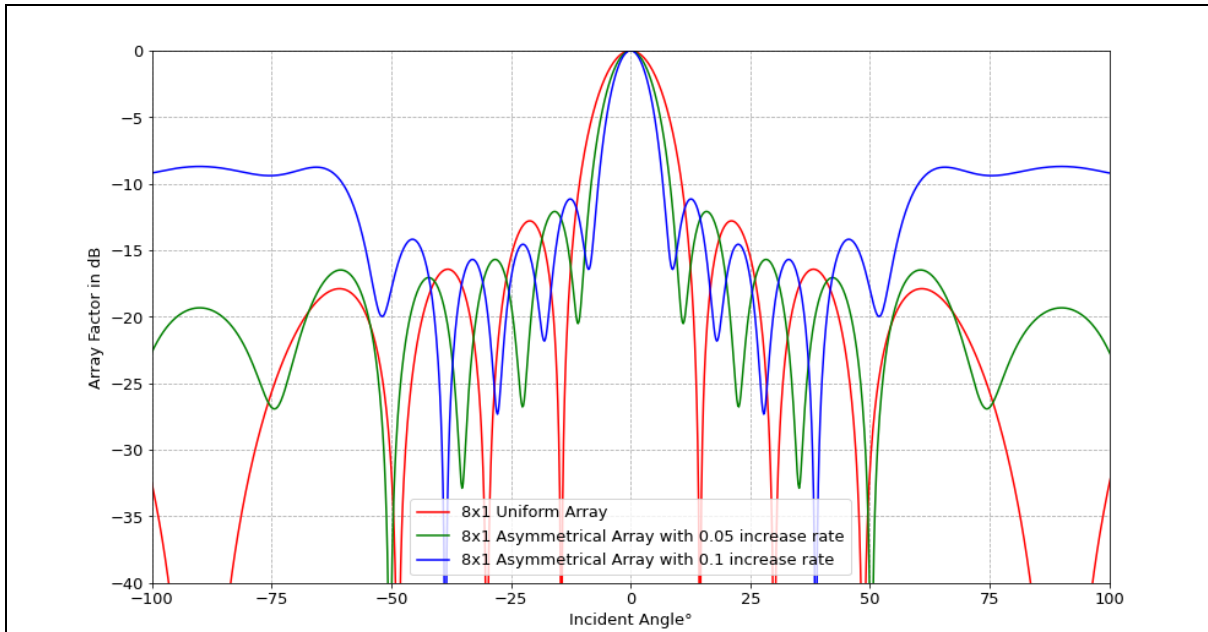
Moreover, to see the potential improvements on array performance with the same element number, two types of non-uniform array configurations are implemented as already explained in the section 2.5.2.2. Accordingly, Figure 3.14 and 3.15 show the array factor patterns of linear and planar arrays respectively in case the asymmetrical configuration is chosen. Neither for linear nor for planar arrays desired enhancement on the array performance could not be obtained with this sort of configuration.



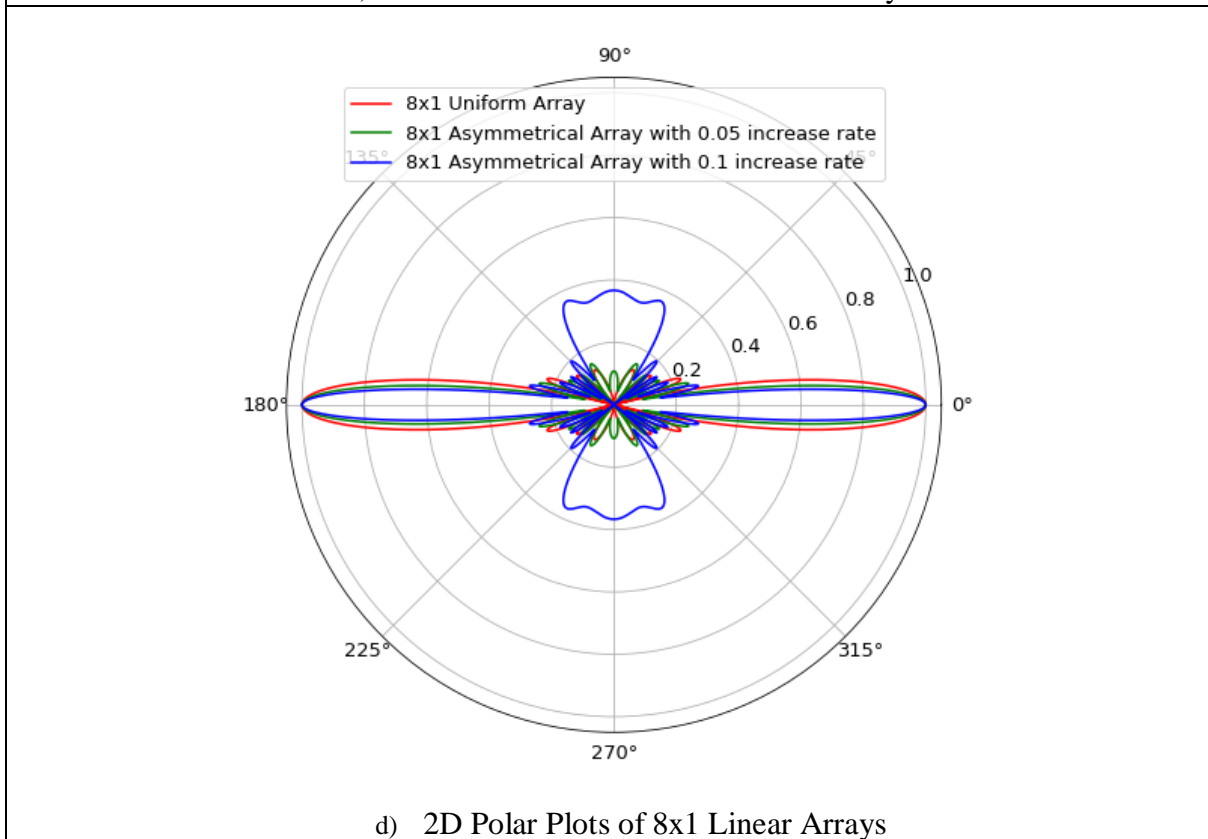
a) 2D Cartesian Plots of 4x1 Linear Arrays



b) 2D Polar Plots of 4x1 Linear Arrays

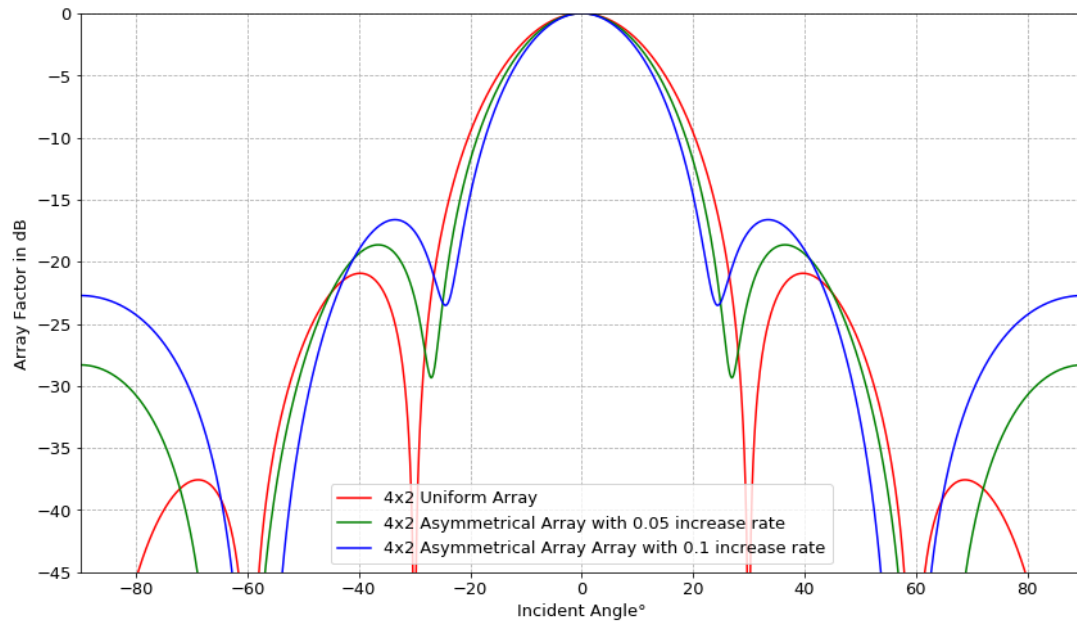


c) 2D Cartesian Plots of 8x1 Linear Arrays

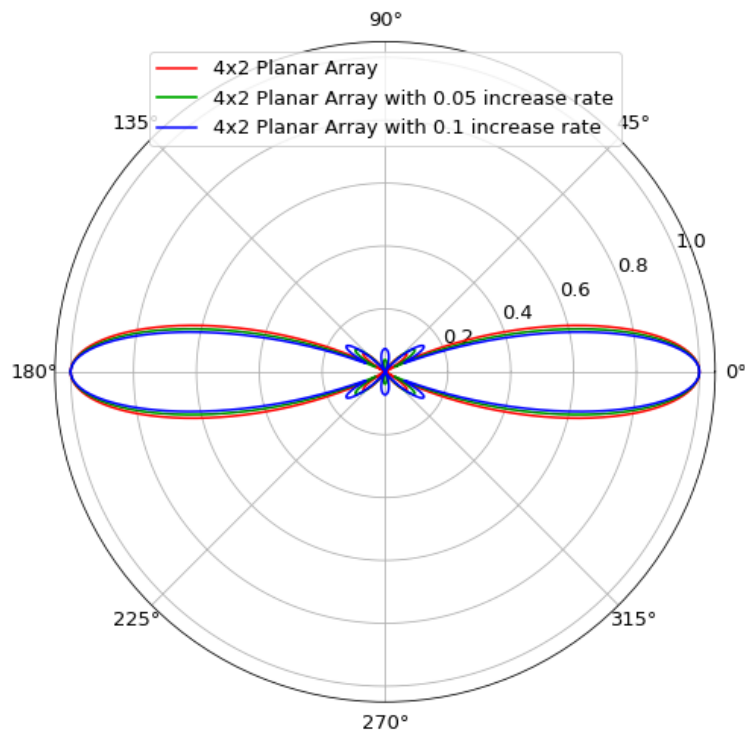


d) 2D Polar Plots of 8x1 Linear Arrays

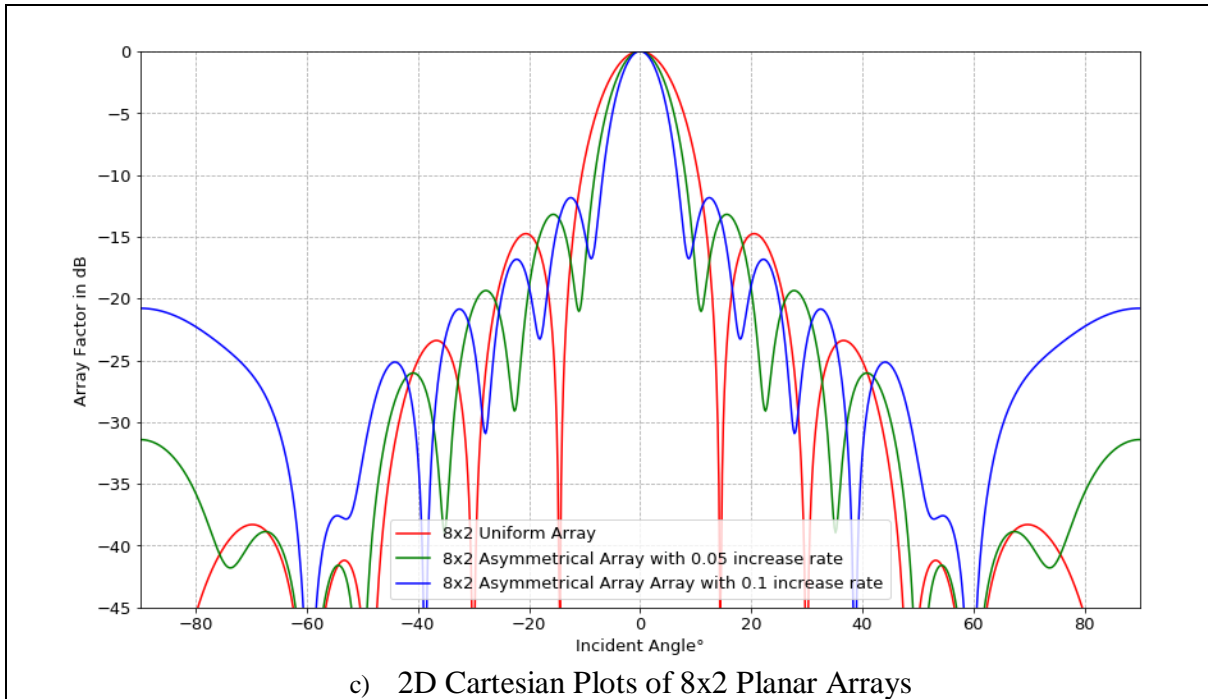
Figure 3.14 Normalized Array factor patterns of Uniform and Asymmetrical Non-Uniform broadside linear arrays along x- axis



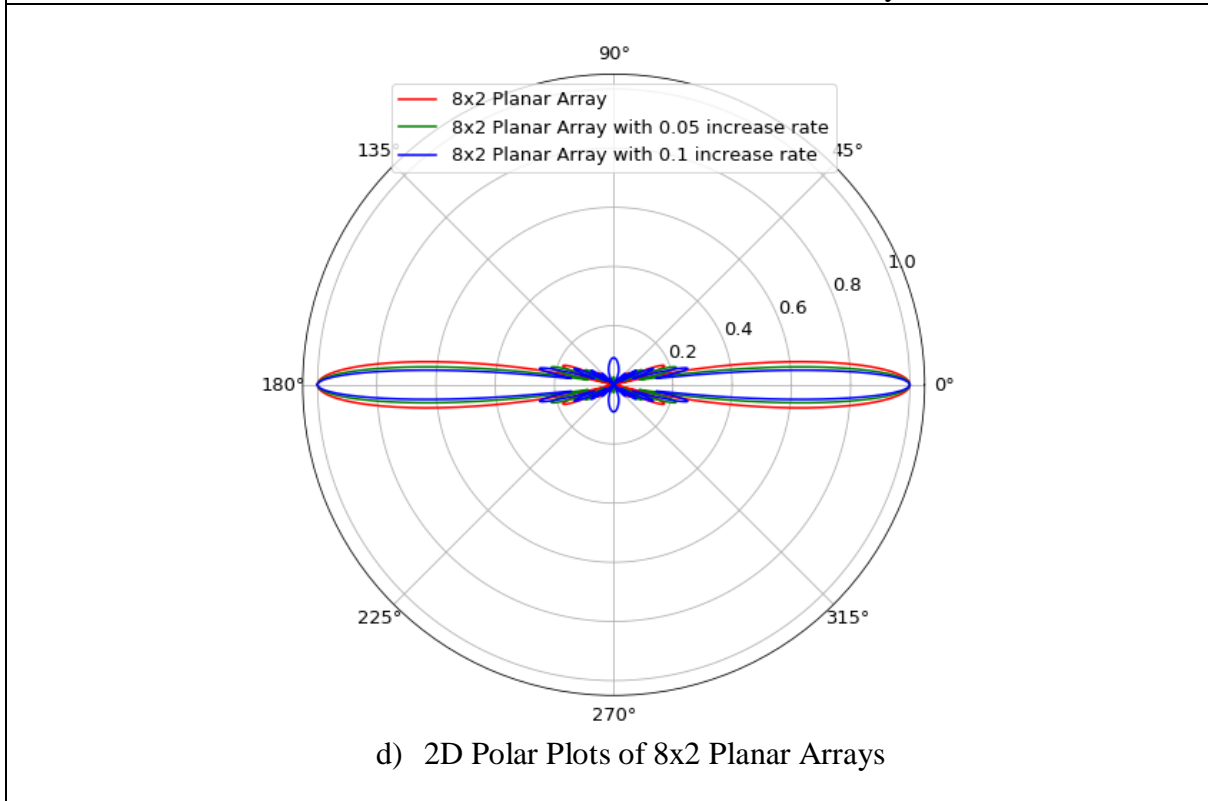
a) 2D Cartesian Plots of 4x2 Planar Arrays



b) 2D Polar Plots of 4x2 Planar Arrays



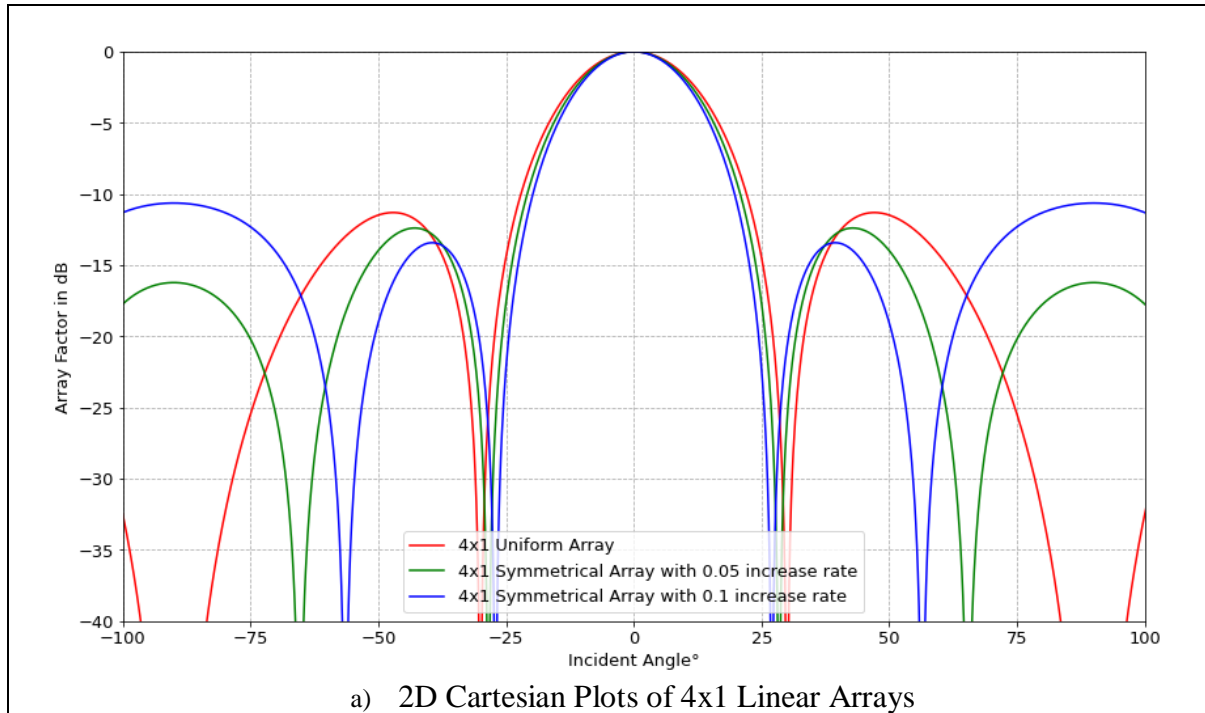
c) 2D Cartesian Plots of 8x2 Planar Arrays



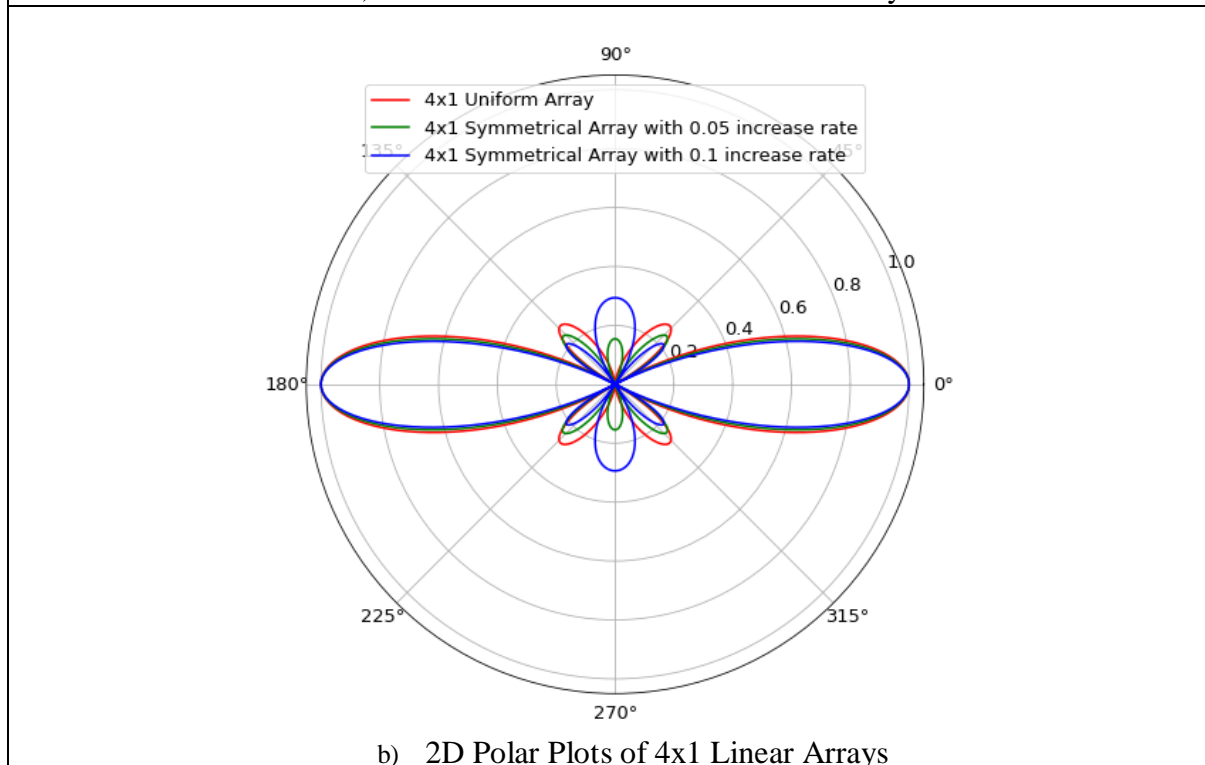
d) 2D Polar Plots of 8x2 Planar Arrays

Figure 3.15 Normalized Array factor patterns of Uniform and Symmetrical Non-Uniform broadside planar arrays along x- and y- axes

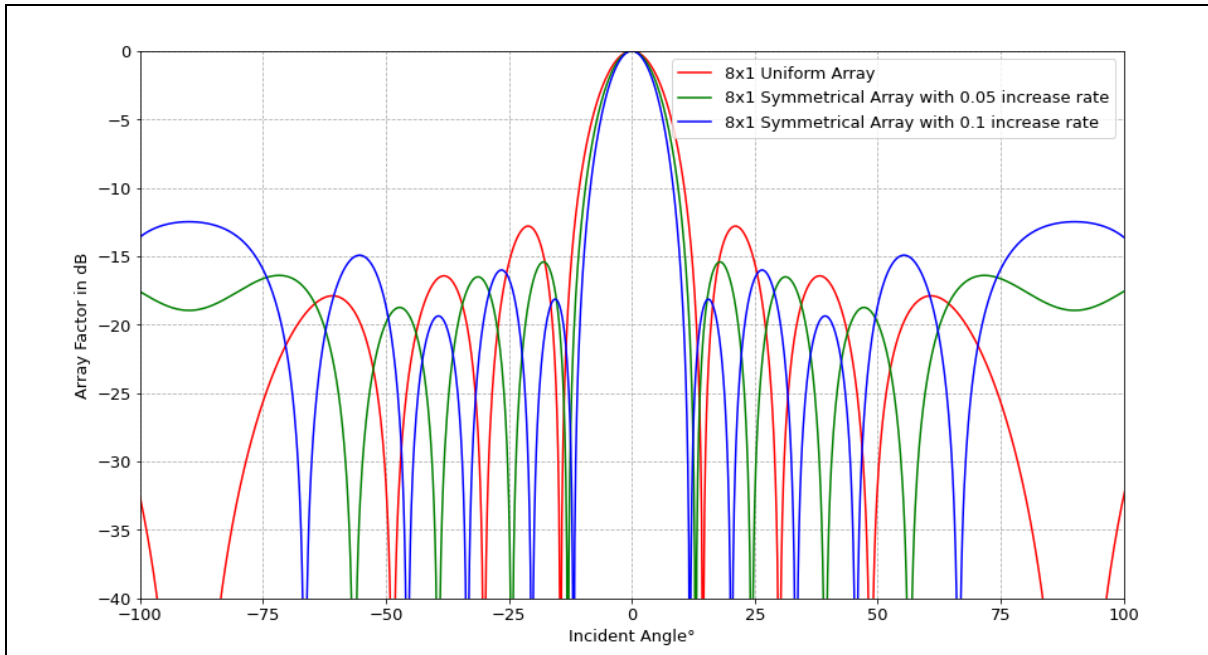
On the other hand, Figure 3.16 and Figure 3.17 present noticeable enhancements in sidelobe level reduction by non-uniform symmetrical arrangement with 0.1λ and 0.05λ as increase rate which also provides shorter array length than asymmetrical configurations. In addition, the gain slightly increases in comparison to the uniformly arrangement arrays.



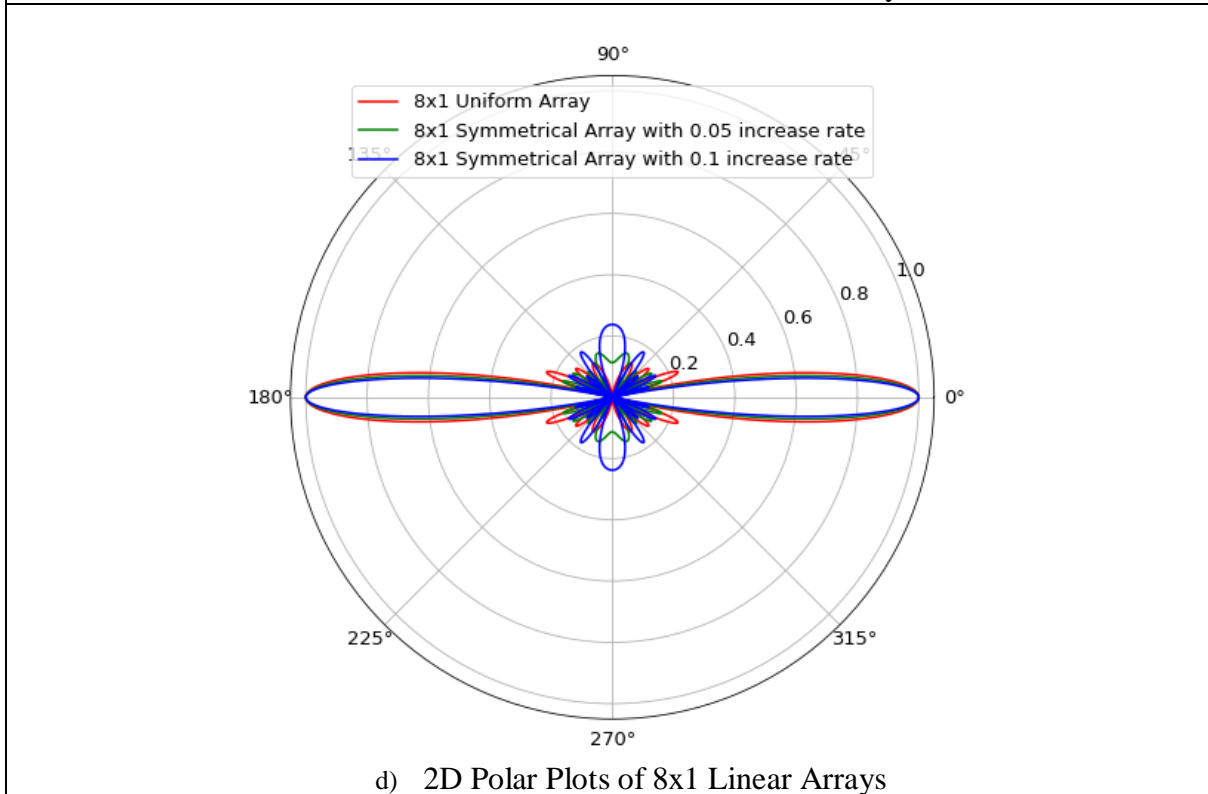
a) 2D Cartesian Plots of 4x1 Linear Arrays



b) 2D Polar Plots of 4x1 Linear Arrays

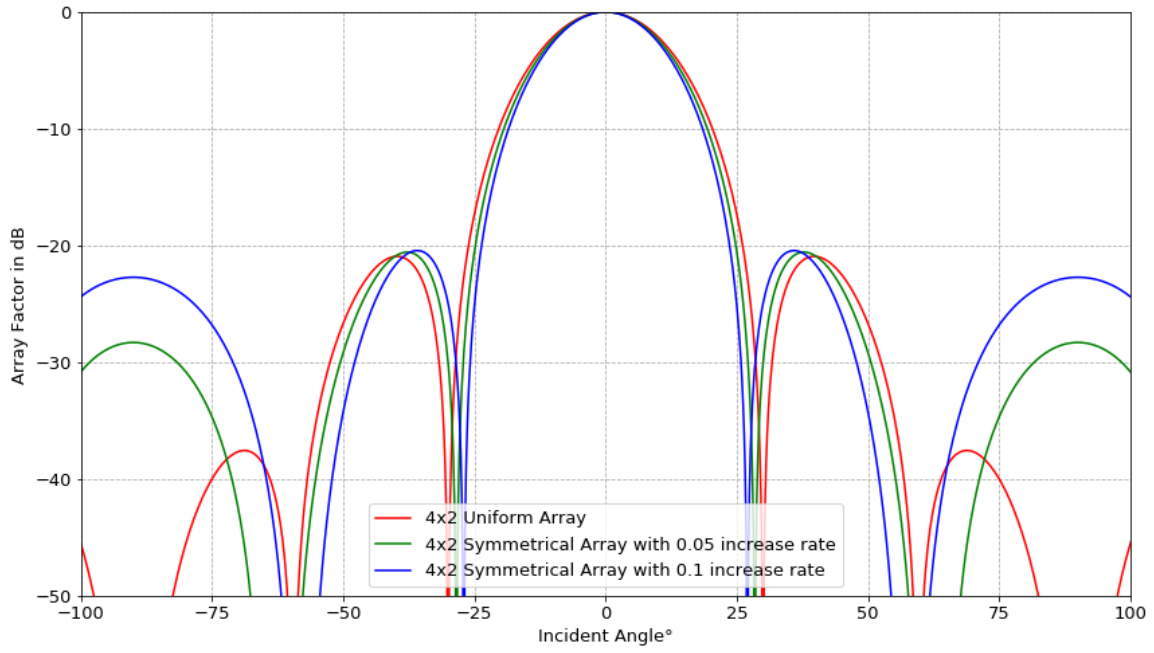


c) 2D Cartesian Plots of 8x1 Linear Arrays

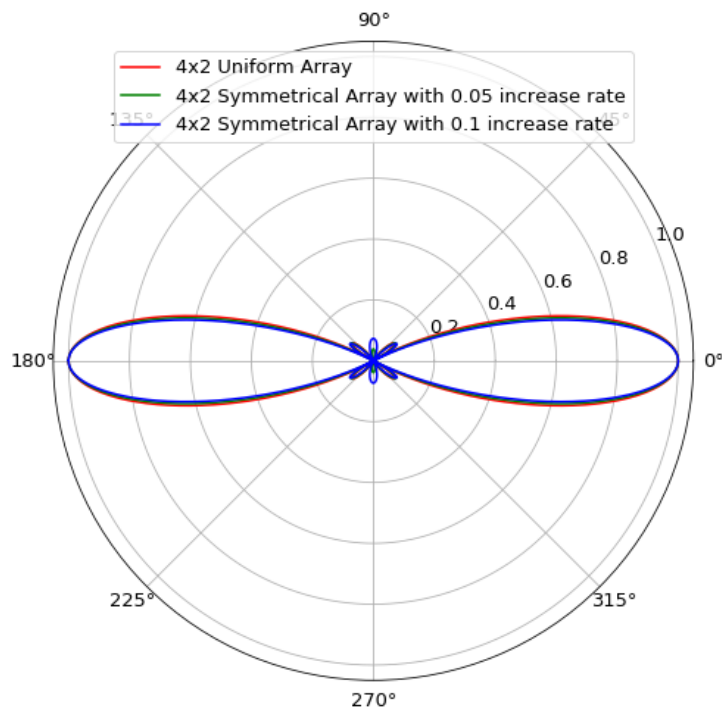


d) 2D Polar Plots of 8x1 Linear Arrays

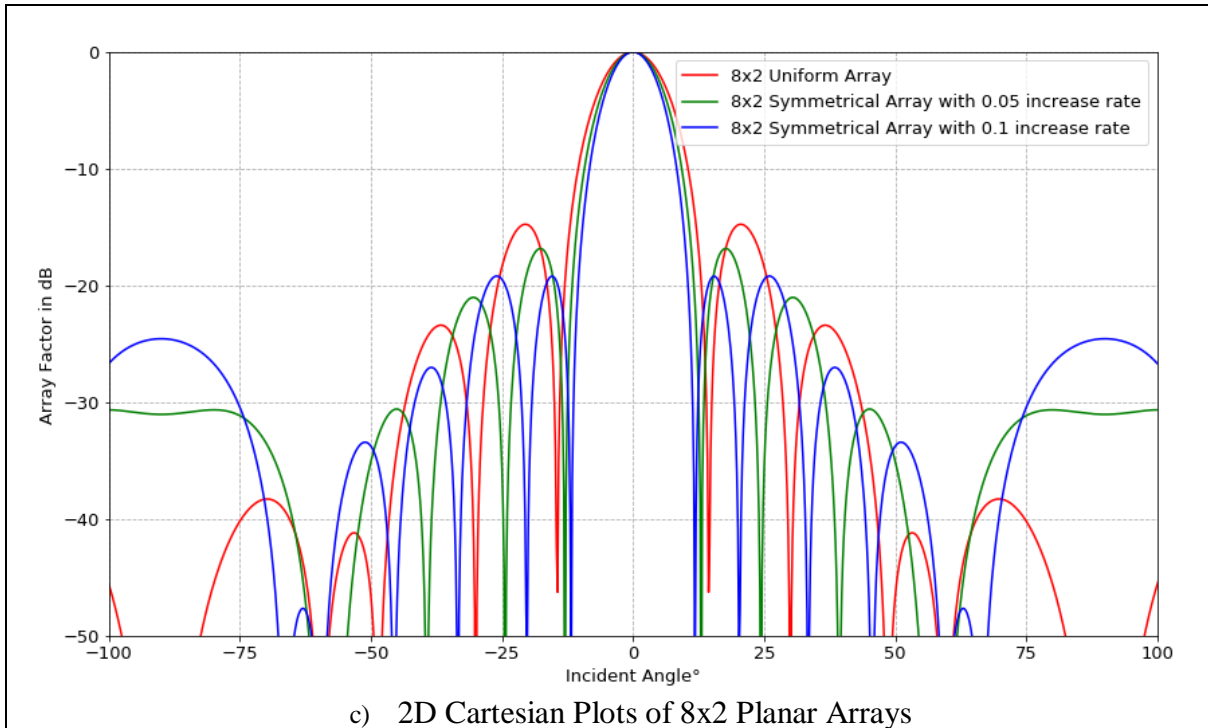
Figure 3.16 Normalized Array factor patterns of Uniform and Symmetrical Non-Uniform broadside linear arrays along x- axis



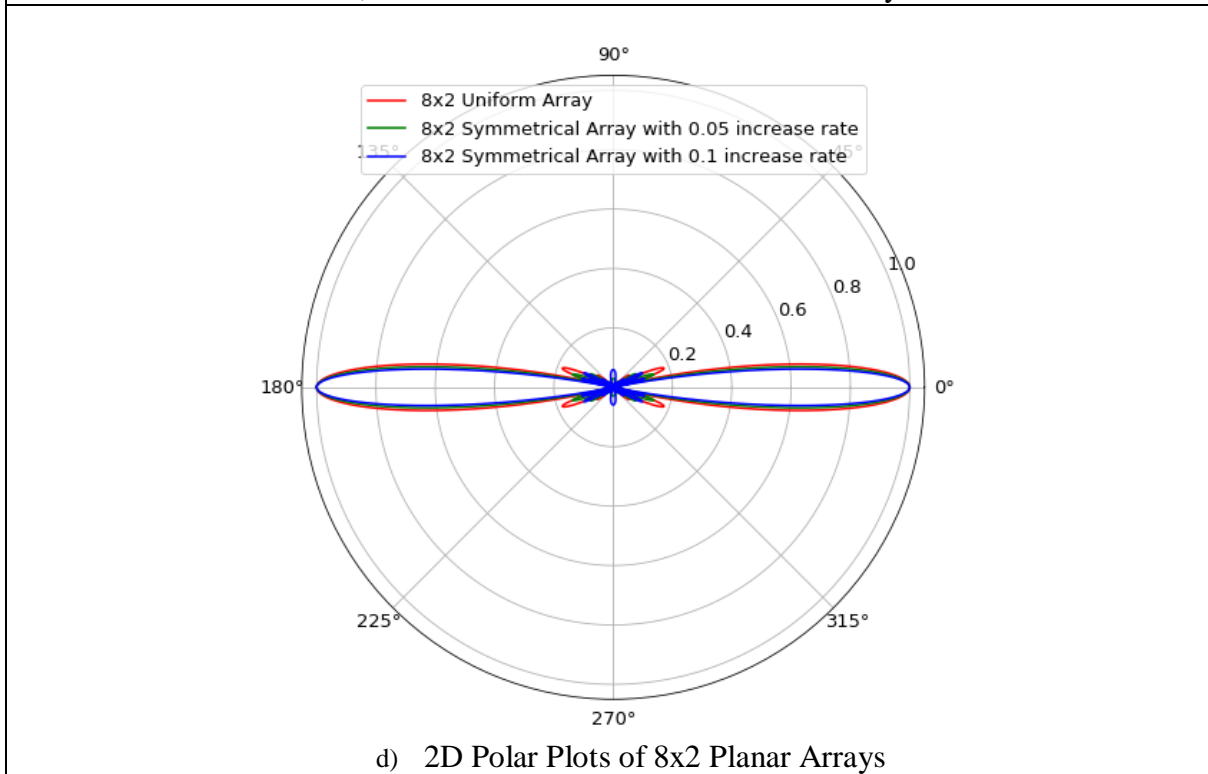
a) 2D Cartesian Plots of 4x2 Planar Arrays



b) 2D Polar Plots of 4x2 Planar Arrays



c) 2D Cartesian Plots of 8x2 Planar Arrays



d) 2D Polar Plots of 8x2 Planar Arrays

Figure 3.17 Normalized Array factor patterns of Uniform and Symmetrical Non-Uniform broadside planar arrays along x- and y-axes

3.4 3D Simulations by HFSS

There are many programs available to assist the antenna design and modeling. ANSYS High-Frequency Structural Simulator (HFSS) is one such software program that utilizes three-dimensional (3-D) modeling defined by the finite elements method (FEM). The FEM utilizes a more powerful and versatile numerical technique for handling problems involving complex geometries and inhomogeneous mediums [48]. This essential tool of HFSS was used for designing and simulating the antennas in this thesis work. Figure 3.18 shows the typical layout of this tool.

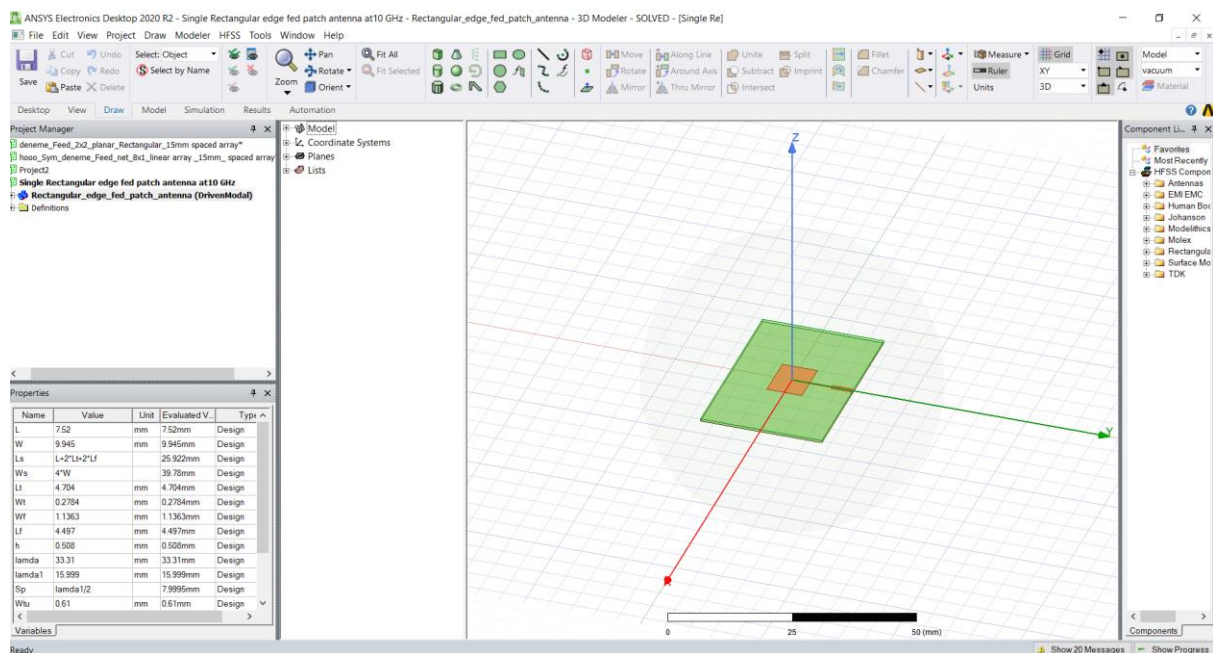


Figure 3. 18 Layout of HFSS

There are four main steps to create and solve a proper HFSS simulation:

1. Creation of the Model
2. Assigning the Boundaries
3. Assigning the Excitation
4. Solving and Simulating the Results

3.4.1 Proposal of Single Rectangular Patch antenna at 10 GHz

The microstrip patch antennas are promising antennas which have been developed with extensive application prospects over 35 years [19]. The efficient design of the single printed patch antenna is initially required to achieve the best performance with the proposed array. As explained in Chapter 2.5, the radiation pattern of the single array element, which is rectangular microstrip patch antenna (RMSA) in this study, has a vital role on the total radiation pattern of the array. For the design of a single RMSA, design parameters; substrate with appropriate dielectric constant (ϵ_r), dielectric loss tangent ($\tan\delta$), substrate thickness (h), antenna dimensions, feeding technique and operation frequency are specified at the beginning. These design parameters have a significant role in antenna performance which are already presented in many studies [20,29,30,31]. The proposed RMSA in this thesis operates at 10 GHz and made by ROGER4003 as substrate material whose dielectric constant (ϵ_r) is 3.55 and dielectric loss tangent $\tan\delta$ is 0.0027. The final design of 10 GHz single RMSA is shown in Figure 3.19 and Table 3.1 gives the dimensions in detail.

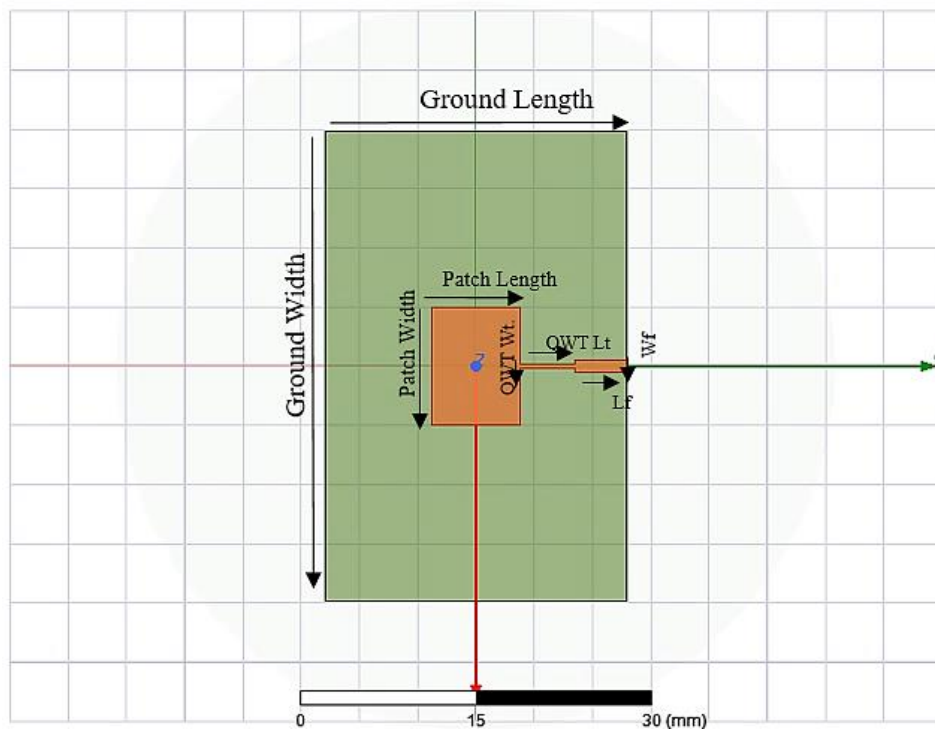
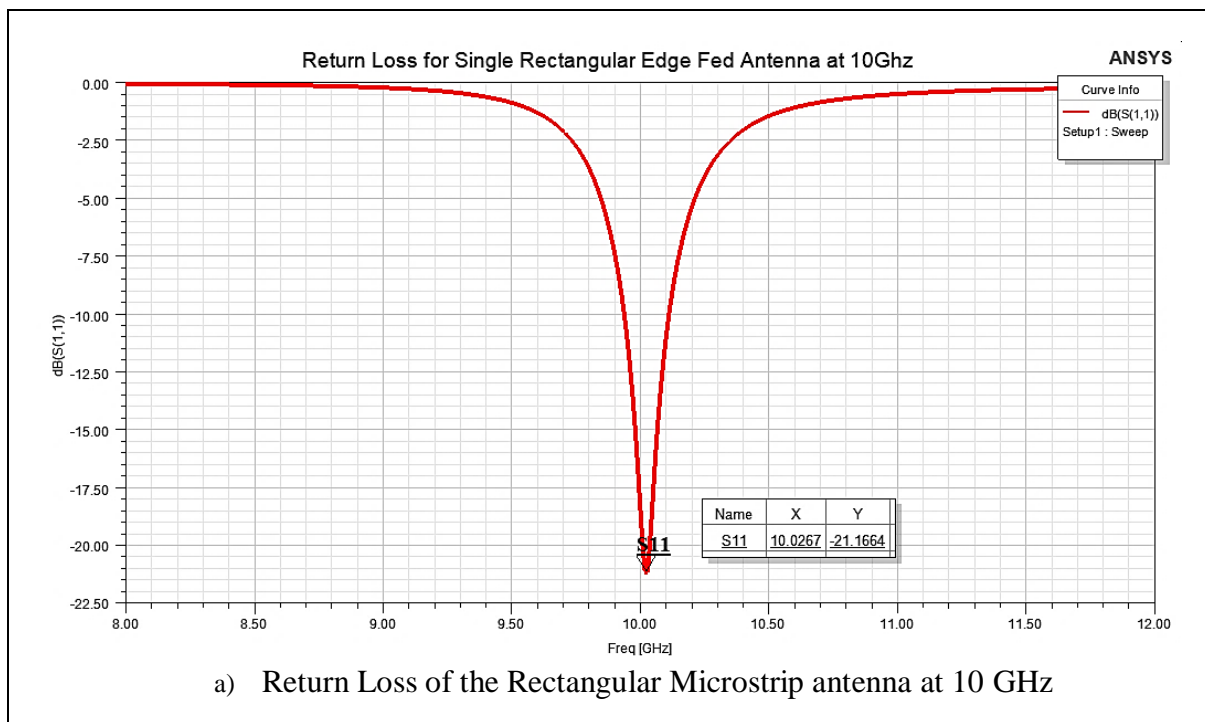


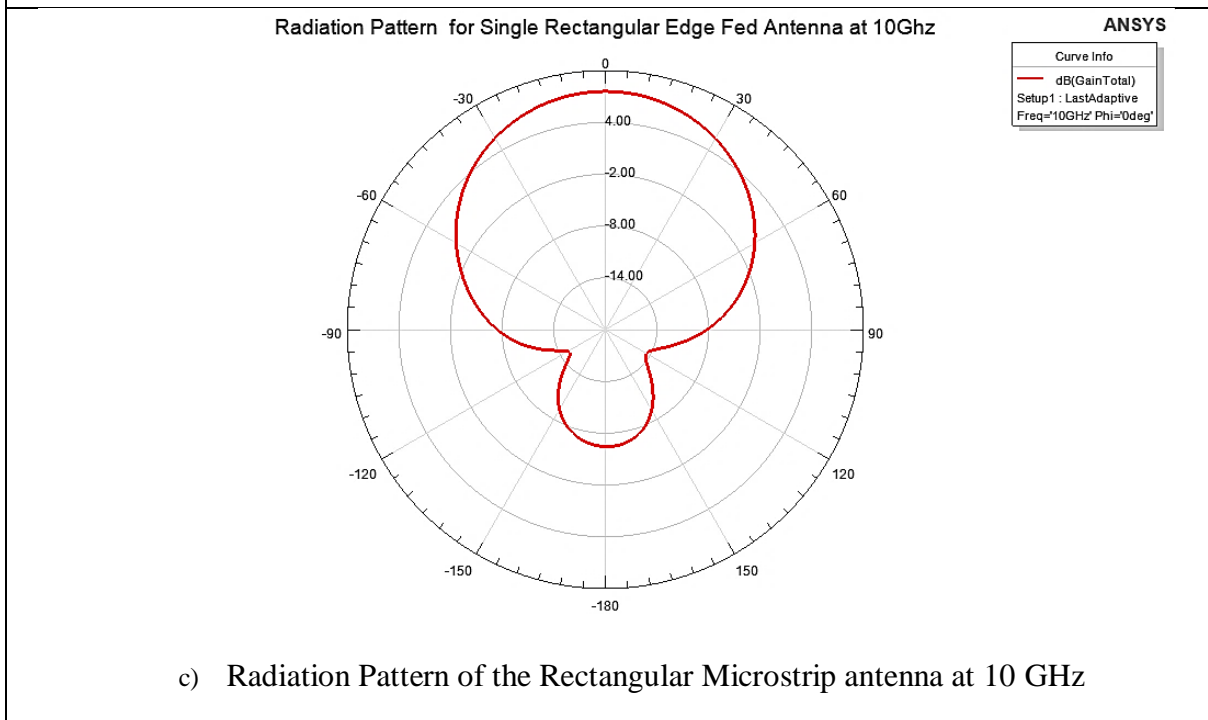
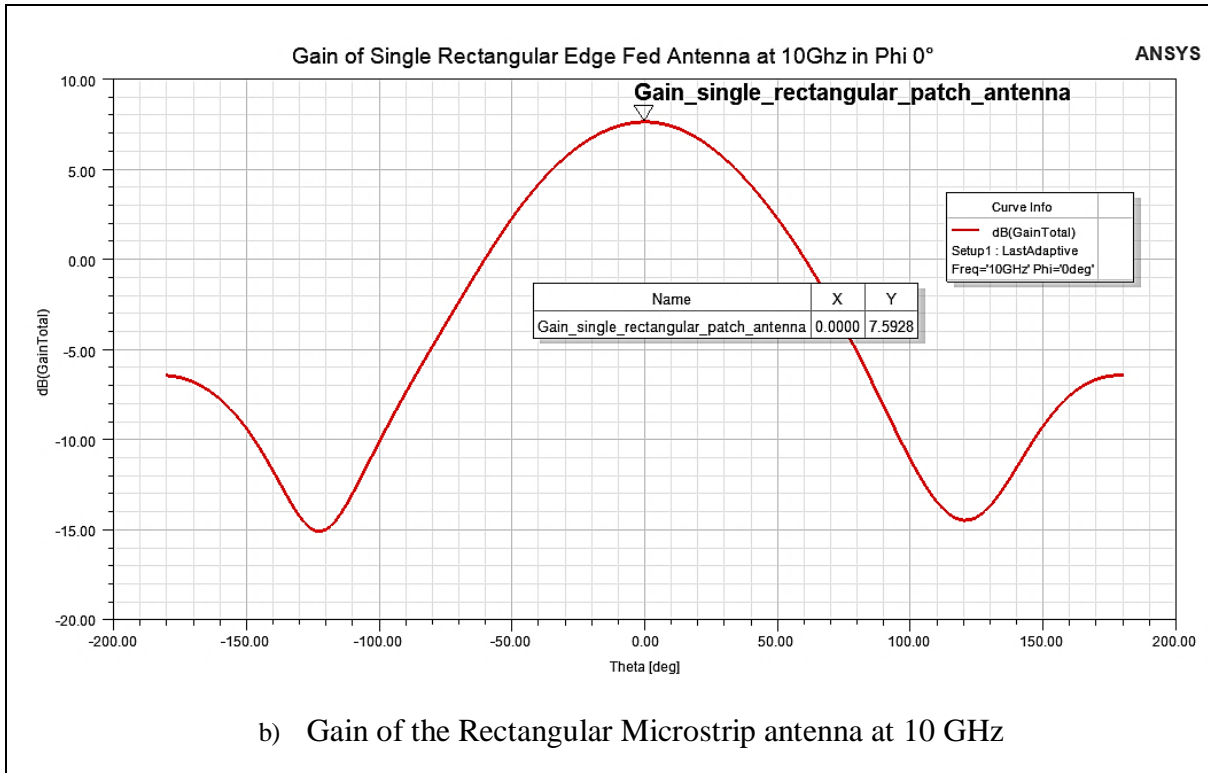
Figure 3.19 Final design of rectangular Patch antenna in HFSS

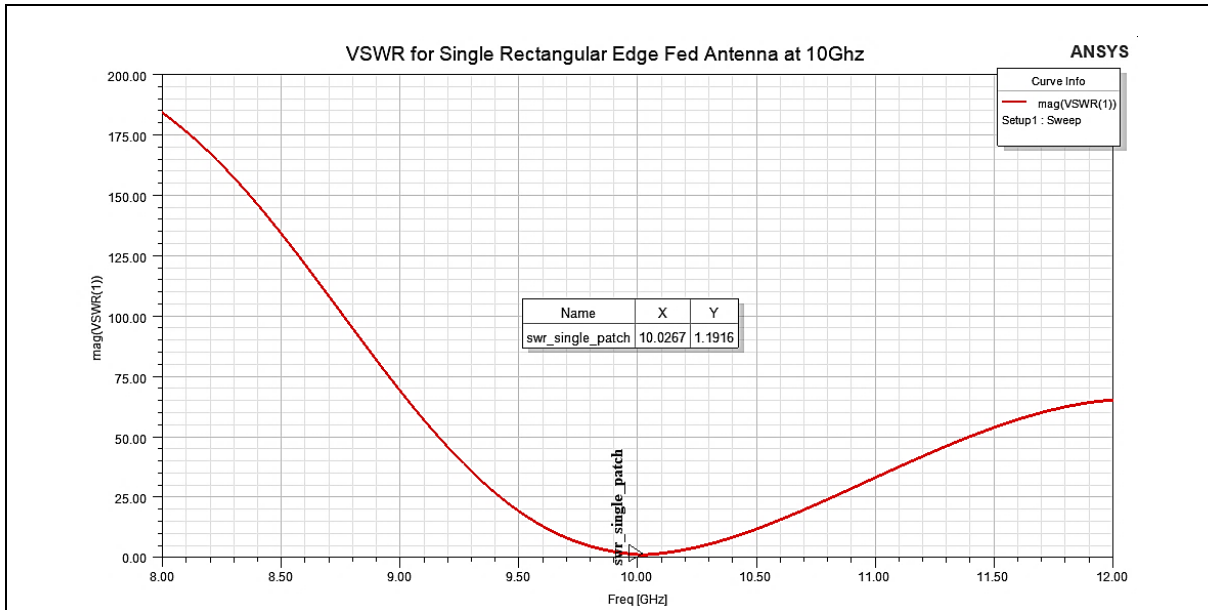
Table 3.1 Dimensions of Single Rectangular Microstrip Patch Antenna

Substrate Material	RO4003
Thickness of the substrate [mm]	0.508
Operation Frequency [GHz]	10
Dielectric constant	3.55
Ground width[mm]	39.78
Ground Length[mm]	25.922
Patch Width [mm]	9.945
Patch Length [mm]	7.52
QWT W_t (100Ω)[mm]	0.2784
QWT L_t (100Ω)[mm]	4.704
Feed length of the 50Ω [mm]	4.497
Width of the the 50Ω [mm]	1.1363

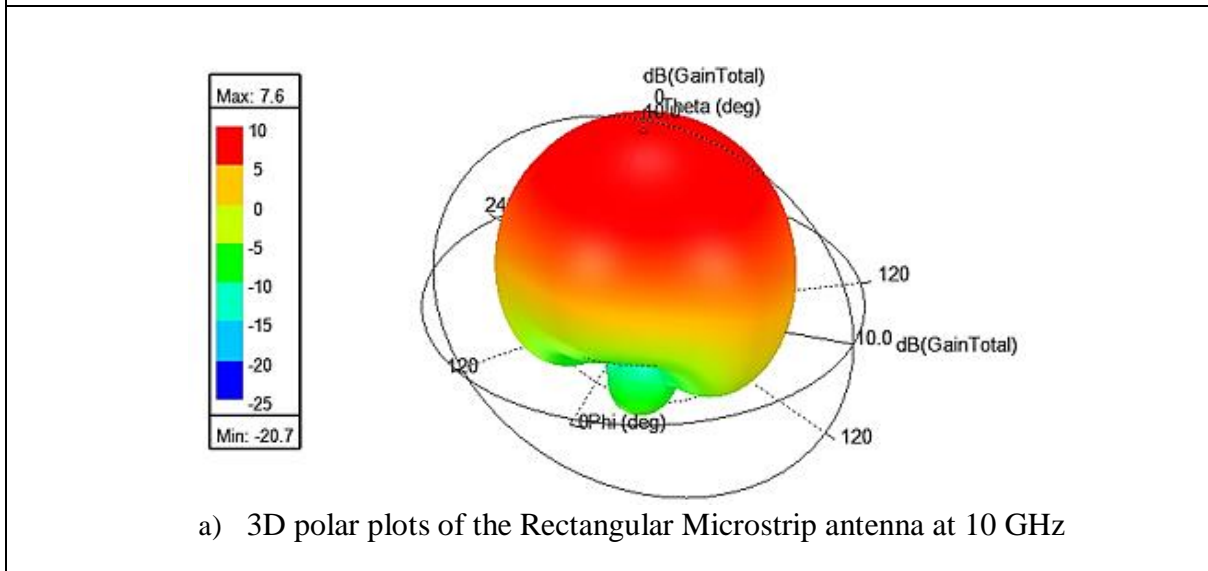
The simulation results of this proposed single RMSA is given by Figure 3.20.







d) VSWR of the Rectangular Microstrip antenna at 10 GHz



a) 3D polar plots of the Rectangular Microstrip antenna at 10 GHz

Figure 3.20 Graphical Representation of Simulation results of RMSA at 10 GHz

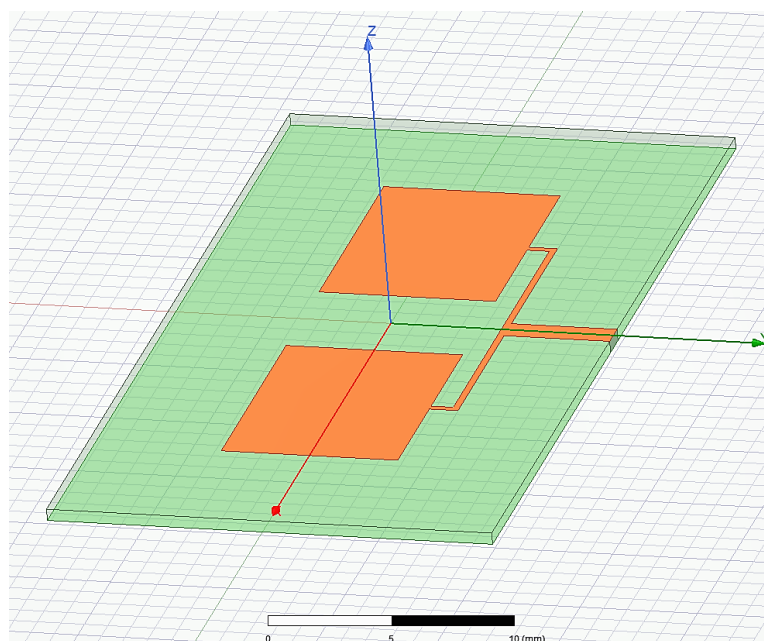
In addition to the graphical representation, Table 3.2 gives the results numerically.

Table 3.2 Numerical simulation result of Single Rectangular Patch Antenna

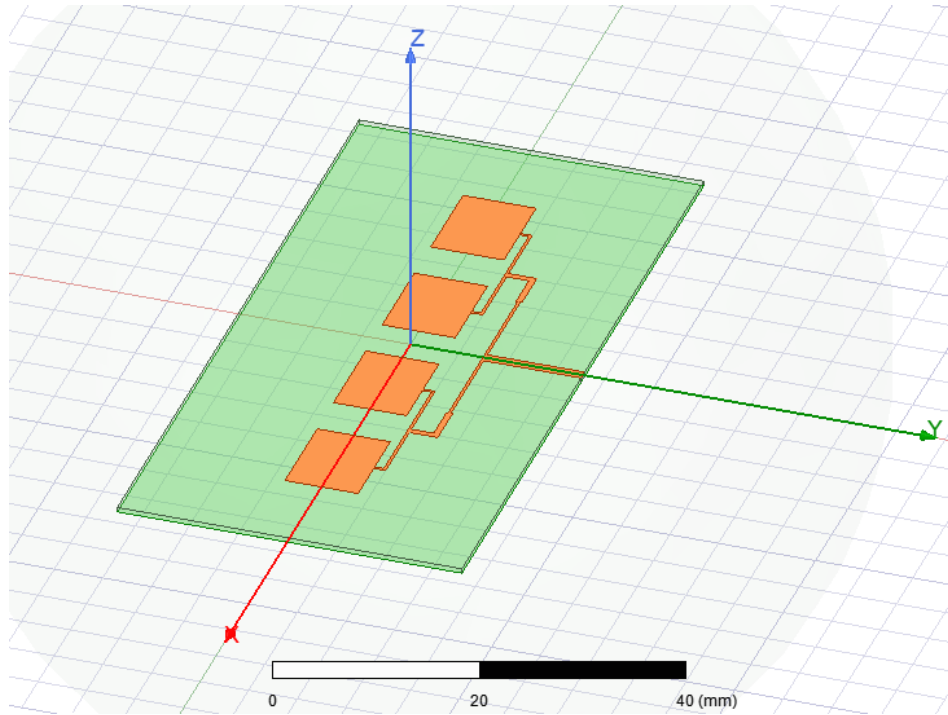
Resonance frequency f_r [GHz]	10.0267
Directivity D [dB]	7.7677
Gain [dB]	7.6
Return loss (RL) [dB]	-21.1664
Bandwidth BW (MHz)	174
VSWR	1.1916

3.4.2 Uniformly Spaced Linear Rectangular Array Antenna Designs at 10 GHz

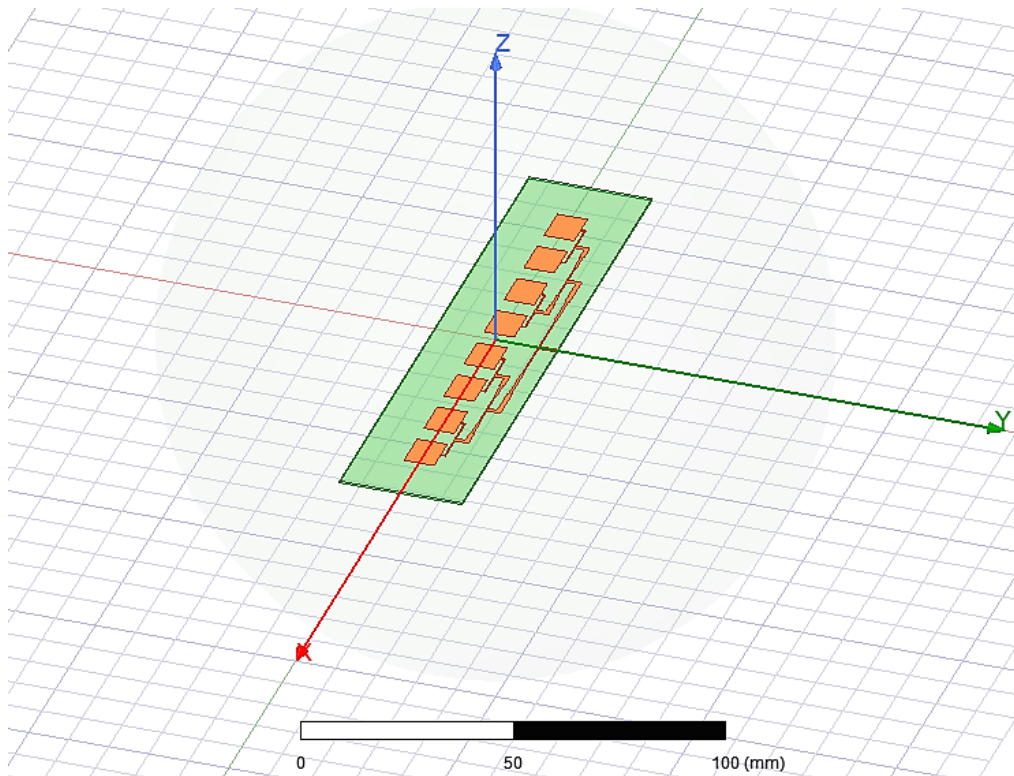
Since the single microstrip patch antenna has not enough gain as well as the directivity for high-frequency applications or long-distance transmission, the enhancement of directivity and gain is a critical point needs to be considered. Therefore, the array configuration of RMSA is preferred which provides required characteristics such as higher Gain, Directivity and Bandwidth [20]. The phased array configuration is consisting of several small antennas that are grouped together in an antenna array to achieve such a high gain and directive pattern that can be electronically scanned in a certain direction. Shaping the array radiation pattern can be achieved by appropriate element spacing as well as an appropriate magnitude and the phase of current excitation of individual elements as thoroughly explained in Chapter 2.5. In this thesis work, uniformly and non-uniformly spaced linear and planar arrays were designed and simulated with uniform amplitude current excitation. In this section, the design procedure and the simulation results of uniformly spaced linear array antennas with different number of elements are presented. Accordingly, 2x1, 4x1 and 8x1 linear arrays were designed by using the proposed single RMSA which is given in section 3.6.1. Figure 3.21 illustrates the geometrical configurations of uniformly spaced linear arrays. Here, all arrays are modelled in HFSS with each antenna element having its own excitation since this method offers the most accurate results even if requires large amount of memory and simulating time.



a) 2x1 Linear Array



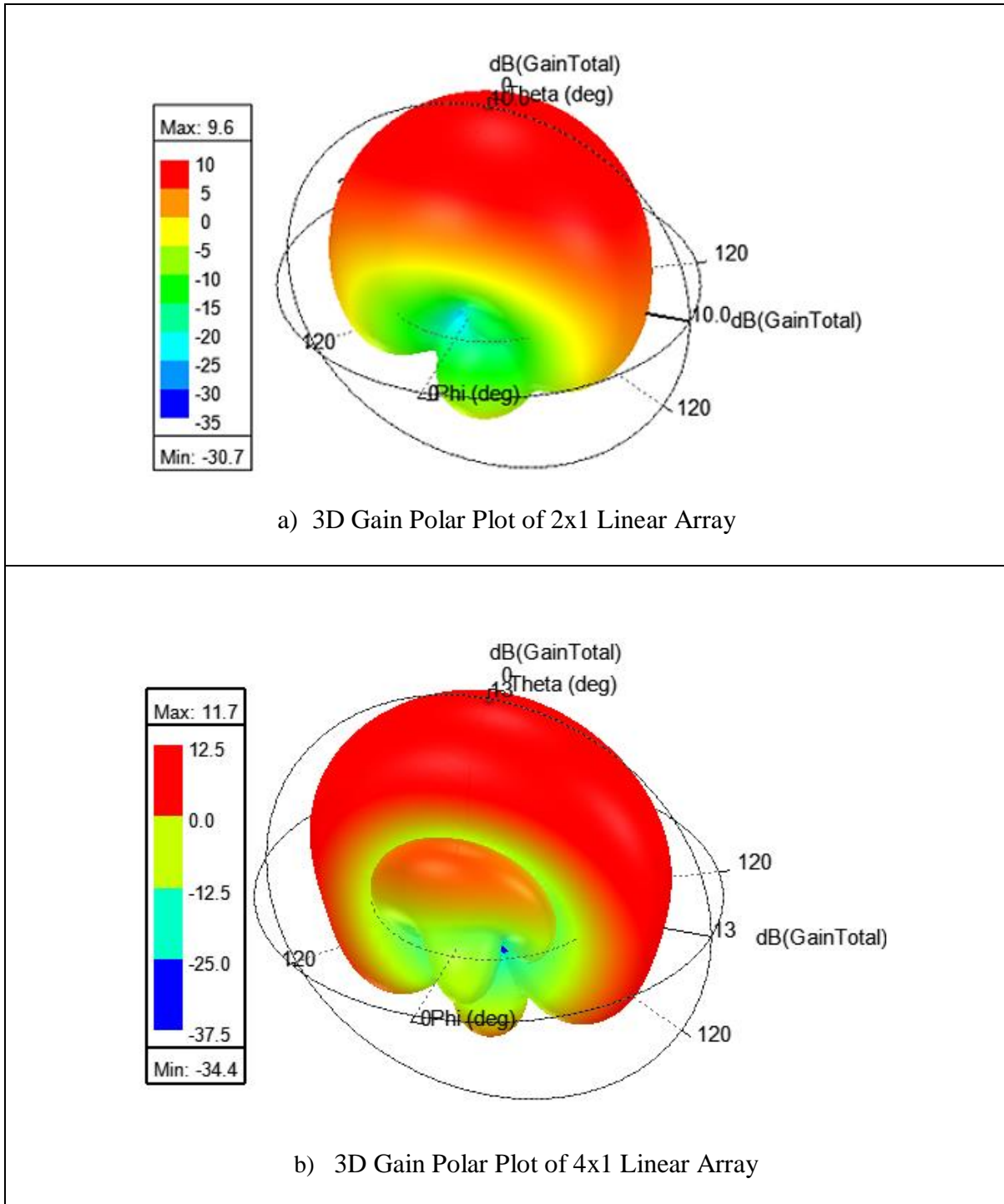
b) 4x1 Linear Array



c) 8x1 Linear Array

Figure 3.21 Final design of Linear arrays in HFSS

In these designs, the individual patch antenna geometry is the same for all of these arrays. The differences are just the sizes of the substrate and ground due to the increased number of elements. In addition, all these linear arrays are fed by the corporate feed network. Instead of giving all the graphical simulation results obtained in HFSS, 3D gain plots of each are given in Figure 3.22. All numerical simulation results are also given numerically in Table 3.3.



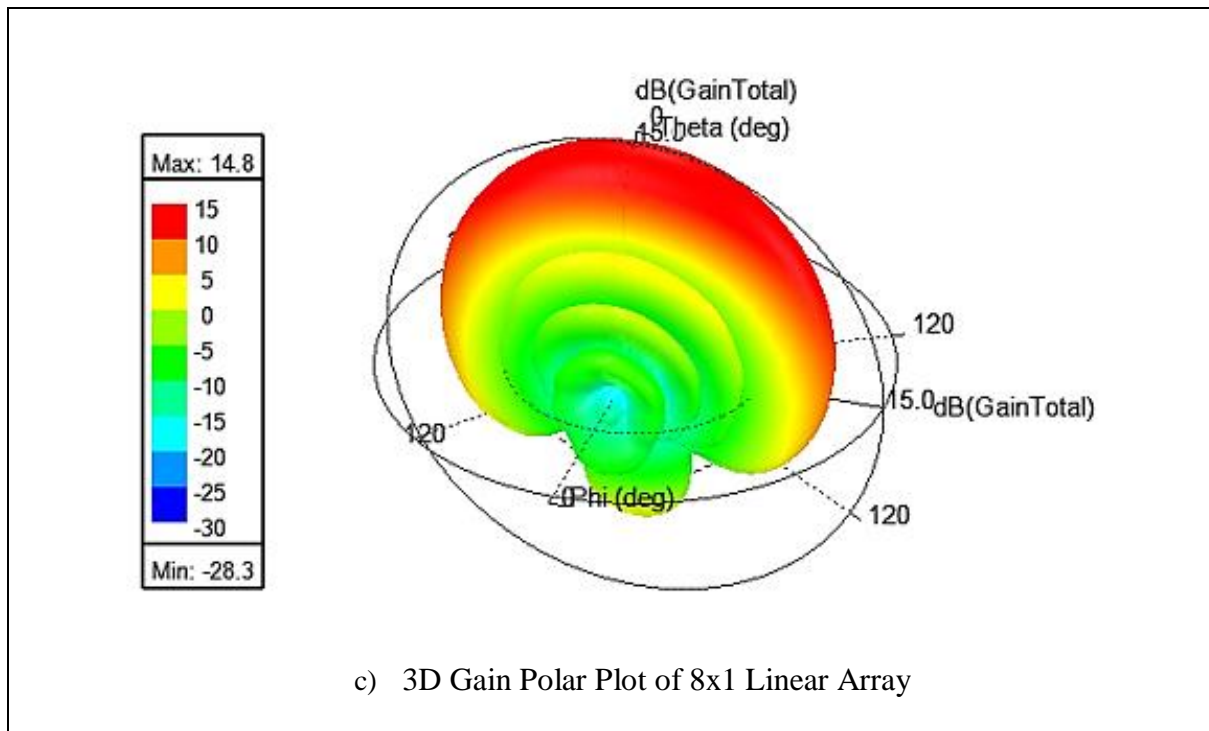


Figure 3.22 Graphical Simulation result of Linear array antennas 3D Gain Polar Plot

Table 3.3 Numerical Simulation Result of Linear Array Antennas

Linear Array with 0.5 lambda space	2x1	4x1	8x1
Resonance frequency f_r [GHz]	10.0089	10.0889	10.0178
Directivity D [dB]	9.5179	11.9324	14.7931
Gain [dB]	9.5388	11.7153	14.7839
Return loss (RL) [dB]	-20.5793	-19.9324	-21.7539
Bandwidth BW [MHz]	284.4	275.6	177.8
VSWR	1.2064	1.3082	1.1780

Some observations from Figures 3.22 and Table 3.3 can be concluded as follows:

- When the number of elements increases, the beamwidth as well as the bandwidth reduces since the antenna becomes more directive.
- When the number of elements increases, the gain of the antenna notably increases.
- The number of nulls and side lobes increases as the number of elements increases.

As mentioned in Chapter 2.5, the inter-element spacing between the adjacent element is quite critical parameter which causes the existence of grating lobes. When the inter-element spacing is greater or equal than the one wavelength ($d \geq \lambda$), grating lobes appear. Figure 3.23 shows the comparison of inter-element spacing $d=1.5\lambda$ and $d=0.5\lambda$ for the 2x1 linear array. The red line on the plot represents the array pattern with grating lobes. In addition to this observation, when the spacing between the element increases, the gain, number of nulls and side lobes also increases, and the beam width becomes narrower.

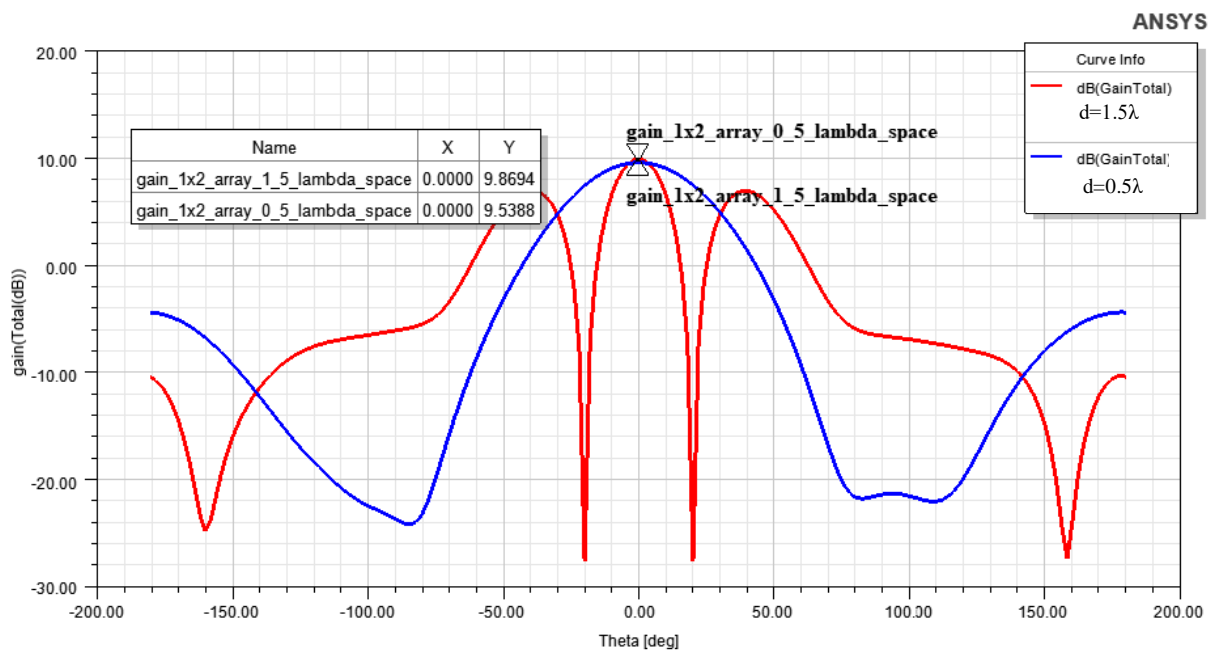
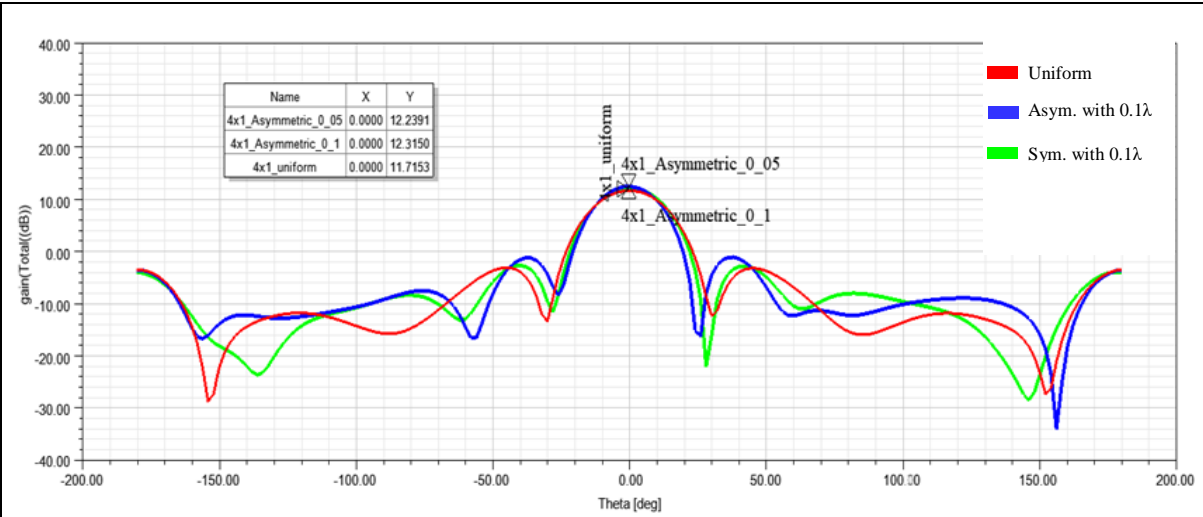


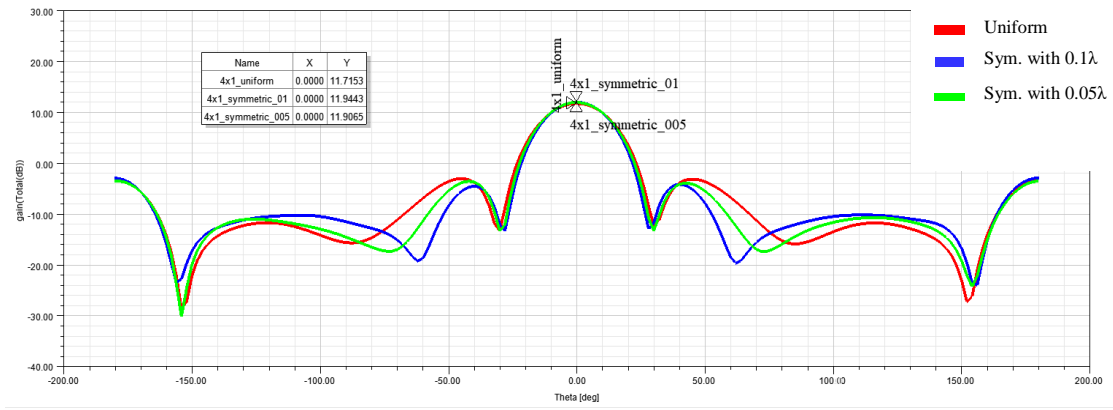
Figure 3.23 Gain comparison of 2x1 Linear Array with different inter-element spacing

3.4.3 Non-uniformly Spaced Linear Rectangular Array Antenna Designs at 10 GHz

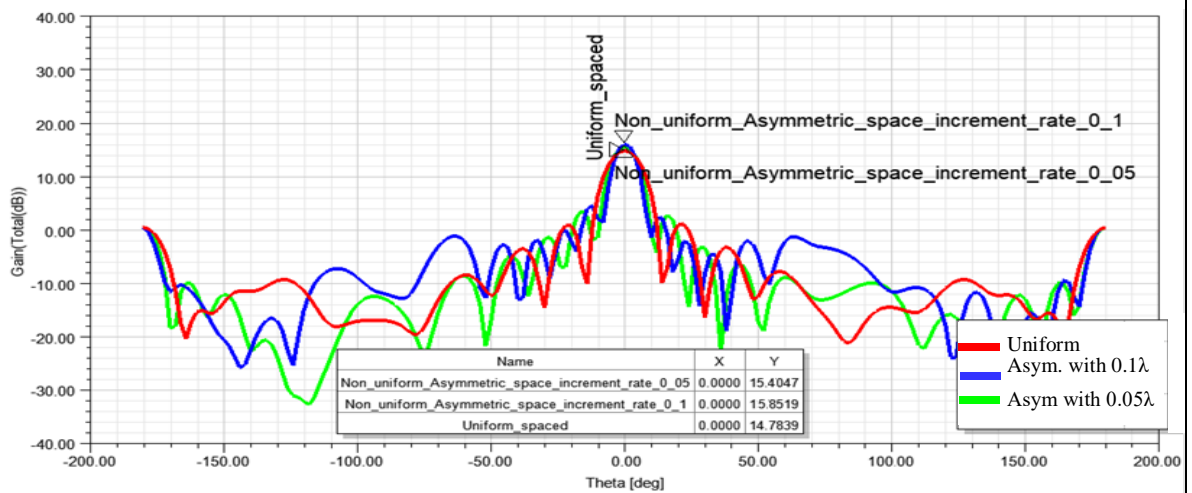
In order to decrease the side lobe levels and thereby to increase the overall array performance, arrays are now designed and simulated with non-uniform (unequal) spacing keeping the excitation amplitude uniform. In non-uniform spacing, the same configurations, which are asymmetrical and symmetrical arrays with the increase rates of 0.1λ and 0.05λ have been used as already given in Chapter 3.5. Figure 3.24 is the graphical representation of the simulation results for uniform and non-uniform arrangements of 4x1 and 8x1 linear arrays.



a) 2D Cartesian Plots of Uniform and Asymmetric 4x1 Linear Arrays



b) 2D Cartesian Plots of Uniform and Symmetric 4x1 Linear Arrays



c) 2D Cartesian Plots of Uniform and Asymmetric 8x1 Linear Arrays

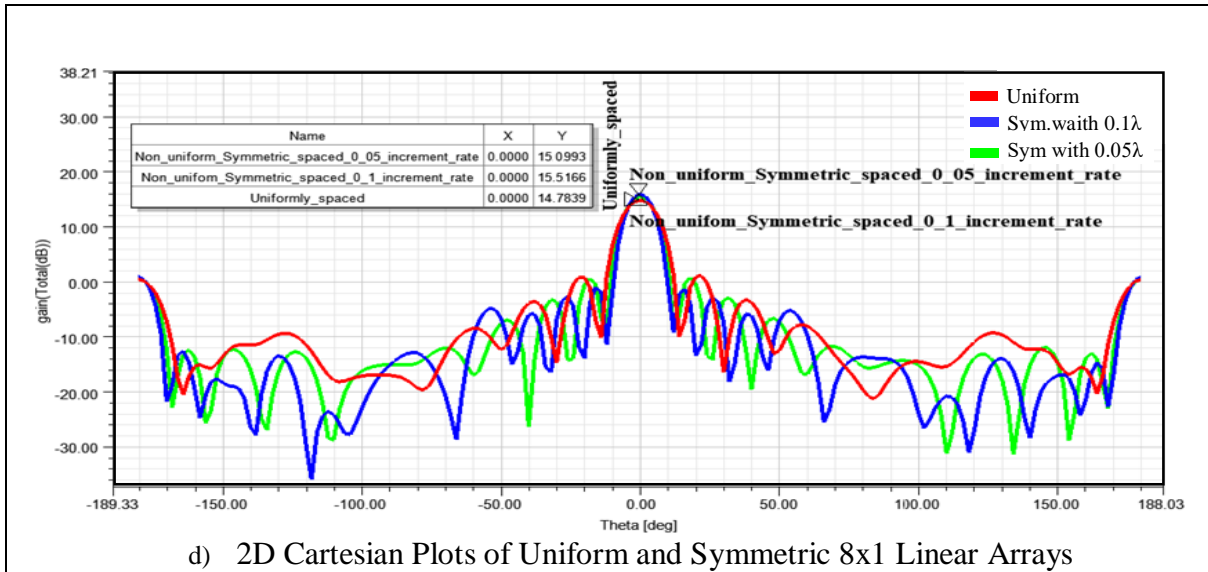


Figure 3.24 Gain patterns of Uniform and Non-Uniform broadside linear arrays along x- axis

Table 3.4 and 3.5 gives the numerical results of 8x1 and 4x1 linear arrays with different geometrical configurations.

Table 3.4 Numerical simulation results of 8x1 linear arrays

Characteristics	Uniform Space	Symmetrical with 0.1λ ir	Symmetrical with 0.05λ ir	Asymmetrical with 0.1λ ir	Asymmetrical with 0.05λ ir
f_r [GHz]	10.0178	10.0356	10.0089	10.0178	10.0178
Directivity D [dB]	14.7931	15.7136	15.1982	15.9501	15.5233
Gain [dB]	14.7839	15.5166	15.0993	15.8519	15.4047
Return loss [dB]	-21.7539	-21.5850	-21.8692	-18.2876	-18.0921
VSWR [Mag]	1.1780	1.1818	1.1754	1.2774	1.28

*ir: increase rate f_r , : Resonance frequency

Table 3.5 Numerical simulation results of 4x1 linear arrays

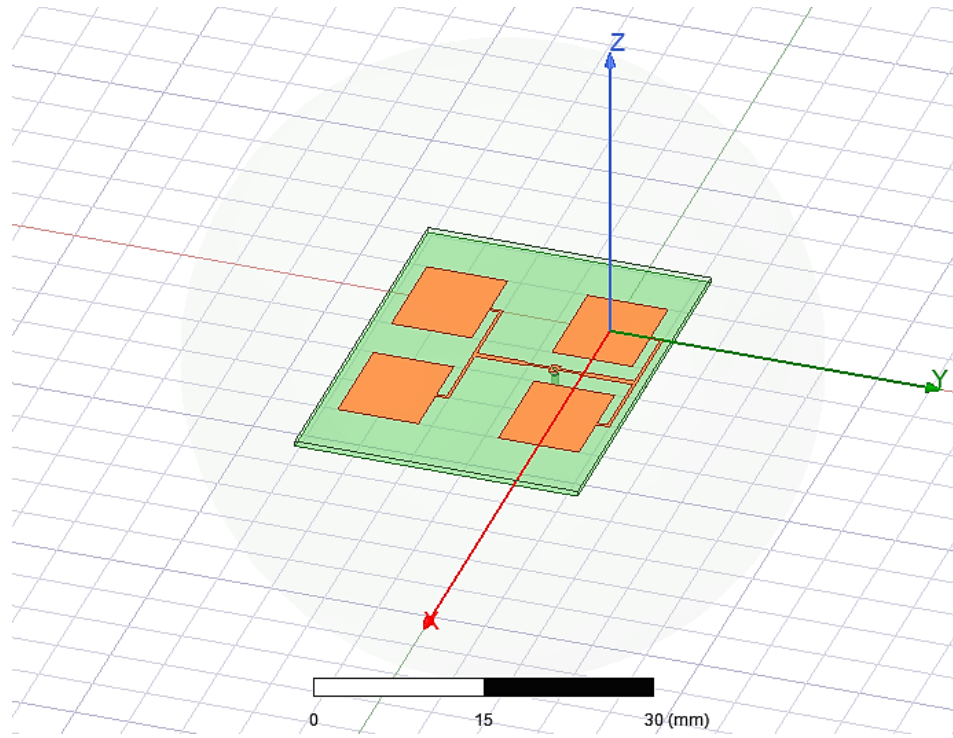
Characteristics	Uniform Space	Symmetrical with 0.1λ ir	Symmetrical with 0.05λ ir	Asymmetrical with 0.1λ ir	Asymmetrical with 0.05λ ir
f_r [GHz]	10.0889	10.0178	10.0444	10	10.0178
Directivity D [dB]	11.9324	12.1049	11.9335	12.4165	12.3238
Gain [dB]	11.7153	11.9443	11.8065	12.3150	12.2391
Return loss [dB]	-19.0310	-17.9861	-20.1788	-17.9557	-19.9446
VSWR [Mag]	1.3082	1.2886	1.2172	1.2897	1.2238

*ir: increase rate f_r , : Resonance frequency

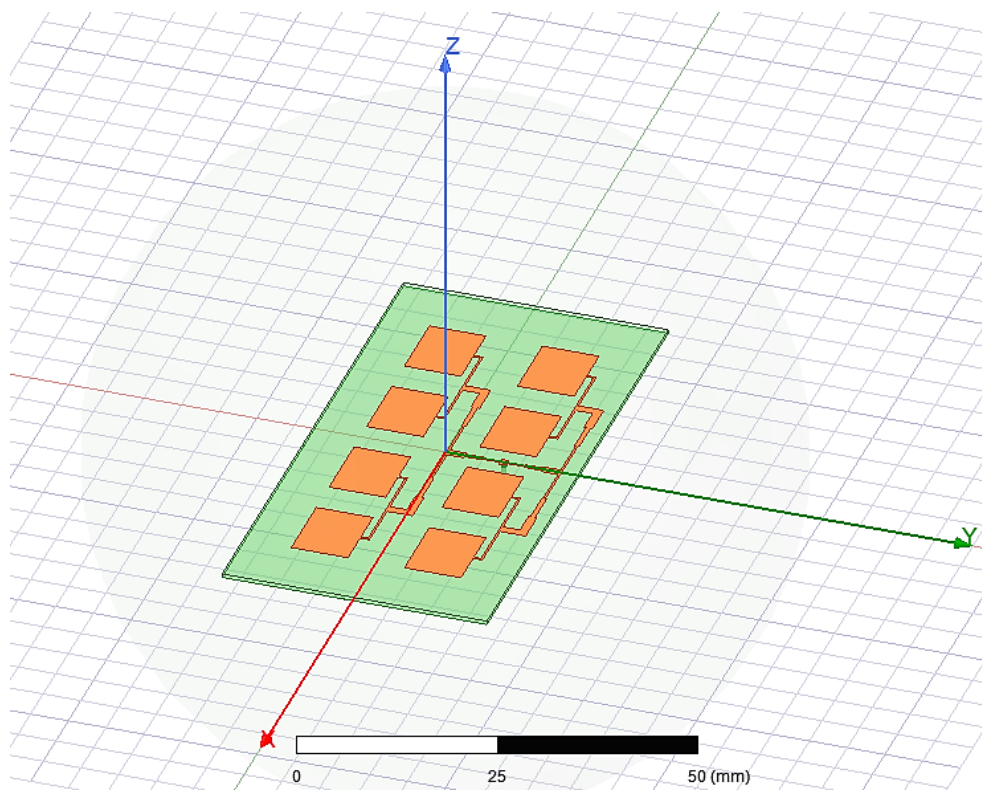
As obtained in the developed Python simulator, an obvious improvement is not obtained in side lobe level reduction for asymmetrical configurations as shown by Figure 3.24 (a) and (c). Nevertheless, gain of asymmetrical arrays seems slightly higher than symmetrical and uniform arrays as a result of narrower beamwidth. Despite this slight gain enhancement, using an asymmetrical array would not be efficient due to the relatively longer array length. On the other hand, noticeable enhancements in sidelobe level reduction is now visible by non-uniform symmetrical arrangement with 0.1λ as increase rate which also provides shorter array length than asymmetrical configurations. It should be also definitely noted that the number of sidelobes increases even if the SLL decreases with symmetrical arrays.

3.4.4 Uniformly Spaced Planar Rectangular Array Antenna Designs at 10 GHz

Planar array antennas consist of many numbers of microstrip patch antennas along two axes that provide relatively higher gain and directivity rather than linear arrays. Symmetrical pattern of planar arrays also provides lower side lobe levels as observed earlier in linear arrays and more directional beam. In this thesis work, single RMSA are used to design planar antenna arrays along x- and y- direction. Inter-element spacing between each element in the arrays is obtained to avoid the grating lobes by giving the spacing on x-axis as 0.5λ and on y- axis as 0.5λ . or 0.58λ (depending on the array geometry considering feed lines). Figure 3.25 illustrates the 2x2 ,4x2 and 8x2 uniformly spaced planar arrays with coaxial feed.



a) 2x2 Planar Array



b) 4x2 Planar Array

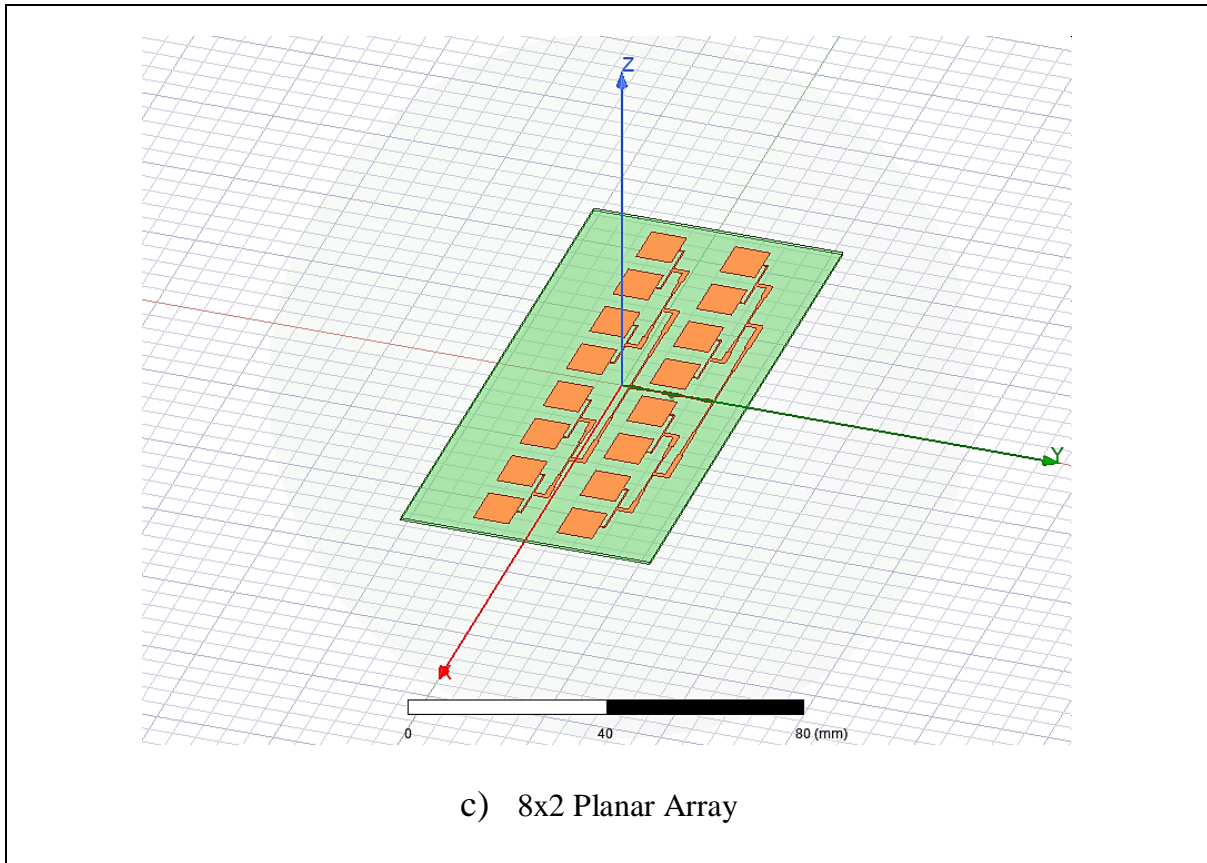
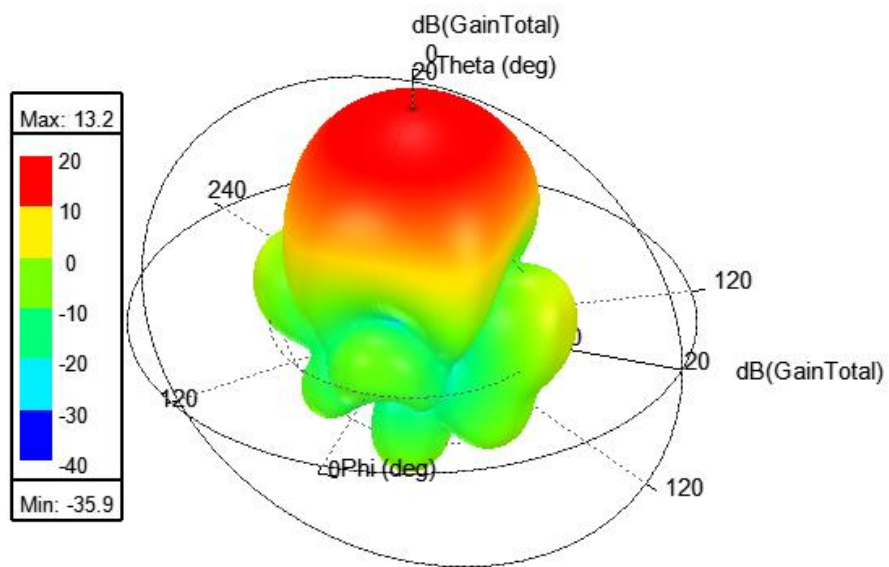
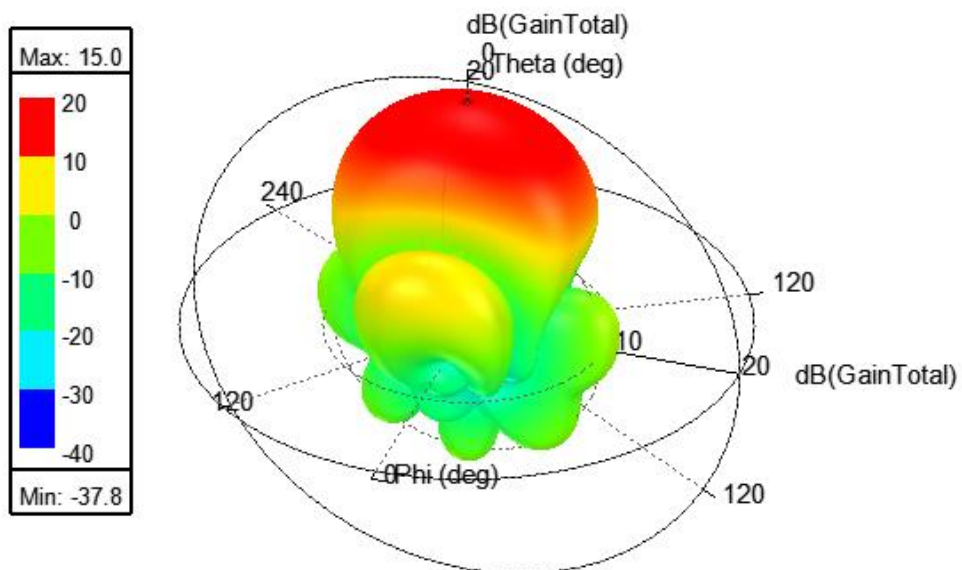


Figure 3.25 Final design of Planar arrays in HFSS

In these planar array designs, the individual patch antenna geometry is the same for all of these arrays. The only differences are just the sizes of the substrate and the ground due to the increased number of elements. In addition, the 0.58λ separation are used along y- axis to avoid superposition of bottom side of patches and upper side of feed network of 4x2 and 8x2 arrays. Instead of giving all the graphical simulation results obtained in HFSS, 3D gain plots of each are given in Figure 3.26 and all numerical simulation results are given numerically in Table 3.6.



a) 3D Gain Polar Plot of 2x2 Planar Array



b) 3D Gain Polar Plot of 4x2 Planar Array

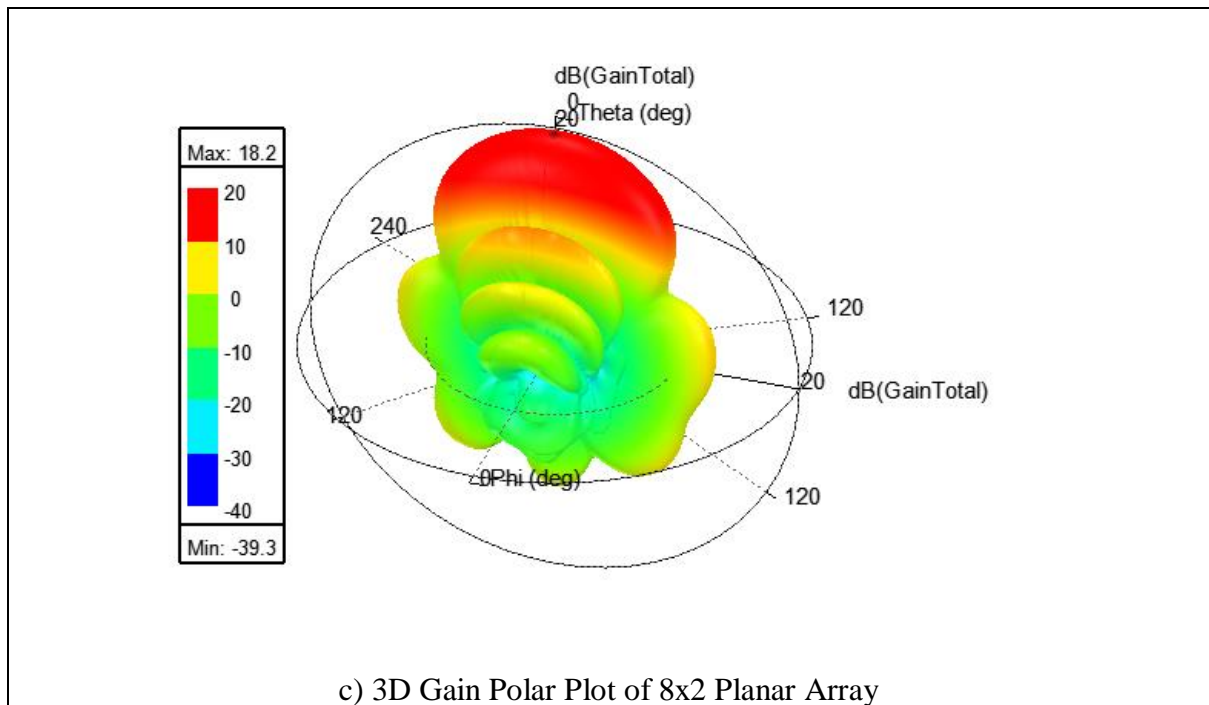


Figure 3.26 Graphical Simulation result of Linear array antennas 3D Gain Polar Plot

Table 3.6 Numerical Simulation Result of Planar Array Antennas

Planar Array	2x2	4x2	8x2
Resonance frequency f_r [GHz]	10	9.8311	9.83
Directivity D [dB]	13.37	15.3156	18.27
Gain [dB]	13.19	14.9542	18.15
Return loss (RL) [dB]	-21.38	-19.6912	-32.13
Bandwidth BW [MHz]	204.4	124.4	105.2
VSWR	1.19	1.2312	1.36

According to the results, it can be obviously observed that when the number of elements increases, the antenna becomes more directive and have more gain. In addition, the number of side lobe and nulls increases. As already mentioned above, the planar arrays have less number of sidelobes and more directive beam as a result of scanning the main beam along both θ and ϕ .

Figure 3.27 shows the comparison of linear and planar arrays with the same total number of elements. According to results of HFSS simulation, the linear array antenna has a greater number of side lobes and narrower beamwidth. Thus, the planar arrays would be more preferable if the application requires high directive antenna array.

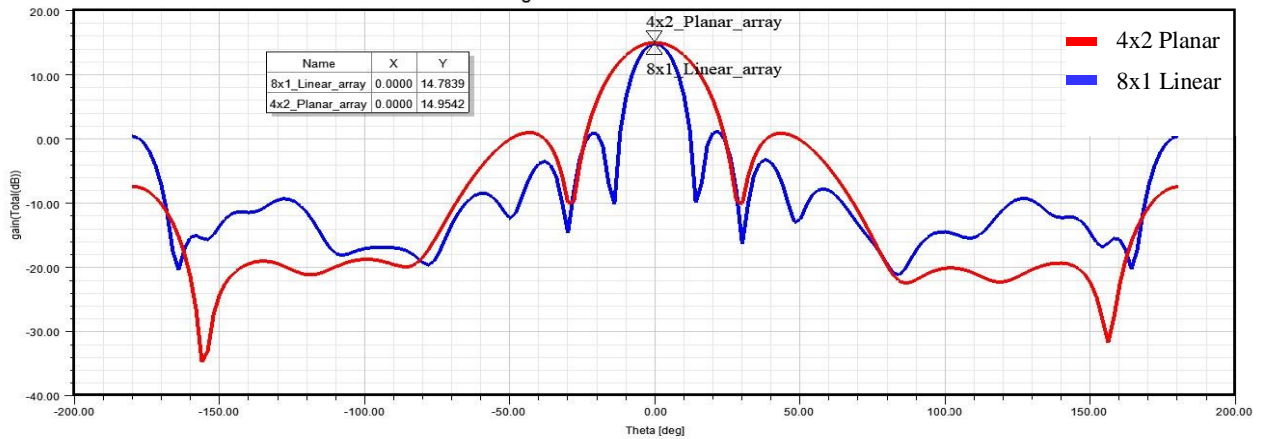


Figure 3.27 Gain Patterns of 8x1 Linear vs 4x2 Planar Arrays in HFSS

3.4.5 Non-Uniformly Spaced Planar Rectangular Array Antenna Designs at 10 GHz

As earlier implemented for linear array configurations, planar arrays were also designed and simulated with non-uniform (unequal) spacing keeping the excitation amplitude uniform to observe the array performance. According to the observations from linear arrays, planar arrays were not analyzed with 0.05λ as increase rate since it does not provide satisfactory outcomes. Figure 3.28 gives the comparison of linear array planar arrays with different array layouts. As earlier obtained in linear arrays, the asymmetrical configurations do not provide a sufficient enhancement for sidelobe level reduction in planar arrays either. This must also be remembered that the enhancement becomes more obvious for the arrays with higher number of elements.

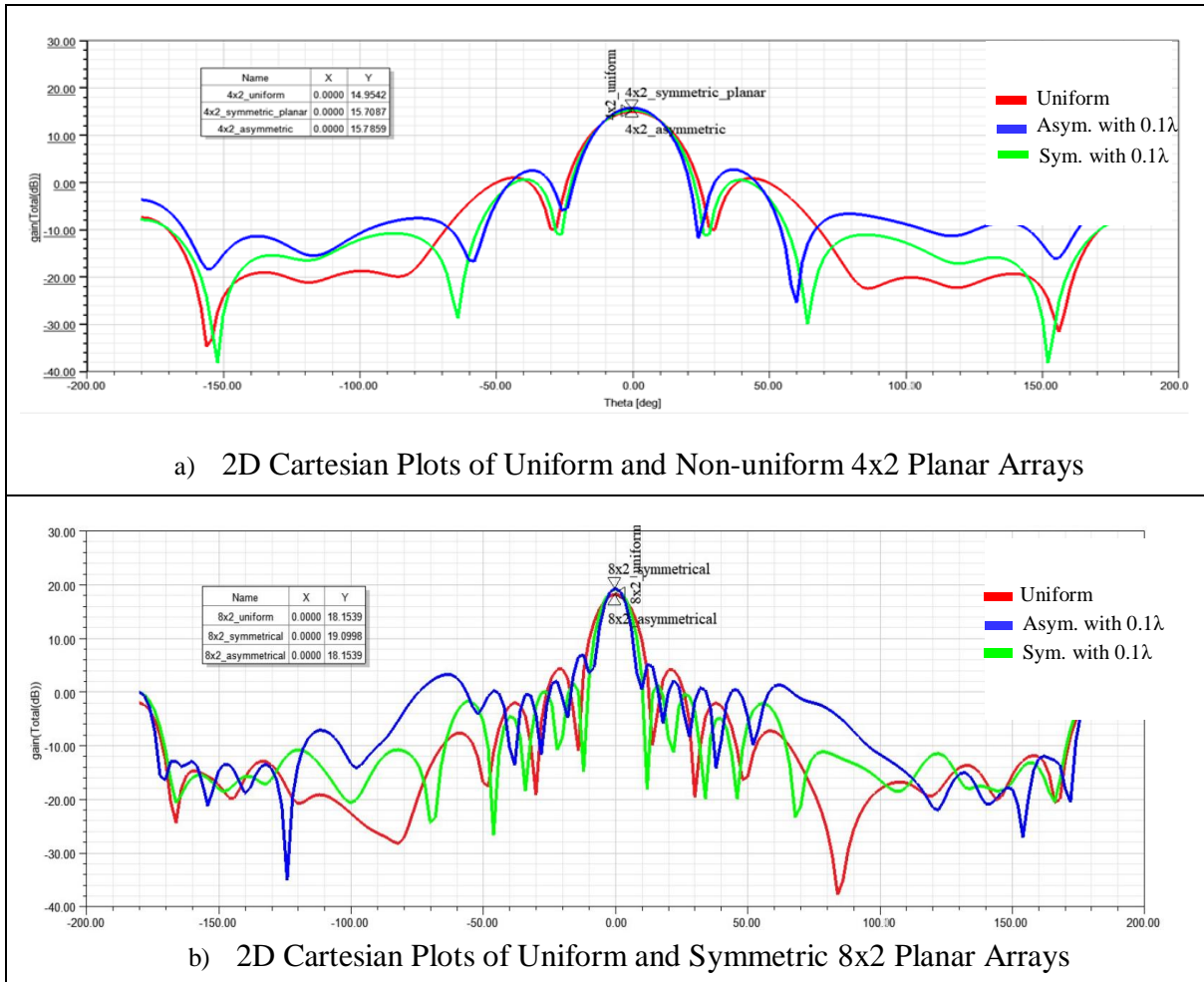


Figure 3.28 Gain patterns of Uniform and Non-Uniform broadside planar arrays along x- and y- axes

Table 3.7 and 3.8 gives the numerical results of 4x2 and 8x2 planar arrays with different geometrical configurations.

Table 3.7 Numerical simulation results of 4x2 planar arrays

Characteristics	Uniform	Symmetrical with 0.1λ ir	Asymmetrical with 0.1λ ir
f_r [GHz]	9.8311	10.3	10
Directivity D [dB]	15.3156	15.9170	15.85
Gain [dB]	14.9542	15.7087	15.78
Return loss [dB]	-19.6921	-21.1416	-19.2153
VSWR [Mag]	1.2312	1.1922	1.2979

*ir: increase rate f_r ,: Resonance frequency

Table 3.8 Numerical simulation results of 8x2 planar arrays

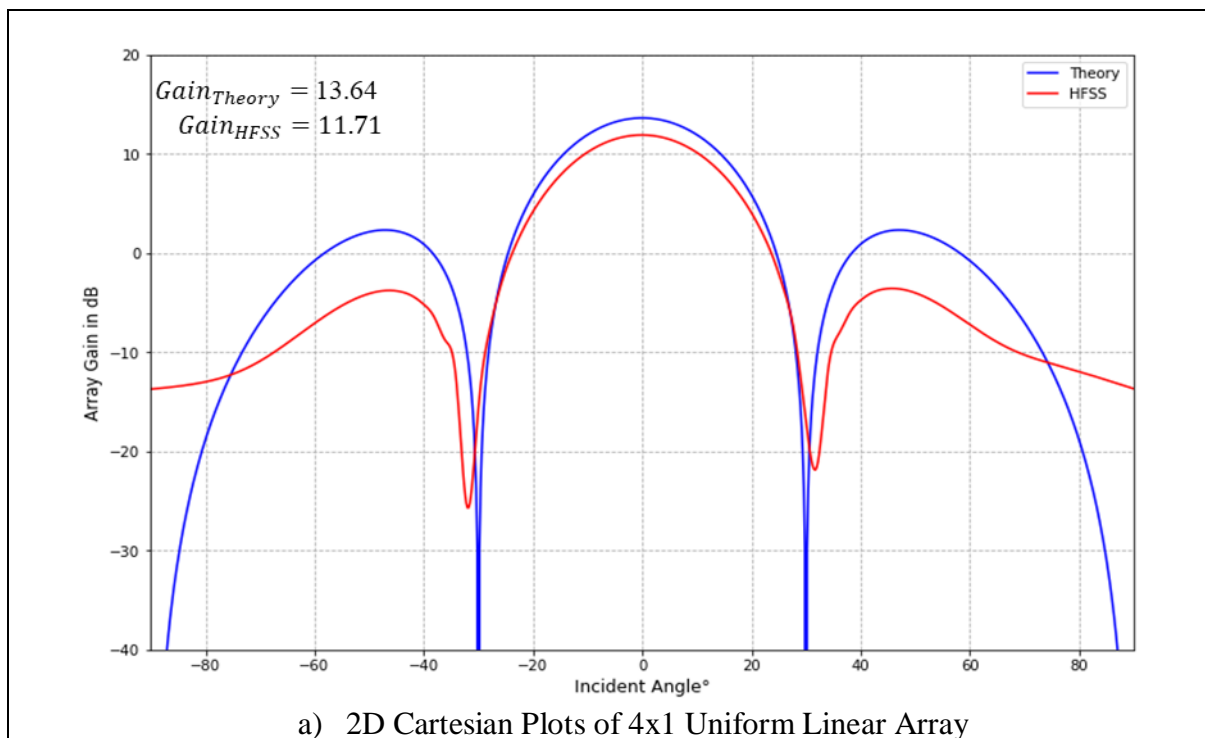
Characteristics	Uniform	Symmetrical with 0.1λ ir	Asymmetrical with 0.1λ ir
f_r [GHz]	9.83	10.0178	10.0089
Directivity D [dB]	18.27	19.3283	19.6171
Gain [dB]	18.15	19.0998	19.2887
Return loss [dB]	-32.13	-22.2920	-20.3061
VSWR [Mag]	1.36	1.3271	1.2762

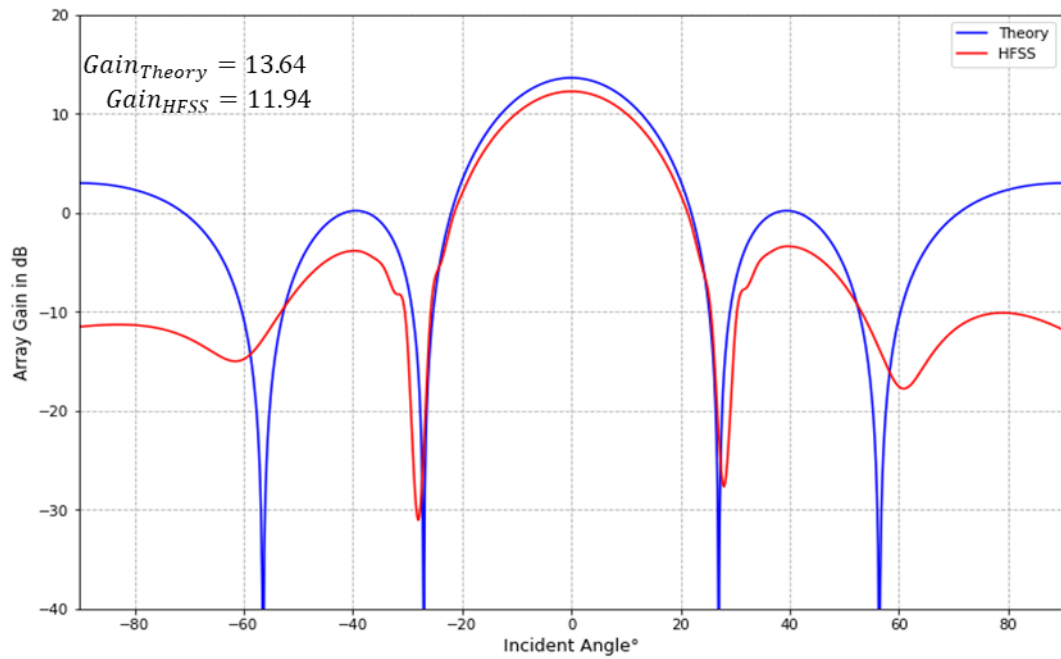
*ir: increase rate f_r , : Resonance frequency

3.5 Comparison of Theory and Simulation

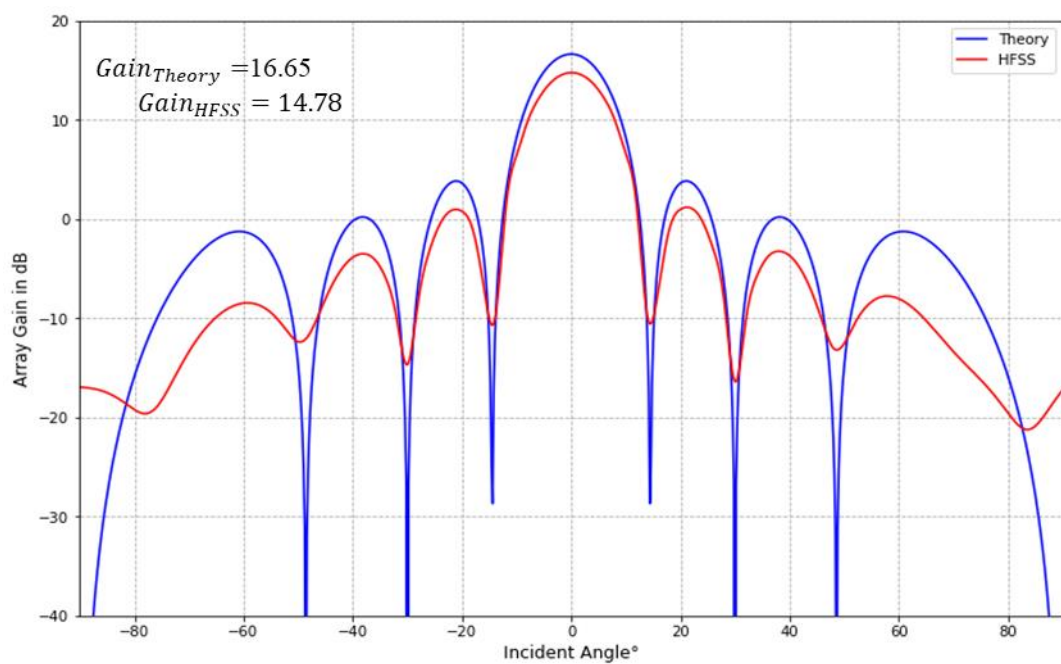
In this part, the simulation results of 2D Gain patterns obtained in developed Python simulator and HFSS are compared. Hence, the differences between the classical approach, which is based on antenna array theory, and Floquet Model approach, which is the basis of HFSS tool, are able to be observed. Floquet analysis, or HFSS, provides remarkable advantages since it considers the mutual coupling effects on the input impedance of array elements as well as additional losses which are Radiation Loss, Impedance Mismatch Loss, Dielectric Loss, and Conducting Loss. **In a Conductor**, there are few mechanisms of energy dissipation both at Low Frequency (LF) and High Frequency (HF). One of the common energy dissipations is the ohmic heating of electrical resistance of conductor at LF. In the case of HF, there is a change of current distribution along the conductor [52] in addition to the ohmic heating. This change contains two additional crucial effects which are the Skin effect and the Current Crowding. Skin Effect is non-uniform distribution of electric current over the conductor's surface. In other words, the concentration of charge is nearer the surface as compared to the center of the conductor. The ohmic resistance of the conductor is increased due to the concentration of current on the skin or surface of the conductor [53]. In addition, this effect increases with the increase in frequency [53]. Current crowding is a powerful function of frequency that causes the increase of effective resistance [53]. **In Substrate or Dielectric Losses** which, cause Eddy Current, Strong Capacitance and Dielectric Polarization, depend on the frequency. Eddy Current is appearing if the substrate is semiconductor. It occurs when the magnetic fields penetrate material, and they induce the parasitic current along the thickness and width of the substrate [53]. Dielectric polarization is all about the complex permittivity which is strong function of the frequency.

Therefore, the loss tangent and dissipation factor must be checked from the datasheet of relevant material for the Dielectric Polarization. The loss tangent and dissipation factor parameters are also important to measure the isolation degree [52]. Lastly, the strong capacitance is another critical parameter for antenna’s design because it shows how powerful electric field is inside the substrate. **Radiation Loss**, which is crucial parameter for input impedance as mentioned in section 2.2, is caused by radiation resistance. This impedance is present at the antenna’s feed point. Its real part, R_{in} , can be split up into the radiation resistance (R_{rad}) and the loss resistance (R_{loss}). The loss resistance shows the radiation loss which results in re-radiating RF energy from transmission lines [6]. **Impedance mismatch Loss** is also critical parameter since it describes how much RF power is transferred from source to the load. In theory, the source and load impedances should be matched. However, in practice there will be loss due to mismatch loss and often equals on the order of 1dB [7]. Hence, some discrepancies would be expected between the simulations in theory and HFSS with respect to the aforementioned losses.





b) 2D Cartesian Plots of 4x1 Non-uniform Symmetric Linear Array



c) 2D Cartesian Plots of 8x1 Uniform Linear Array

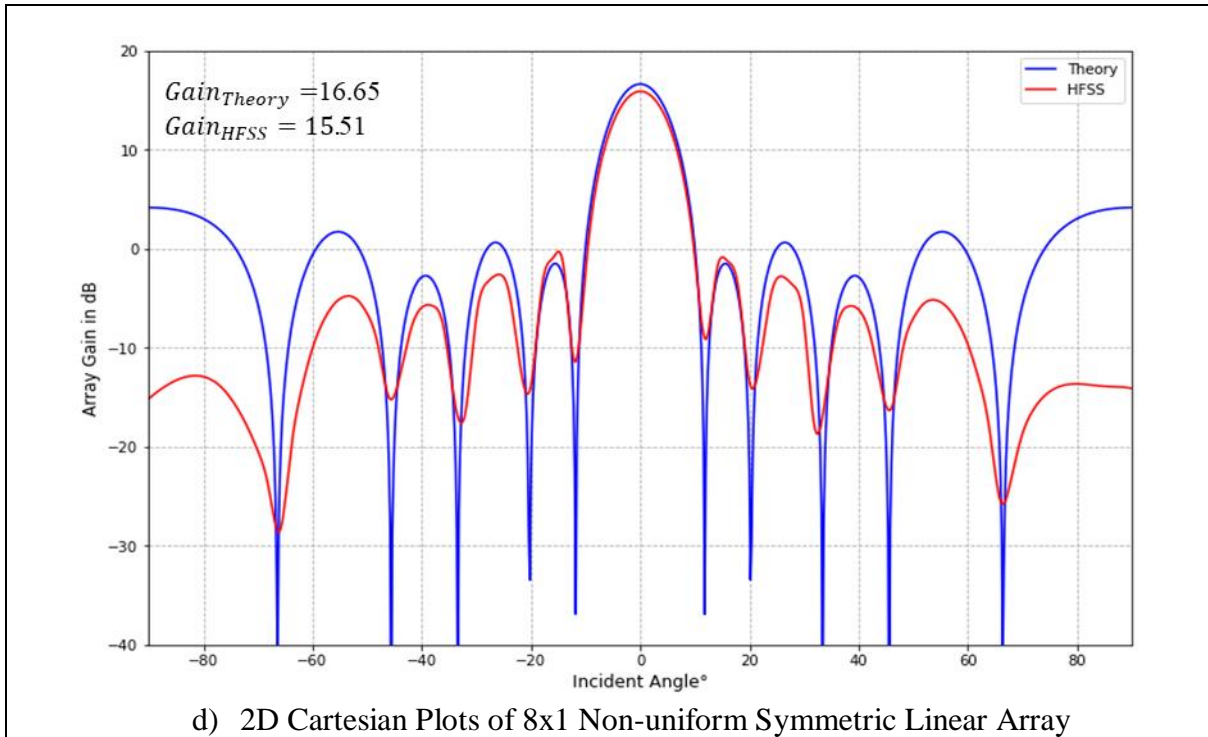
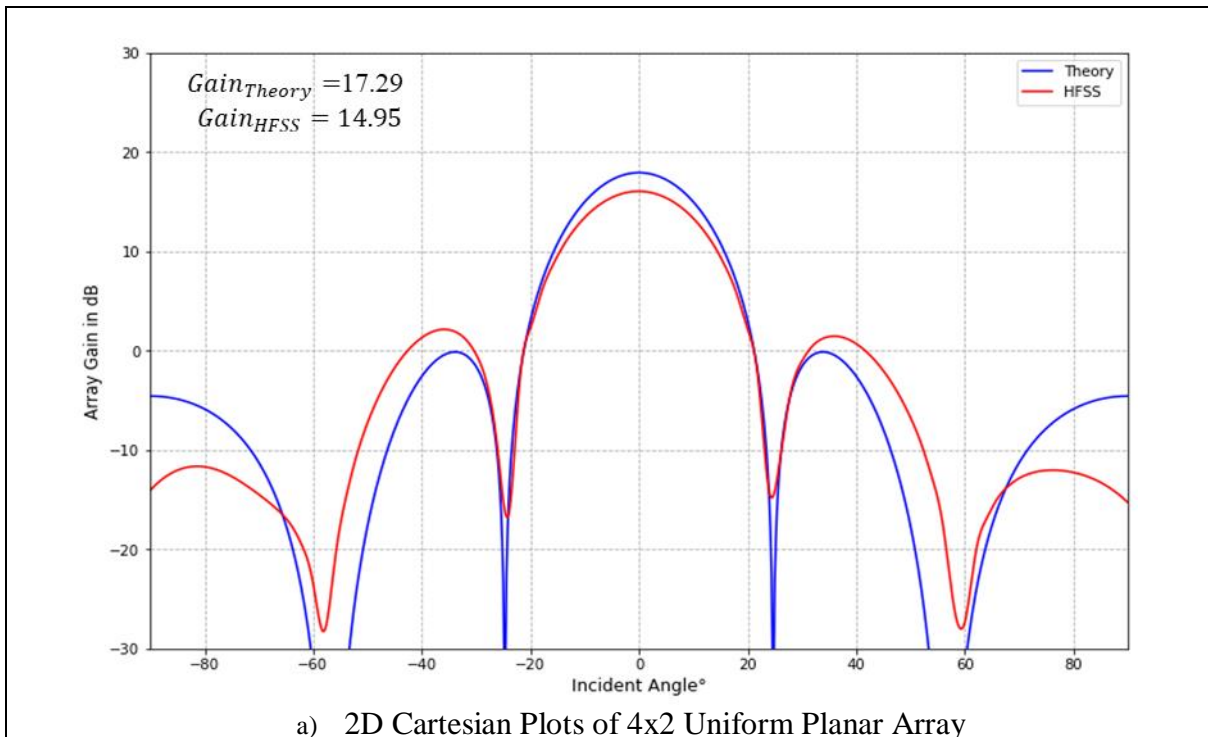
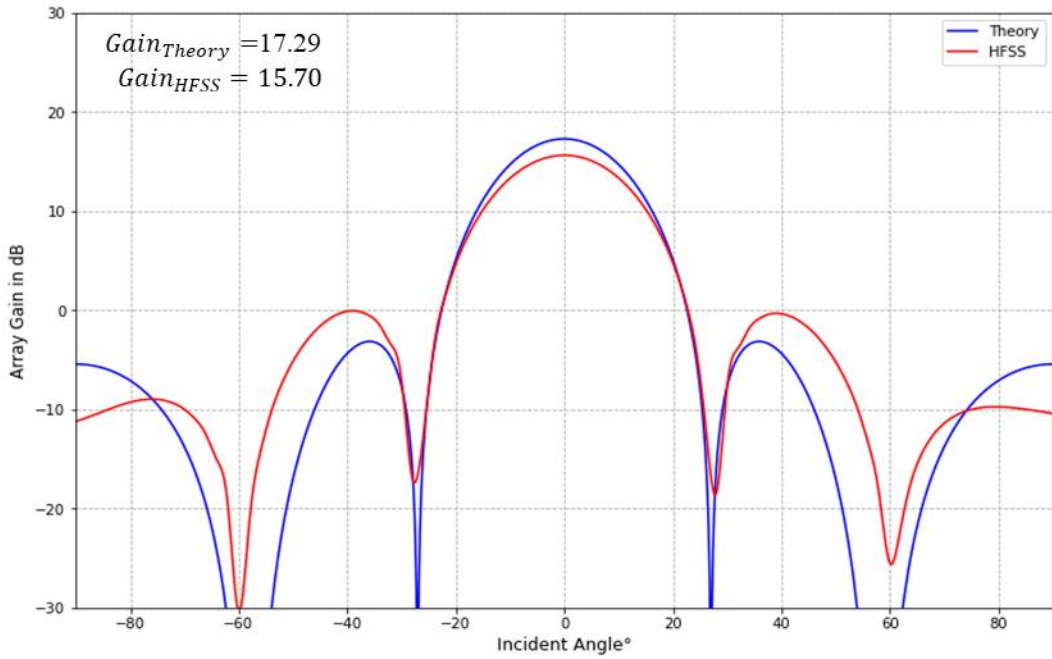
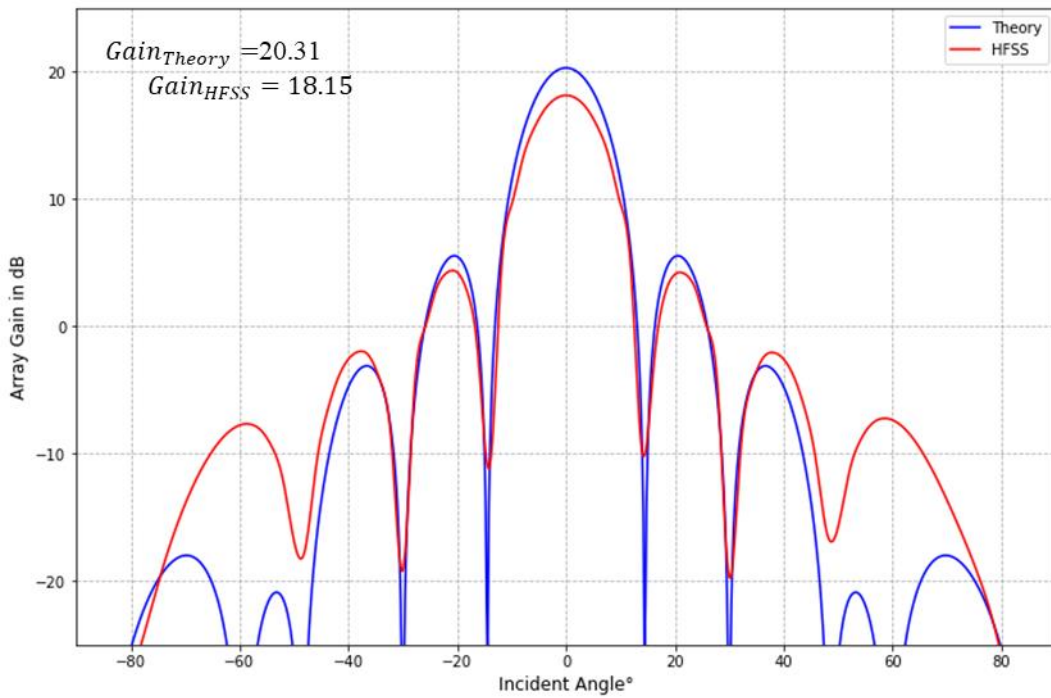


Figure 3.29 Comparison of Gain Patterns of Linear Arrays in HFSS and Theory





b) 2D Cartesian Plots of 4x2 Non-uniform Symmetric Linear Array



c) 2D Cartesian Plots of 8x2 Uniform Planar Array

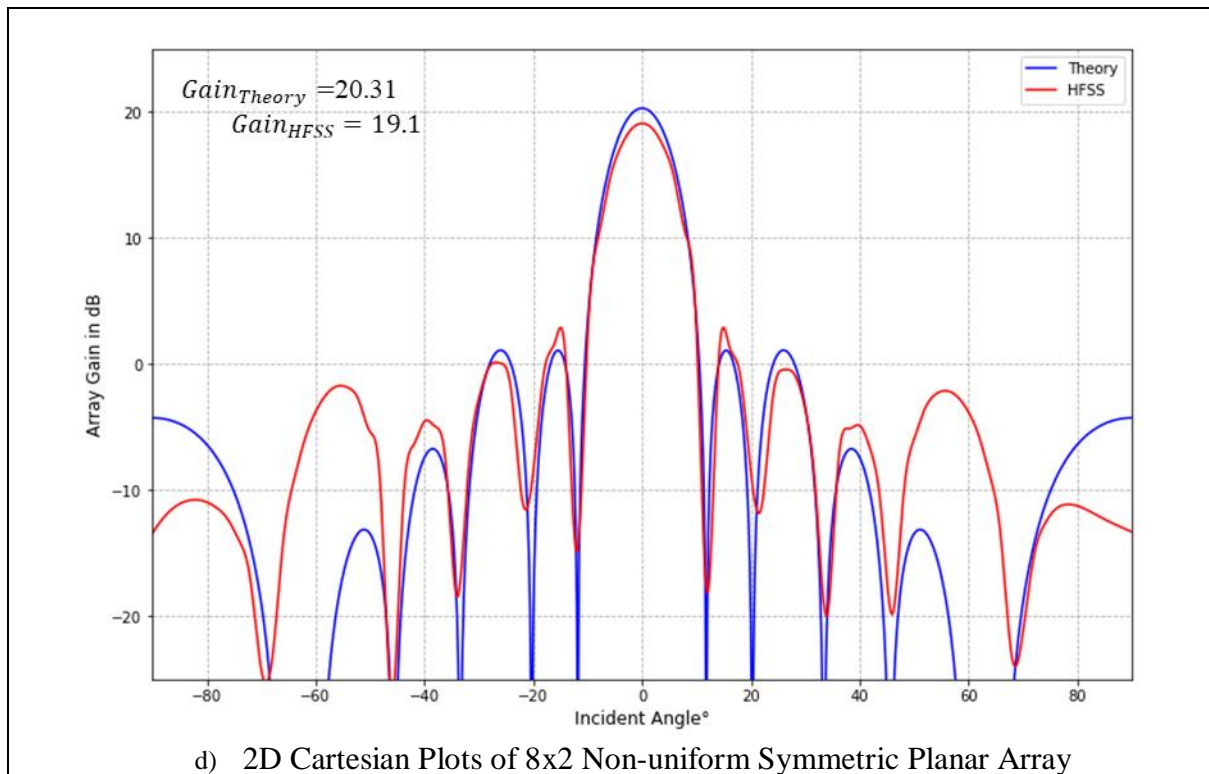


Figure 3.30 Comparison of Gain Patterns of Planar Arrays in HFSS and Theory

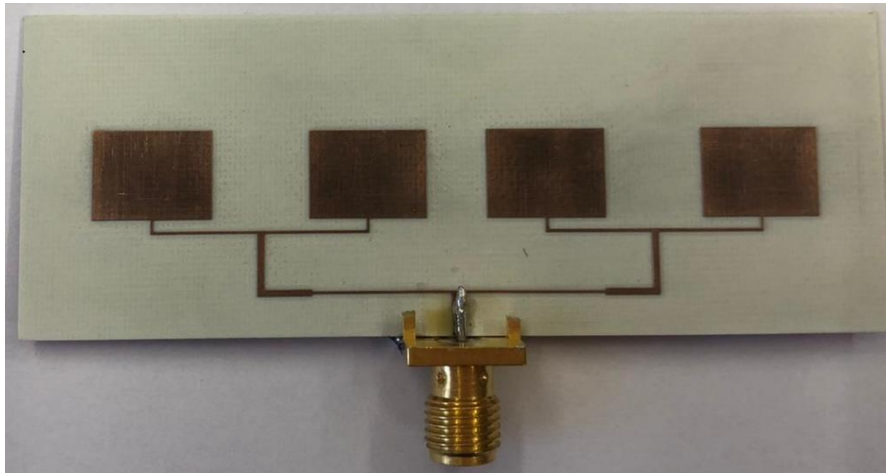
This comparison would be good for fundamental understanding of antenna array behaviour in both cases. As explicitly expressed in section 3.1, Python simulator is able to give the normalized array factor pattern which maximizes at 0 dB. According to equation 2.34, gain of antenna array can be calculated in dB by the summation of array factor and gain of the single array element. To be able to observe this comparison, gain of the designed single RMSA (7.6 dB) is added to the array factor pattern obtained in Python simulator. Accordingly, Figures 3.29 and 3.30 show this comparison for uniform as well as non-uniform symmetric linear and planar arrays with increase rate of 0.1λ , respectively. It can be deduced that Python simulator provides a useful outcome in terms of obtaining the expected behaviour of array pattern considering relevant factors which are array layout, geometrical configuration, beamforming techniques, steering angle and inter-element spacing. According to the comparison, HFSS simulation presents more realistic case since it contains all aforementioned losses such as the effects of materials and feed mechanism rather than the theoretical simulation in Python.

3.6 Fabrication and Measurement

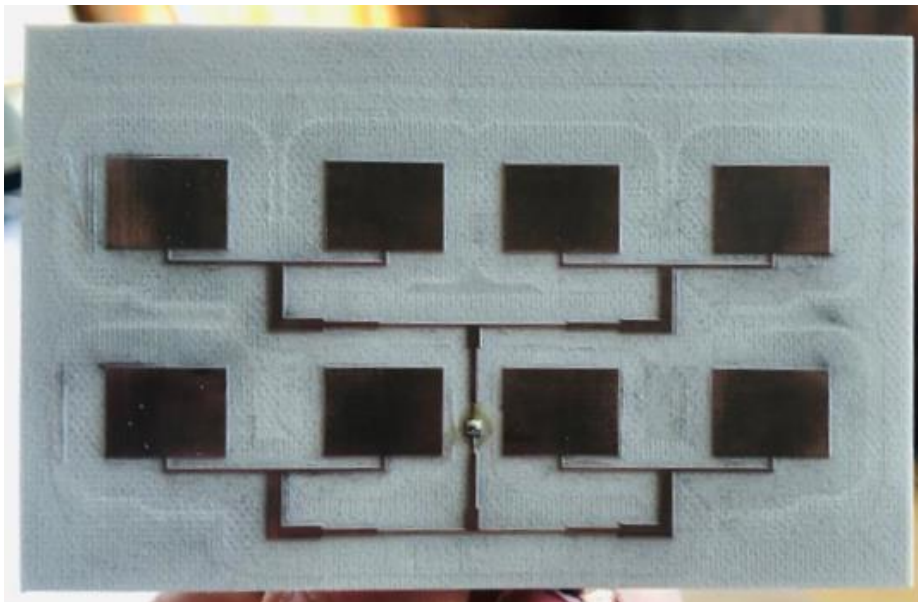
The symmetrical configurations of 4x1 linear and 4x2 planar antenna arrays are fabricated via 3D printing technology and standard PCB manufacturing process [54]. The equipment used for fabrication of arrays is LPKF ProtoMat as shown by Figure 3.31. The process of fabrication involves: Firstly, converting the HFSS design files into Gerber file via AWR software program. These files are required to work on the LPKF machine which allows to print designed antennas on the substrate. The machine makes the contour lines on the substrate for the areas from where the copper is to be removed and draws the shape of the antennas. After all, it hatches out the copper from unwanted areas and at the end, all the copper is removed from the contour lines with the help of suction machines. Hence, designed arrays printed on the substrate, Rogers 4003, whose dielectric constant is 3.55 and has 0.508 mm thickness which is useful for high frequency applications. The top view of the printed arrays is illustrated in Figure 3.32.



Figure 3.31 LPKF ProtoMat Machine [55]



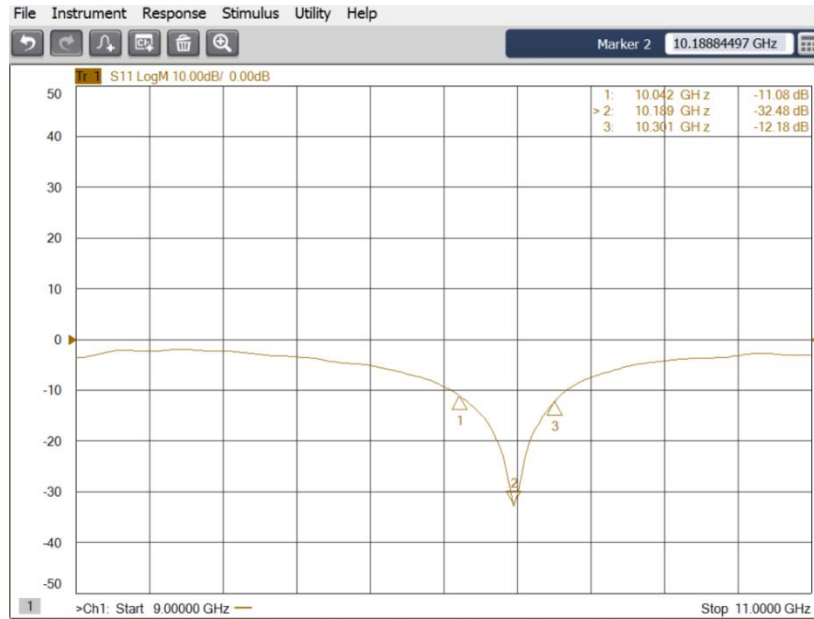
a) 4x1 Linear Symmetric



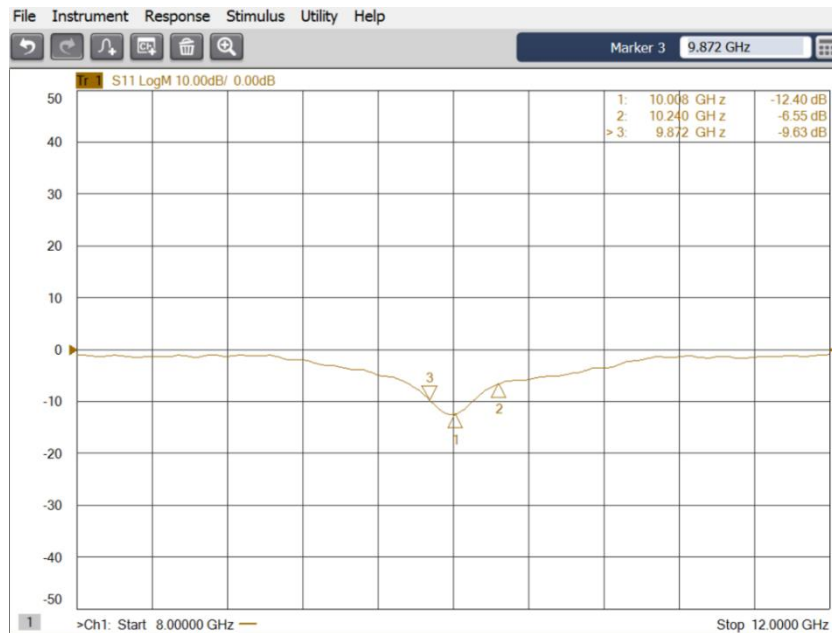
b) 4x2 Planar Symmetric

Figure 3.32 Top view of printed antenna arrays

The measurements were carried out at the normal laboratory environment rather than anechoic chamber. To verify the performance of proposed arrays, KEYSIGHT PNA Network Analyzer model N5224B, which has frequency range from 10MHz to 43.5 GHz, is utilized. The measurement results in terms of input return loss are shown in Figure 3.33.



a) 4x1 Linear Array



b) 4x2 Planar Array

Figure 3.33 Measured input Return Loss of 4x1 and 4x2 patch antenna arrays

According to the measurement results, it can be concluded that proposed linear and planar array work at 10.19 GHz and 10.08 GHz, respectively which are consistent with the purpose of this thesis project. Moreover, s_{11} parameter of both arrays are below -10 dB at the operating frequency which is the case for antennas working principle.

Furthermore, a pyramid horn antenna is used for the gain measurement as a transmitter source antenna where its gain and transmitter power are already known from its datasheet. Then, the received power of the arrays is measured via ROHDE&SCHWARZ SMB 100A Signal Generator and FSW Spectrum Analyser as the results are illustrated in Figure 3.34. Afterward, the gain calculation is made by Friis transmission equation since it defines the path loss which represents the signal attenuation. In fact, it directly provides the relation between received and transmitted power as mathematically given as follow [1]:

$$P_{rx} = P_{tx} G_{tx} G_{rx} \left(\frac{\lambda}{4\pi R}\right)^2 \quad (3.1)$$

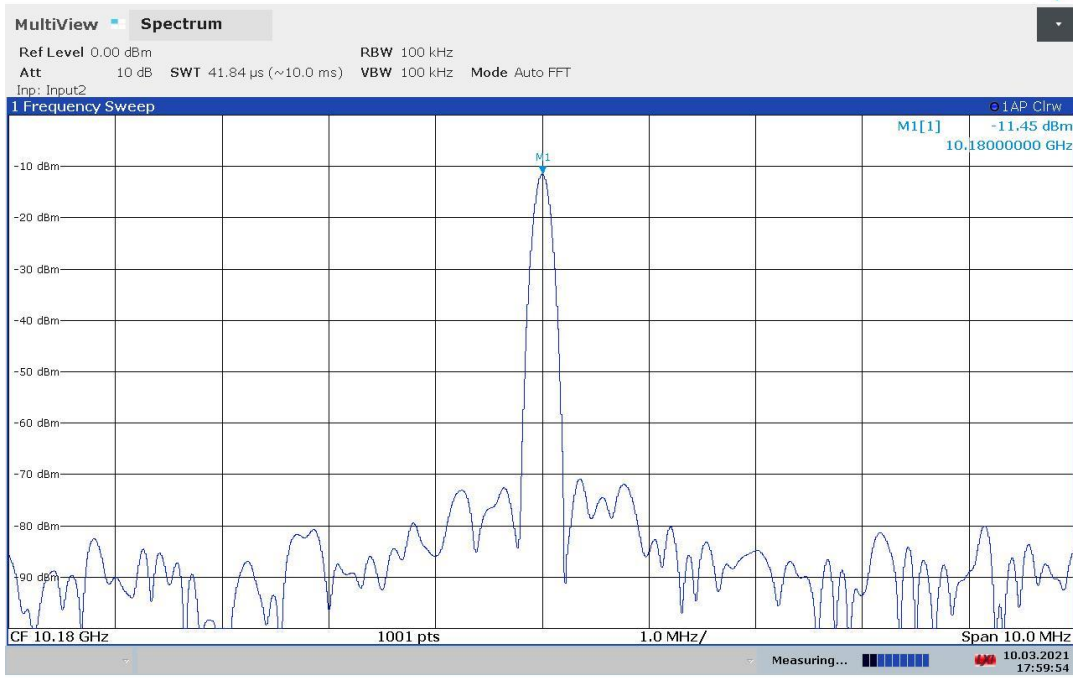
where P_{tx} : Input power in transmitter antenna, P_{rx} : Transmitted power in receiver antenna, G_{tx} , G_{rx} : Antenna's gains for transmitter and receiver antennas, respectively. R : The distance between receiver and transmitter antenna

In our case, the gain of the pyramid horn antenna is 12 dBi and the transmitter power is 13 dBm. The distance between the transmitter and receiver is considered with respect to the far-field condition. The measured cable loss is -4.6 dBm. Friis equation in dB should be considered as follows:

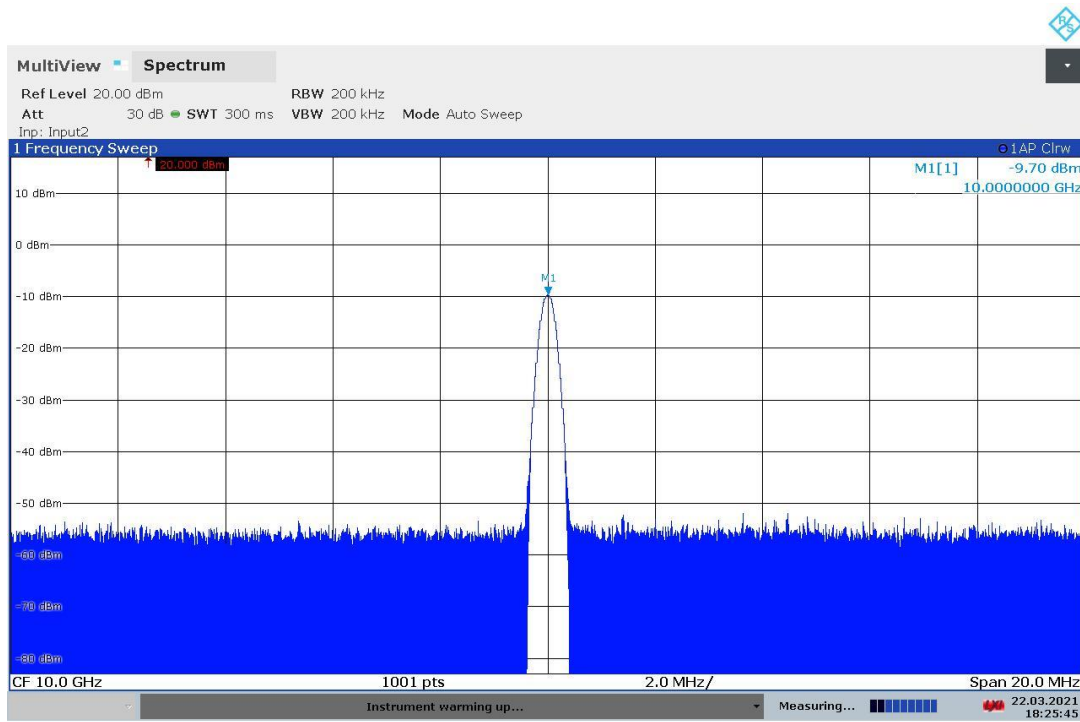
$$P_r = P_t + G_{tx} + 10\log\left(\frac{\lambda^2}{(4\pi d)^2}\right) + C_b + G_{rx} \quad (3.2)$$

where d : Distance between source and test antenna, C_b : Cable loss in dBm, P_r : Received Power in dBm P_t : Transmitted Power in dBm, G_{tx} : Gain of the transmitting antenna, G_{rx} : Gain of receiving antenna, λ : wavelength.

According to this calculation, the gains of proposed arrays are equal to 10.15 dB for 4x1 linear array and 12.3 dB for 4x2 planar array.



a) 4x1 Linear Array



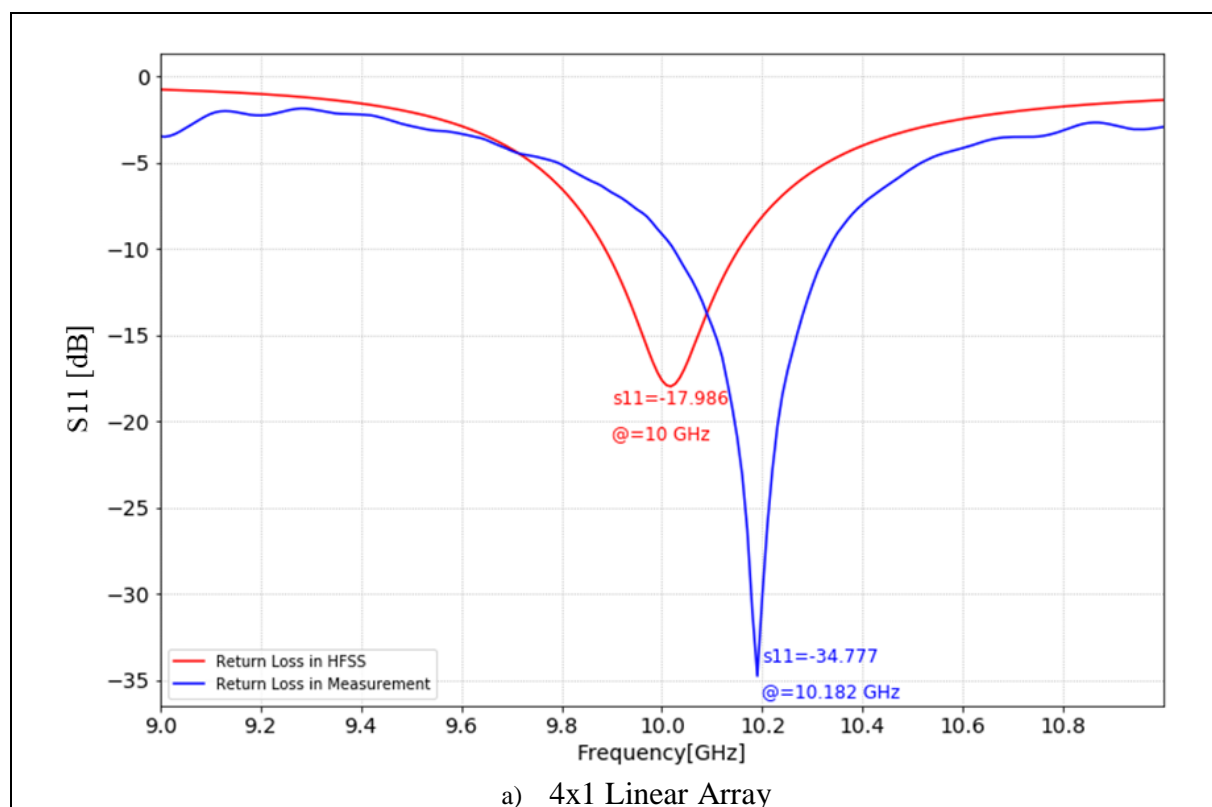
b) 4x2 Planar Array

Figure 3.34 Received power results of Spectrum Analyzer

Furthermore, the results obtained in HFSS and in the measurement are compared since the differences between them is significant to realize the antenna verification. The comparison is indicated in Table 3.9 and Figure 3.35 shows the comparison of input return loss parameters. As it is seen from the comparison, there is are different frequency shifts between S11 parameters for 4x1 (measurement result is upward) and 4x2 (measurement is downward). That could occur because of the calibration of equipment, soldering of feed mechanism (which directly affects impedance matching) as well as different surface roughness of the arrays.

Table 3.9 Comparison Between Simulation and Measurement Results

Parameters	Simulation(4x1)	Measurement(4x1)	Simulation(4x2)	Measurement(4x2)
f_r [GHz]	10	10.182	10.3	10
S_{11} [dB]	-17.986	-34.777	-21.1416	-12.086
Gain[dB]	11.94	10.15	15.7	12.3
BW $S_{11} < -10$ dB [MHz]	248.9	259	151.1	220



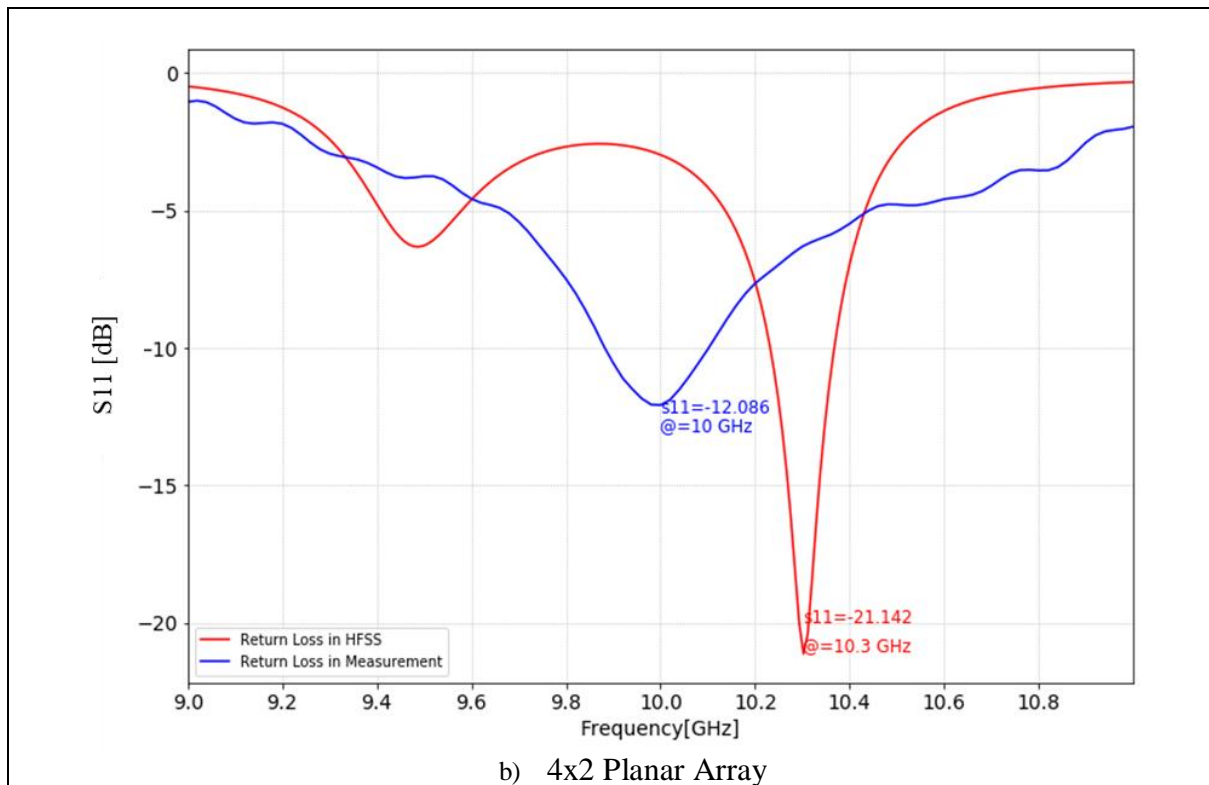


Figure 3.35 Comparison between the measured and simulated input return loss of proposed antenna arrays

The gap between the measurement and simulation can be explained by the following reason:

- Laboratory environment effect
- Insertion loss of connectors
- Fabrication tolerance
- Human error

Environment effect is the most significant reason which is absolutely relating to the near-field scattering objects such as metallic objects around the test environment in the laboratory. This would be relatively better and ideal to conduct test in anechoic chamber which eliminates reflection and external noise of electromagnetic waves. Secondly, the losses due to the feed connector and the coaxial cable also affect the array performance. In addition to them, fabrication tolerance of the machine (0.1 mm) as well as human error would cause some slight differences as well. Human error could be caused by soldering which is required for feed mechanism. Besides, due to the lack of the equipment in the laboratory, radiation patterns of arrays could not be compared which would be better for further verification.

4.

APPLICATION USE CASES AND RELEVANT ALGORITHM

The propagation characteristics of the Radio Frequency (RF) signals in mm frequency bands complicate the design of reliable communication systems since they can be easily blocked by obstacles preventing Line-of-Sight (LoS) communications. The high propagation loss limits the coverage region and thereby beamforming with large antenna array is necessary to concentrate the power in narrow, directional beams and increase the link budget [56]. The outstanding technologies like massive Multiple-Input Multiple-Output (MIMO) benefits from beamforming techniques to be able to serve users in the same time-frequency slot where the idea is to steer the beams towards the most powerful paths reaching the user [61]. As it is well known, the transmitted signal often reaches the receiver by more than one path, causing the multipath propagation or it is also called multipath fading [57]. The received signal is consisting of distorted version of transmitted signal. Multipath fading seriously degrades performance of communication system which totally depends on materials of the door and position of the furniture, influences on the signal power distribution within the building. Hence, few questions arise as how to identify these paths? and how to evaluate angle of arrival (AoA) at the receiver side? To clarify these queries, there are few well-known algorithms such as MVDR (Minimum Variance Distortionless Response), MUSIC (Multiple Signal Classification), ESPRIT (Estimation of Signal Parameters via Rotational Invariant Techniques) which require high level of complexity in terms of estimation and elaboration [60]. Besides them, Ray Tracing (RT) is a good candidate for BF and MIMO technology [63]. Accordingly, RT simulation tool, which was developed at the University of Bologna by the group of Research in Electromagnetic Propagation and Wireless Channel Modeling [61], is utilized in this thesis. RT is a strong deterministic numerical method used to examine and forecast the radio channel in the given propagation scenario. It is based on classical Geometrical Theory of Propagation (GTP) in Geometrical Optics (GO) and in Uniform Theory of Diffraction (UTD) [61] to simulate radio propagation paths between the transmitter and the receiver.

Within the scope of this thesis, indoor environment is considered which have reflection, refraction and diffraction of radio waves due to objects such as walls and doors inside a building. Accordingly, the aforementioned RT tool is used in order to predict radio propagation in created indoor environment where multipath disturbances appear. Figure 4.1 illustrates two different indoor environments which include one transmitter (Tx) which is isotopic antenna since it is common in most of the communication applications due to wide bandwidth as well as one communication receiver (Rx) in which the radiation characteristic of proposed antenna arrays is used. Beside them, there is an obstacle in between Tx and Rx as well as walls (in Scenario II) whose properties such as thickness, material type, location, height are decisive parameters for the analysis.

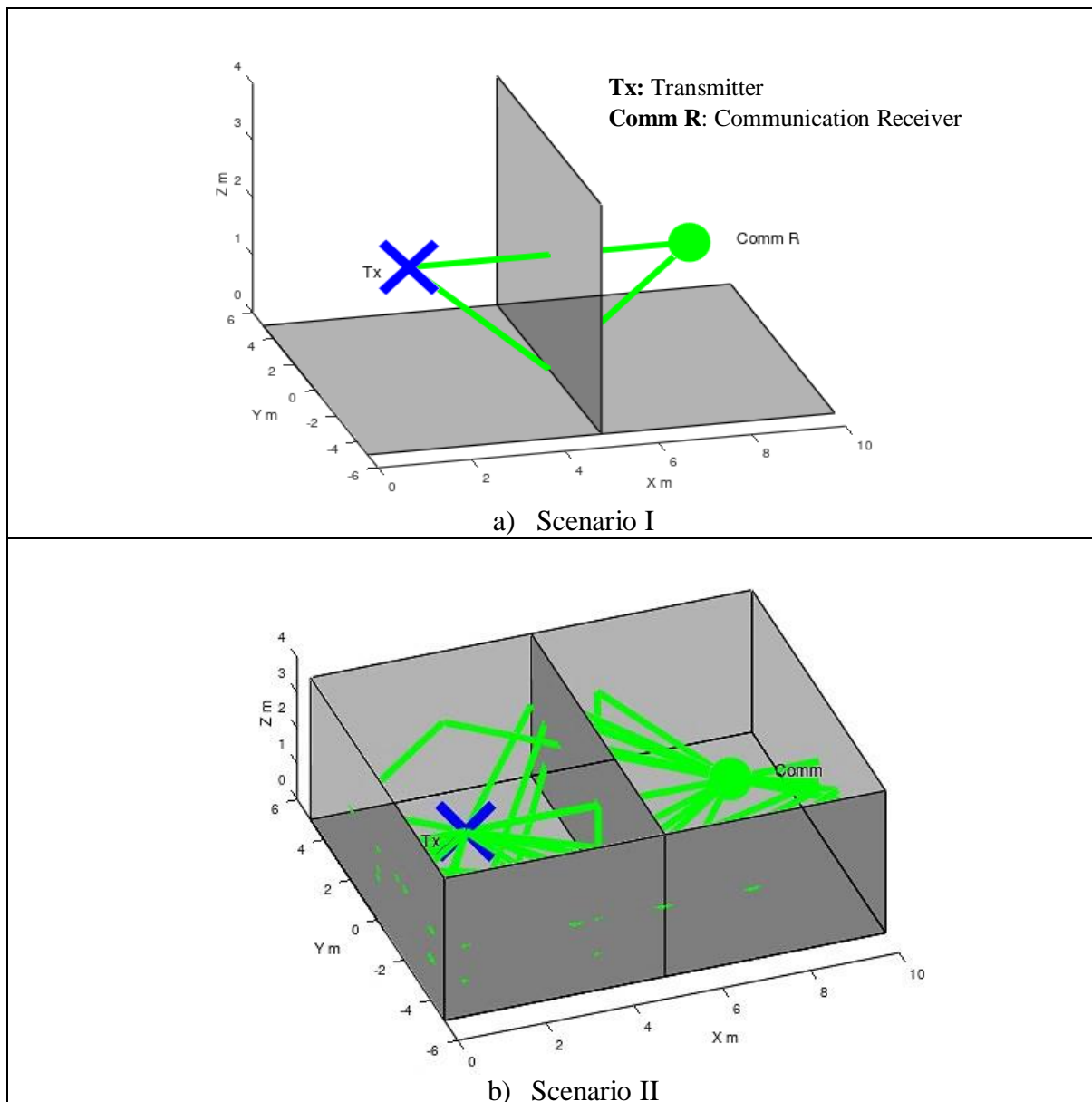


Figure 4.1 Scenario for Ray Tracing

In the RT simulator, designed antenna arrays of 4x2 and 8x1 were utilized for evaluating and analysing the different path-rays of their received power in dBm with delay spread profile. The delay profile is one of the significant parameters in the wireless communication system since it measures the effect of time (pulse) dispersion in multipath channel. This time (pulse) dispersion arises as a result of the different signal taking times to cross the channel through different propagation. In other words, the power delay profile gives the signal power received through a multipath channel as function of the time delay [65]. RT tool describes each multipath by rays as seen by green lines in Figure 4.1. A detailed description of propagation environments which is essential for accurate channel prediction is given by Table 4.1.

Table 4.1 Features of Indoor Environments

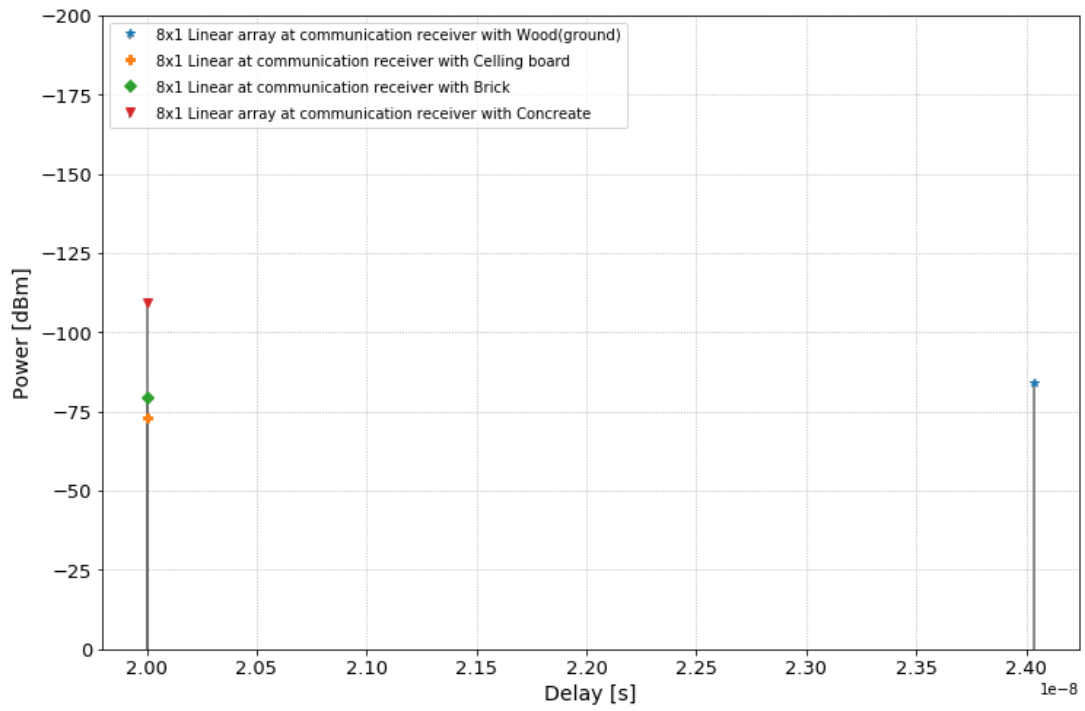
Type of Tx	Isotropic Antenna
Gain of Tx	0 dBi
Type of Rx	4x2 planar array & 8x1 linear array
Height of the Tx and Rx [m]	2
Frequency [GHz]	10
Distance between the Tx and Rx [m]	6
Obstacles' Thickness [m]	0.25
Obstacles' Height [m]	4

The reflection and transmission characteristics of the electromagnetic waves through and from the indoor obstacles is the key in designing a radio propagation model. The materials' electric and magnetic properties, which is thoroughly explained in [8], determine the behaviour of reflection and transmission of the electromagnetic waves [64]. Accordingly, three different materials as ceiling board, brick, concrete are investigated due to their low, middle and high relative permittivity, respectively. Ground plane is chosen as wood for each case. Table 4.2 gives all necessary material properties.

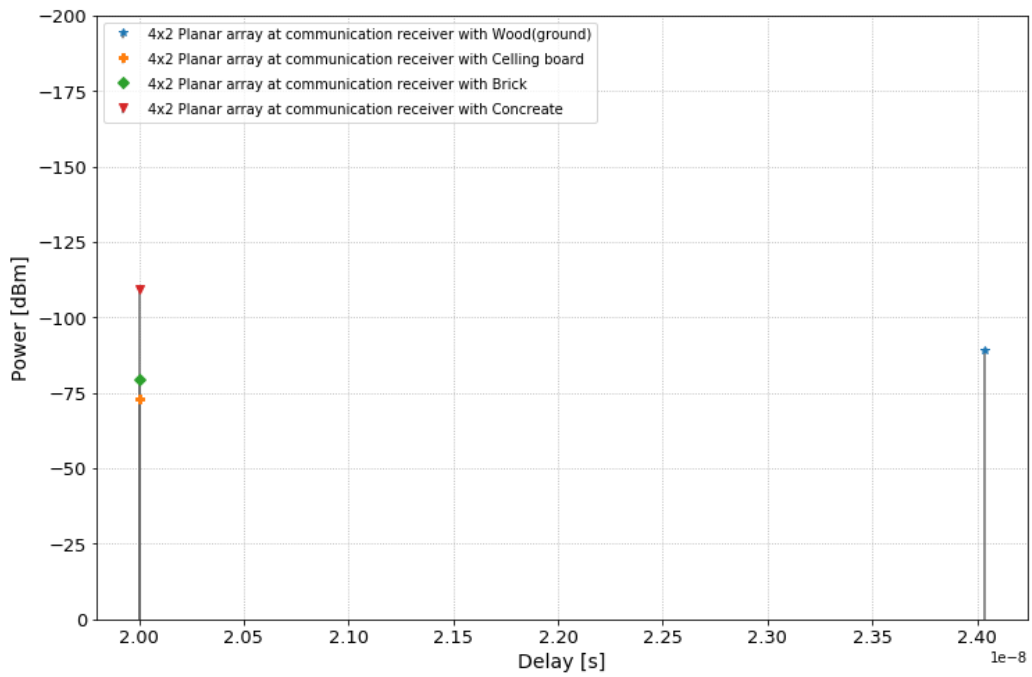
Table 4.2 Material Properties

	Celling board	Brick	Concrete	Wood
Frequency, f_r [GHz]	10	10	10	10
Relative Permittivity of real part , ϵ'_r	1.500	3.750	5.310	1.990
Conductivity, σ [S/m]	0.007	0.038	0.212	0.056
Relative Permittivity of imaginary part, ϵ''_r	0.013	0.068	0.378	0.100
Loss tangent, $\tan\delta$	0.009	0.018	0.071	0.050
Attenuation rate [dB/m]	9.66	10	149.13	64.27

By ray-tracing technique, it is supposed that all obstacles' dimensions in scenarios I-II are larger than the wavelength. The relevant propagation in the channel are combinations of multiple reflections which depend on the incident angle, material properties and polarization are calculated with respect to Fresnel reflection and transmission coefficients [67]. Besides, using Snell's law, the refraction angle is substituted with the equation of the incident angle and refractive indexes of the medium [63]. Accordingly, this RT tool has ability to obtain rays with multiple reflection, multiple diffractions and combinations of both. However, in this thesis, the scattering and the diffraction were not taken into account. The formulation of reflected is carried out based on geometrical optics (GO) for the calculation of electromagnetic wave theory [61]. Figure 4.2 and Figure 4.3 shows the response of arrays with the comparison of aforementioned materials in Scenario I and Scenario II, respectively. Each bar on the plot represents a single reflected ray. According to results, it is obtained that the higher the permittivity, the lower the received power due to the wave impedance depending upon the relative permittivity of the walls used for building materials [61].



a) 8x1 Linear Array



a) 4x2 Planar Array

Figure 4.2 Arrays with the Comparison of Different Materials in Scenario-1

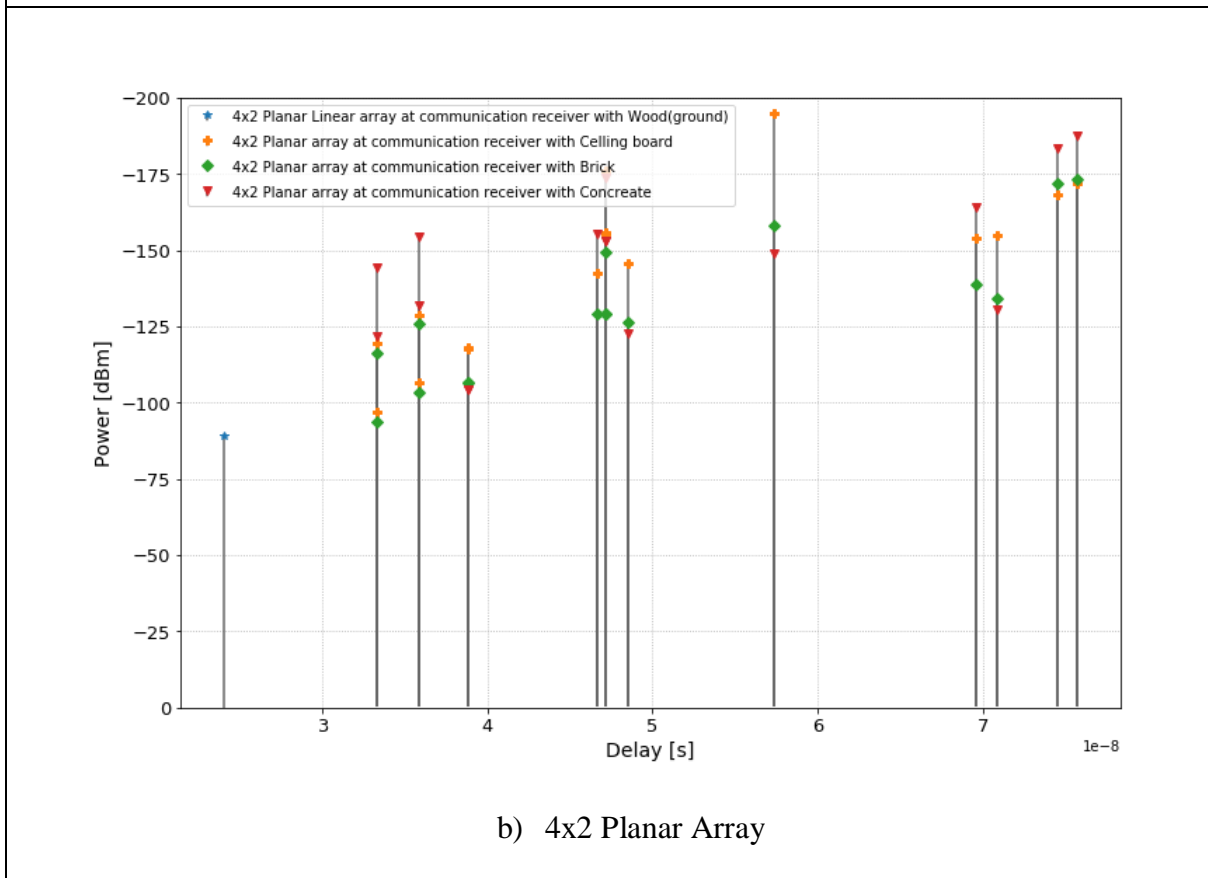
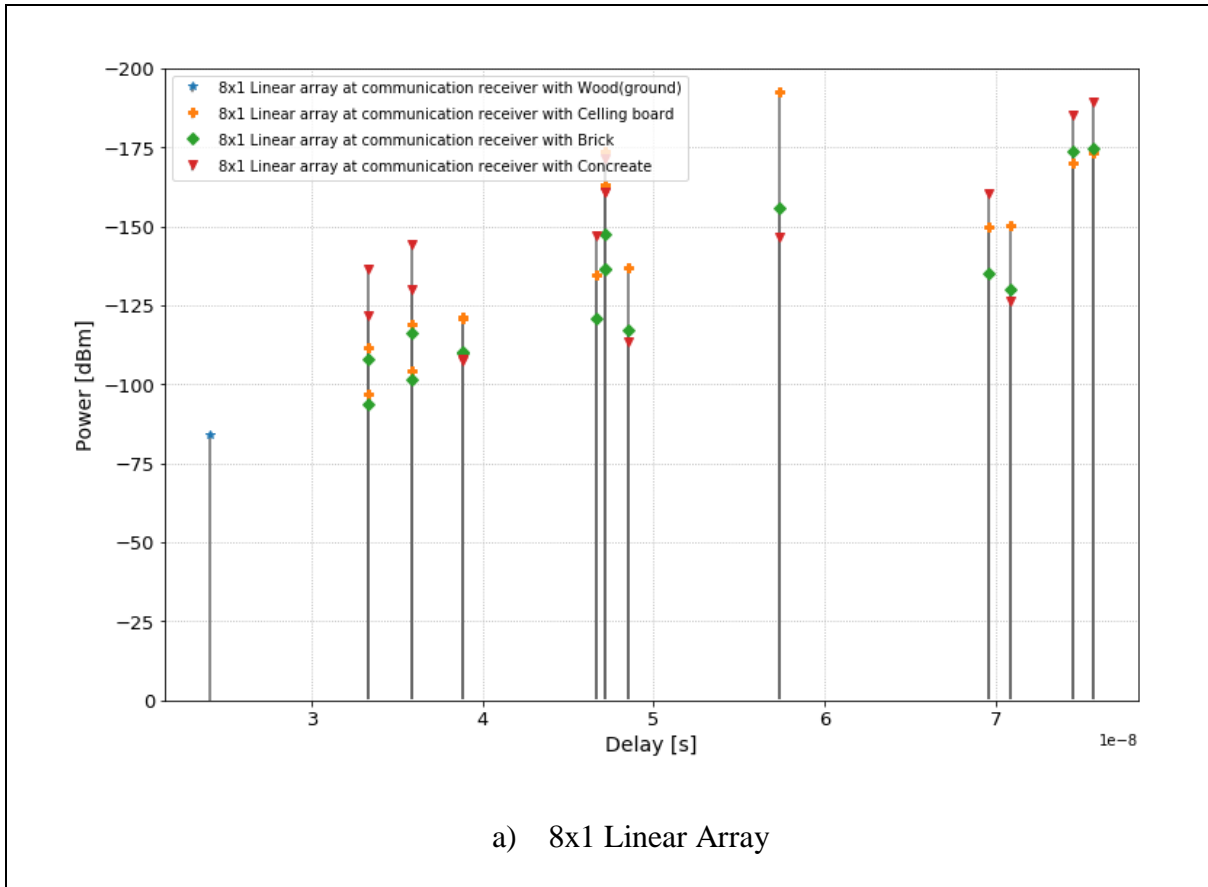


Figure 4.3 Arrays with the Comparison of Different Materials in Scenario-2

Furthermore, the performance of 4x2 and 8x1 arrays in terms of received power are also compared in Scenario-II by concrete as illustrated in Figure 4.4.

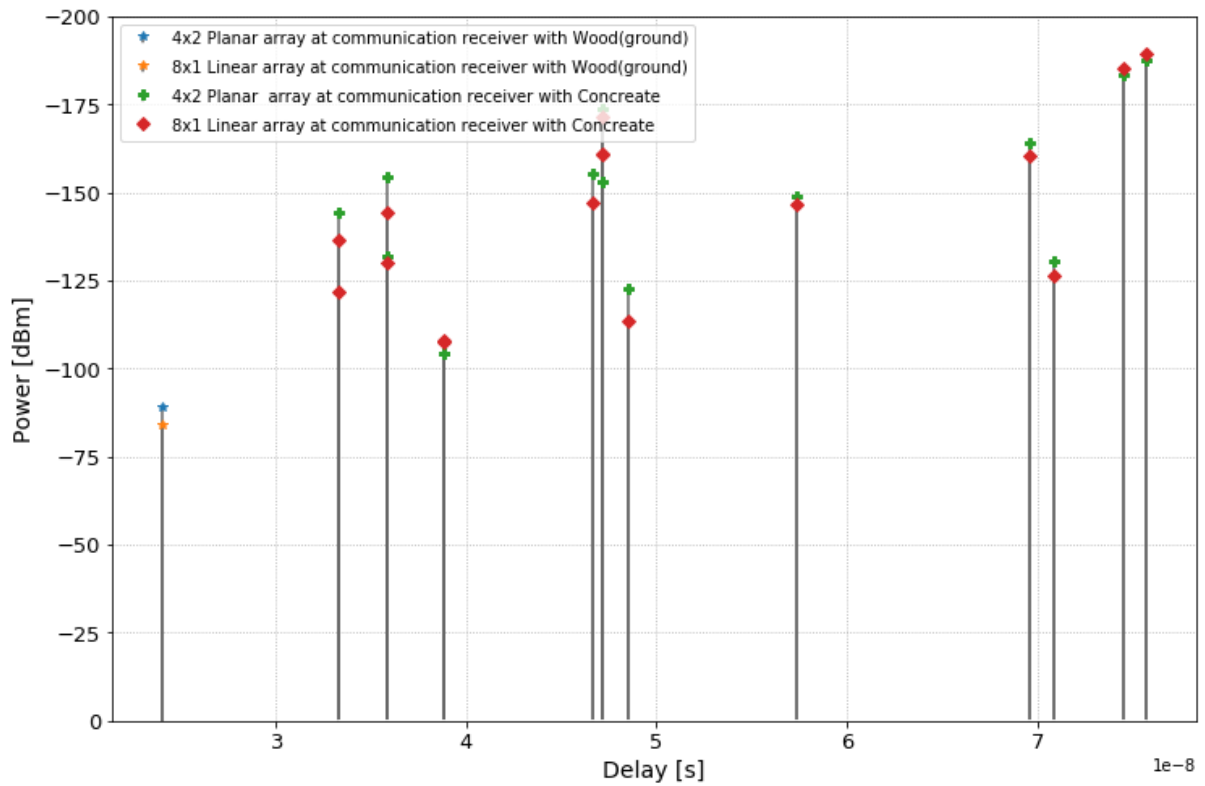


Figure 4.4 Performance Comparison of 4x2 and 8x1 Arrays with Concrete

According to the plot, the reflected rays, which are bouncing on the walls, carry less power with 4x2 planar antenna: the green dots are higher than the red dots since 4x2 planar array is more directive and radiating more power on a concentrate beam along the radial direct path between Tx and Rx. This means that less power is spread all over the environment.

5.

CONCLUSION

This master thesis study presents an exhaustive survey on the design of antenna array for mm-wave & sub mm-wave communications. Accordingly, the investigation of array antennas for mm-wave communication with their fundamental characteristics, benefits, drawbacks as well as design and fabrication process are described. The design of mm-wave arrays has become attractive among the researchers since phased array antenna technology has ability to produce high gain with high directive beam in desired direction. However, there are various challenges such as choice of antenna array structure, method of beamforming, mutual coupling between array elements, etc. Therefore, for mm-wave applications, careful consideration should be given on the selection of antenna element, material properties, mutual coupling, feed radiation loss in order to evaluate the performance of arrays with respect to the gain, radiation pattern, bandwidth and directivity. The objective of this thesis was to investigate, analyse, design and fabricate various antenna arrays which can be utilized in (but not limited to) phased array antenna systems with different geometrical arrangements and element layouts. First of all, an open-source Python simulator has been developed to evaluate the behaviour of the desired array characteristic in terms of how the array antenna is affected by changing crucial parameters such as the inter-element spacing, number of elements, array geometry, layout, beamforming techniques and beam steering angle. Accordingly, the performance of phased array antennas, which provides flexibility to electronically steer transmitted signal into the desired angle, can be examined by this simulator since it is capable of presenting how the array factor pattern changes when using common beamsteering techniques which are phase shifting or true time-delay technique in this study. Hence, the simulator provides easy and beneficial way to design array antenna since it gives behaviour of array pattern rapidly as an initial impression without needing long simulations. Moreover, 3D EM simulator, HFSS, was also used to design and simulate the proposed arrays in more realistic environment. Afterward, a linear and a planar array were fabricated and measured in the laboratory to verify the results obtained via prior computational simulations. In addition, the side lobe level reduction, and thereby higher gain, are also considered with unequal spacing which gives the response of array with enhanced performance.

In particular, a considerable improvement of side-lobe level can be obtained by using non-uniform symmetrical array arrangement in comparison to uniform and non-uniform asymmetrical arrays. The second advantage of symmetrical arrangement is to achieve the same beamwidth with a smaller number of elements in comparison to uniform arrays. Furthermore, the proposed arrays were integrated in RT tool that utilises numerical deterministic method to predict radio propagation between the Transmitter and the Receiver. Thus, the angle of arrival of each ray as well as received power with delay profile can be analysed. In addition, RT tool was used to observe the effects of different materials on the performance of proposed Linear and Planar arrays at receiver side. In addition to the conclusions, a further research corresponding to this study can be continued with optimization of random unequal spacing between the array elements. This would be the best approach to suppress SLLs as much as possible to get enhanced performance. Besides this, to degrade the effect of mutual coupling, the methods mentioned in the section 2.5.5 would be implemented in the design phase of the arrays.

BIBLIOGRAPHY

- [1] Balanis C. A. Antenna Theory: Analysis and Design (3rd edition), 2005.
- [2] Thrimurthulu V. Lecture Notes on Antenna & Wave Propagation, 2013.
- [3] Reckeweg M. and Rohner C. Antenna Basics, 2015
- [4] Kraus J. D. and Marhefka R. J. Antennas for All Applications, 2002.
- [5] Jensen S. Microstrip Patch Antenna, 2010.
- [6] Garg R. Microstrip Antenna Design Handbook, 2000.
- [7] Pozar D. M. Microwave Engineering (4th edition), 2011.
- [8] Skolnik M. I. Introduction to Radar Systems (2nd edition), 1980.
- [9] Subrahmanya V. L. Pattern analysis of ‘The Rectangular Microstrip Patch Antenna’, 2009.
- [10] Ghosh S, Debarati S. An Inclusive Survey on Array Antenna Design for Millimeter-Wave Communications, 2019.
- [11] Connor J.D. Antenna Array Synthesis Using the Cross Entropy Method, 2008.
- [12] Zooghyby A. E. Smart Antenna Engineering, 2005.
- [13] Delos P., Broughton B., Kraft J. Phased Array Antenna Patterns—Part 1: Linear Array Beam Characteristics and Array Factor, 2020.
- [14] Huang Y., Boyle K. Antennas from Theory to Practice, 2008.
- [15] Rocca P., Oliveri G., Mailloux R.J., Massa A. Unconventional Phased Array Architectures and Design Methodologies –A Review, 2016.
- [16] Orfanidis J. Electromagnetic Waves and Antennas Sophocles, 2016.
- [17] Gross F.B. Smart Antennas with MATLAB (2rd edition), 2011.
- [18] Safaai-Jazi A. and Stutzman L., Side Lobe Reduction in Uniformly Excited Linear Arrays, 2015.
- [19] Gutton H. and Baissinot G., Flat Aerial for Ultra High Frequencies, French Patent No. 703 113, 1955.
- [20] Jasim S.E, Jusoh M.A, Mazwir M.H, Mahmud N.S. Finding The Best Feeding Point Location of Patch Antenna Using HFSS, 2015.
- [21] Abimbola R. A, Akinwale A. K. Design and Analysis of Broadside Arrays of Uniformly Spaced Linear Elements, 2016.
- [22] Dutta K.P. Study of Broadside Linear Array Antenna with Different Spacing and Number of Elements, 2017.

- [23] Abimbola R. A. Effects of Spacing and Number of Elements on the Fields Radiated by Linear Arrays of Equally Spaced Elements, 2017.
- [24] Adnan N. H. M, Rafiqul I. M, Alam A Z. Effects of Inter Element Spacing on Large Antenna Array Characteristics, 2017.
- [25] Siakavara K. Methods to Design Microstrip Antennas for Modern Applications, 2010.
- [26] Mailloux R. J. Phased Array Antenna Handbook (2nd edition), 2005.
- [27] Alami A. E., Bennani S. D., Bekkali M. E. and Benbassou A. Optimization and High Gain of a Microstrip Patch Antenna Excited by Coaxial Probe for RFID Reader Applications at 2.4 GHz, 2013.
- [28] Garg R., Bhartia P., Bahl I., Ittipiboon A., Microstrip Antenna Design Handbook, 2001.
- [29] Hu et al. Characterization of the Input Impedance of the Inset-Fed Rectangular Microstrip Antenna, 2008.
- [30] Alhaji I. A., Ishaq F. S., Aminu A. S. Effect of Feed Techniques and Substrate Material on Rectangular Patch Antenna, 2017.
- [31] Roy, A. A., Mom, J. M., Kureve, D. T. Effect of Dielectric Constant on the Design of Rectangular Microstrip Antenna, 2013.
- [32] Md Tan M. N., Rahim S. K. A., Ali M. T. and Rahman T.A. Smart Antenna: Weight Calculation and Side-lobe Reduction by Unequal Spacing Technique, 2008.
- [33] Ashton B. T., Jovanovic B., Rzayev T. An 8x1 Wideband Antenna Phased Array, 2011.
- [34] Haupt R.L, Rahmat-Samii Y. Antenna Array Developments: A Perspective on the Past, Present and Future, 2015.
- [35] Herd J. S., Conway M.D. The Evolution to Modern Phased Array Architectures, 2015.
- [36] Uchendu I., Kelly J. Survey of Beam Steering Techniques Available for Millimeter Wave Applications, 2016.
- [37] Adami et al., Beamforming Techniques for Large-N Aperture Arrays, 2010.
- [38] Hastürk A., Akçam N., Okan T. Design, fabrication and performance analysis of TTD structures for S-band active phased array RF beamforming networks, 2019.
- [39] Kumar A., Kaur J., Singh R. Performance Analysis of Different Feeding Techniques, 2013.
- [40] Available online: <https://vtechworks.lib.vt.edu/bitstream/handle/10919/27291/ch3.pdf>
- [41] Longbrake M. True Time-Delay Beamsteering for Radar, 2012.
- [42] Kiani et al. Wide scan phased array patch antenna with mutual coupling reduction, 2018.
- [43] Habashi A, Nourinia J, Ghobadi C. Mutual Coupling Reduction Between Very Closely Spaced Patch Antennas Using Low-Profile Folded Split-Ring Resonators (FSRRs), 2011.

- [44] Tang et al. Mutual Coupling Reduction Using Meta-Structures for Wideband, Dual-Polarized, and High-Density Patch Arrays, 2017.
- [45] Hajilou Y., Hassani H. R., Rahmati B. Mutual coupling reduction between microstrip patch antennas, 2012.
- [46] Wei et al. Mutual coupling reduction by novel fractal defected Ground Structure Bandgap Filter, 2016.
- [47] Yu A., Zhang X. A novel method to improve the performance of microstrip antenna arrays using a dumbbell EBG structure, 2003.
- [48] Puzella A. Theoretical and Experimental Development of an Array of Droopy Bowties with Integrated Baluns, 2014.
- [49] Gulbrandsen F. Design and Analysis of an X-band Phased Array Patch Antenna, 2013.
- [50] Rabinovich V., Alexandrov N. Antenna Arrays and Automation Applications, 2013.
- [51] Delos P., Broughton B., Kraft J. Phased Array Antenna Patterns—Part 2: Grating Lobes and Beam Squint, 2020.
- [52] Granados S., Karine L. Antenna for Milimeter-Wave Applications, 2016.
- [53] Kuhn W. B. and Nouredin I. M., Analysis of Current Crowding Effects in Multiturn Spiral Inductors, 2001.
- [54] Coombs C. F., Printed Circuits Handbook. McGraw-Hill Companies, 2008.
- [55] Online available: <https://www.lpkfusa.com/pcb/>
- [56] Hansen, C.J., “WiGiG: Multi-gigabit wireless communications in the 60 GHz band”, IEEE Wireless Communications, 2011
- [57] Wi-Fi Alliance. WiGiG and the future of seamless connectivity, 2013.
- [58] Moiin H., Looking ahead to 5G, presentation hold at EuCNC, 2014.
- [59] Rohde & Schwarz. Millimeter-Wave Beamforming: Antenna Array Design Choices & Characterization, 2016.
- [60] Van Trees H. L., Optimum Array Processing, 2002.
- [61] Zoli M., Performance Analysis of Ray-Tracing Assisted Beamforming Techniques for Future mm-wave Wireless Systems, 2015.
- [63] Muñoz J. C. Characterization of radio propagation channel in industrial systems, 2014.
- [64] Regmi A., Reflection Measurement of Building Materials At Microwaves, 2016.
- [65] Maw M., Promwong S., Takada J.I. Indoor Propagation Channel Model with Ray Tracing for Wireless Communications, 2019.

- [66] Tascioglu M., Design, Investigation and Characterization of Bow-Tie Antenna for 24 GHz Radar Systems, 2020.
- [67] Rappaport T. S., Wireless Communications: Principle and Practice, 2002.
- [68] Prof. Dr.-Ing. Axel Bangert, Lecture notes of Microwaves and Millimeter waves II (Part I), 2017
- [69] Caspers F., RF Engineering Basic Concepts: the Smith chart, 2012
- [70] Obot A. B., Igwue G.A., Udofia K. M.. Design and Simulation of Rectangular Microstrip Antenna Arrays for Improved Gain Performance, 2019